UNIVERSIDADE FEDERAL DO CEARÁ

CENTRO DE TECNOLOGIA

DEPARTAMENTO DE ENGENHARIA METALÚRGICA E DE MATERIAIS

PROGRAMA DE PÓS-GRADUAÇÃO EM ENGENHARIA E CIÊNCIA DE MATERIAIS

PAULO VICENTE DE CASSIA LIMA PIMENTA

SIMULATION OF THE THERMAL-MECHANICAL CONTINUOUS CASTING PROCESS USING UNSTRUCTURED GRIDS

FORTALEZA

2019

PAULO VICENTE DE CASSIA LIMA PIMENTA

SIMULATION OF THE THERMAL-MECHANICAL CONTINUOUS CASTING PROCESS USING UNSTRUCTURED GRIDS

Tese apresentada ao Programa de Pós-Graduação em Engenharia e Ciência de Materiais do Departamento de Engenharia Metalúrgica e de Materiais da Universidade Federal do Ceará, como requisito parcial para obtenção do título de Doutor em Engenharia e Ciência de Materiais. Área de Concentração: Processos de Transformação e Degradação de Materiais.

Orientador: Prof. Dr. Francisco Marcondes.

FORTALEZA

2019

Dados Internacionais de Catalogação na Publicação
Universidade Federal do Ceará
Biblioteca Universitária
Gerada automaticamente pelo módulo Catalog, mediante os dados fornecidos pelo(a) autor(a)

P697 Pimenta, Paulo Vicente de Cassia Lima Pimenta.
Simulation of the thermal-mechanical continuous casting process using unstructured grids / Paulo Vicente de Cassia Lima Pimenta Pimenta. – 2019.
132 f. : il. color.

Tese (doutorado) – Universidade Federal do Ceará, Centro de Tecnologia, Programa de Pós-Graduação em Engenharia e Ciência de Materiais, Fortaleza, 2019.
Orientação: Prof. Dr. Francisco Marcondes.

1. Lingotamento continuo. 2. Plasticidade. 3. Visco-plasticidade. 4. Método de volumes finitos baseado em elementos. I. Título.

CDD 620.11

PAULO VICENTE DE CASSIA LIMA PIMENTA

SIMULATION OF THE THERMAL-MECHANICAL CONTINUOUS CASTING PROCESS USING UNSTRUCTURED GRIDS

Thesis submitted to the Graduate Program in Materials Science and Engineering of the Federal University of Ceará as a partial requirement for obtaining the degree of Doctor in Materials Science and Engineering. Concentration Area: Processes of Transformation and Degradation of Materials.

Approved in: August 23th, 2019.

COMITEE MEMBERS

Prof. Dr. Francisco Marcondes (Orientador)
Federal University of Ceará (UFC)

Prof. Dr. Clovis Raimundo Maliska
Federal University of Santa Catarina (UFSC)

Prof. Dr. Lindberg Lima Gonçalves
Federal University of Ceará (UFC)

Prof. Dr. Cleiton Carvalho Silva
Federal University of Ceará (UFC)

Dr. Eng. Alex Maia do Nascimento
Companhia Siderúrgica do Pecém (CSP)

To my mother and in memory of my grandfather.

ACKNOWLEDGEMENTS

Firstly, I would like to express my sincere gratitude to my family for their never ending support over my life choices. In special, I would like to thanks my mother, Claudinete Lima Pimenta, for the constant support and confidence in my competence. In addition, I have a lot of gratitude to my fiancée, Ingred Souza Silva. I am extremely thankful for the affection and patience I demanded from her. And I also have to recognize and thank Justina Ferreira Lima, my great aunt, for her countless advises and financial support she gave me during the years.

I thank my supervisor, Prof. Francisco Marcondes, for the continuous support of my Ph.D study and related research, for his patience, motivation, and immense knowledge. His guidance helped me in all the time of research and writing of this thesis. Besides my advisor, I would like to thanks Prof. Evandro Parente Junior, for all the help in ideas and comments. I also would to express my sincere gratitude to the rest of my thesis committee: Prof. Clovis R. Maliska, Prof. Cleiton Carvalho Silva, Dr. Alex Maia do Nascimento, and Prof. Lindberg Lima Gonçalves.

My sincere thanks also goes to Prof. Gregory J. Rodin, who provided me an opportunity to join their team as a visitor student at The University of Texas at Austin, and who gave me valuable advice and insightful comments during the brief time I spent under his supervision.

I thank my fellow labmates for the stimulating discussions, for the sleepless nights we were working together before deadlines, and for all the fun we have had in the last six years. They are: Ivens Costa, Dimitry Pessoa, José Renê de Sousa Rocha, João Henrique Gomes, Yuri Cruz, Bruno Ramon, and Edilson Pimentel.

I am extremely thankful to my brothers from another parents, Nicholas Jimenez and Kavid Singh. I own many thanks for the times they provided warm support and relief in the worst moments.

Thanks God for the wisdom and perseverance he bestowed upon me during this research project, and indeed, throughout my life.

This study was financed in part by the Coordenação de Aperfeiçoamento de Pessoal de Nível Superior - Brasil (CAPES) - Finance Code 001. Last but not least, I would like to acknowledge The University of Texas at Austin.

If perhaps, I forgot someone... thank you to whom it concerns! Thank you all.

"O sonho é que leva a gente para frente. Se a gente for seguir a razão, fica aquietado, acomodado."

(Ariano Suassuna)

RESUMO

Um simulador computacional térmico-mecânico usando o Método de Volumes Finitos baseado em Elementos (EbFVM) foi elaborado para investigar a solidificação de lingotes durante o lingotamento contínuo. O comportamento térmico foi avaliado utilizando a equação transiente bidimensional de condução de calor com mudança de fase, em conjunto com coeficientes de transferência de calor obtidos por meio de um procedimento numérico-experimental. Além disso, a abordagem termo-mecânica inclui três representações inelásticas, baseadas nos modelos plástico de Ramberg-Osgood e viscoplásticos de Odqvist. O simulador foi validado usando vários testes de benchmark, juntamente com a solução analítica para o problema de Stefan. A solução numérica fornecida pelo simulador desenvolvido nesse trabalho foi comparada com a obtida por um simulador comercial. Das comparações, pode-se notar que EbFVM faz predições tão boas quanto a abordagem numérica tradicionalmente empregada para obter a solução de casos que envolvem simulação computacional de sólidos. No contexto de lingotamento contínuo, foram investigadas duas velocidades de fundição e, a fim de melhorar o estágio de resfriamento na zona dos sprays, um novo conjunto de sprays foi proposto para os casos investigados voltadas à prevenção de formação de trincas. O estudo termomecânico fornecido por EbFVM foi capaz de fornecer bons resultados para o perfil de temperatura e estado termomecânico e podem ser usados para resolver problemas causados pelo processo de resfriamento.

Palavras-chave: Lingotamento continuo, Plasticidade, Visco-plasticidade, Método de Volumes Finitos baseado em Elementos

ABSTRACT

A computational thermal-mechanical simulator using the Element based Finite Volume Method Element based Finite Volume Method (EbFVM) has been elaborated to investigate the solidification of continuous casting ingots. The thermal behavior was evaluated using the two-dimensional transient heat conduction equation with phase change in conjunction with a numerical-experimental film coefficients. In addition, the thermal-mechanical approach includes three inelastic representations, which are based in the Ramberg-Osgood plastic and Odqvist's viscoplastic models. The simulator is validated using several benchmarks tests, along with the analytical solution of the Stefan's problem. The numerical solution provided by the proposed in-house simulator were compared with a commercial simulator. From the comparisons performed, one can notice that EbFVM makes accurate prediction as the traditional numerical approach commonly employed to obtain the solution of computational mechanical cases. In the context of continuous casting herein were investigated two casting velocities and in order to enhance the cooling stage, in the sprays zone, as well as the crack formation, a new sprays set were proposed for the investigated cases. The thermal-mechanical study provided by EbFVM is able to provide good results for the temperature profile and thermomechanical state that could be used to address problems caused by the cooling process.

Keywords: Continuous casting, Plasticity, Viscoplasticity, Element based Finite Volume Method

LIST OF FIGURES

LIST OF TABLES

LIST OF ABBREVIATION AND ACRONYMS

AISI	American Iron and Steel Institute
BCC	Body Centered Cubic
BCT	Body Centered Tetragonal
CFD	Computational Fluid Dynamics
CSM	Computational Solid Mechanics
CV	Contol Volume
CVFEM	Control Volume based Finite Element Method
EbFVM	Element based Finite Volume Method
FCC	Face Centered Cubic
FDM	Finite Difference Method
FEM	Finite Element Method
FVM	Finite Volume Method
IHCP	Inverse Heat Conduction Problem
PETSc	Portable, Extensible Toolkit for Scientific Computation
TLE	Thermal Linear Expansion

LIST OF SYMBOLS

ρ	Density
c	Specific heat
∇	Nabla differential operator
L_{ij}	Differential operator
v_i	Velocity vector
$\dot{q}$	Latent heat source
$\bar{\bar{k}}$	Second rank conductivity tensor
L	Latent heat
f_{S}	Solid fraction
$h_{m/m}$	Effectiveness heat transfer coefficient at the metal/mold interface
$k_{\circ}$	Partition coefficient
U	Internal energy
e	Internal energy per unit of mass
K	kinetic energy
Q	Heat
W	Work done
R	Volumetric heat capacity
n_i	Outward unit vector
σ_{ij}	Second rank Cauchy stress tensor
ε_{ij}	Second rank total deformation tensor
ε^{i}_{ij}	Second rank inelastic deformation tensor
ε^{e}_{ij}	Second rank elastic deformation tensor
ε^{th}_{ij}	Second rank thermal deformation tensor
ψ	Helmholtz free energy
s	Specific entropy per unit mass
$\bar{S}$	Entropy

q_i	Heat flux vector
A_i	Hardening thermodynamic force or stress-like isotropic hardening variable
N_ε	Non-dimensional rate-sensitivity parameter
K_ε	Viscosity-like of the material.
μ_ε	Viscosity-related parameter
r_i	Strain-like isotropic variable
$\bar{\varepsilon}$	Strain-like isotropic variable
α	Thermal expansion coefficient
T	Temperature
T_{ref}	Reference temperature
T_m	Melting temperature
T_w	Temperature of the wall
T_{L}	Liquid temperature
T_{S}	Solid temperature
T_{water}	Temperature of the cooling water
T_{env}	Temperature of the environment
c_ε	Specific heat at constant strain
κ_T	Bulk modulus
λ_T, μ_T	Lamé's coefficients
E	Young's modulus
$\dot{m}$	Water flow rate
ν	Poisson rate
Q_i	Activation energy
K_p	Plastic resistance
M	Hardening exponent
σ_y	Initial yield stress
S_{ij}	Deviatoric stress
β_T	Thermal linear expansion

σ_{eq}	von Mises equivalent stress
φ	Dissipation potential
D^{e}_{ijkl}	Fourth rank isotropic elastic modulus
D^{p}_{ijkl}	Fourth rank isotropic plastic modulus
u_i	Displacement vector
δ_{ij}	Kronecker delta
b_i	Body force
t_i	Traction vector
γ	Multiplying factor
F_{ext}	External force
F_{int}	Internal force
N_j	Shape functions

CONTENTS

1 INTRODUCTION

1.1 General Aspects

In manufacturing operations that involve solidification phenomena, equivalent to shape casting foundry, continuous casting and welding process there are several very complex entanglements at macroscopic as well as at microscopic level, between thermal and mechanical stresses. The study of such processes is aggravated, since some of these physical phenomena are still not fully comprehended (KORIC; THOMAS, 2007). In reality, continuous casting is probably the most intricate among all of them and some aspects of its solidification mechanism is the main scope of this work.

Continuous casting technique, which is also called strand casting, is a state-of-the-art technological procedure employed in steel-making, which more than 96% of the steel metallurgy industry all over the world uses (ROCHA, 2017; THOMAS, 2018). A pioneer version of the actual continuous casting was first introduced by Sir Henry Bessemer in the 1857 (SIVARAMAKRISHNAN *et al.*, 2000; BUSCHOW *et al.*, 2001). This technique became popular in the 1960s and replaced the previous solidification method so-called stationary casting or ingot casting. In the stationary casting, the metal production is performed by pouring molten metal into stationary molds to form ingots. Since the introduction of continuous casting, it has been enhanced to achieve high quality, productivity, and low cost over the traditional one (AVEDESIAN *et al.*, 1999; KORIC, 2006; PIMENTA, 2014; LEE, 2018). Another advantage of continuous casting is associated to its flexibility, since the addition of others alloys allows the industry to obtain different steel grades during the continuous casting operation, for instance. The most recent feature implemented in this process is the continuous strip casting of steel, which grants the production of metal strips with thicknesses in the order of millimeters (GE *et al.*, 2013).

Despite the fact continuous casting is today a very popular technique in the production of metals, a considerable amount of essential improvements still remains to minimize the presence of defects and to maximize the production (KORIC; THOMAS, 2007). According to Luo *et al.* (2008) there are several issues that could influence the productivity, as well as the steel quality. However, the most import ones are associated with the cooling process. Drawbacks associated with the cooling process are probably responsible for uneven shell growth that affects directly the heat transfer, since it could allow the formation of gaps between the strand and the

walls of the mold. Shell irregularities are able to conduct to longitudinal cracks and breakouts (ZHU, 1996; KORIC, 2006; DU *et al.*, 2018b). Many authors believe that such phenomena occur in the early stages of the solidification (ZHU, 1996; KORIC, 2006; KORIC; THOMAS, 2007; KORIC; THOMAS, 2008; DU *et al.*, 2018a).

An efficient and extensively procedure used to predict crack formation during continuous casting of metals is the correct determination of temperature, deformation, and stress behavior (LUO *et al.*, 2008; DU *et al.*, 2018b). Due to the high cost of experiments in a production plant, which are also performed under harsh conditions, the investigation of such physical aspects become more suitable to be determined by numerical simulations. Even though in recent years a considerable number of modeling applications have been applied to different stages of the continuous casting of steel, and the computational capabilities had been enhanced, there is no complete numerical model available. The description of the physical phenomena involved is still a very challenging task (KORIC; THOMAS, 2007).

From computational point of view, one of the greatest challenges to accurate determine the thermomechanical behavior at elevated temperatures is the application of a satisfactory model that takes into account the complex relation between stress, strain, and time (FACHINOTTI; CARDONA, 2003). One of the simplest models considers only reversible deformations i.e., the elastic description. Nonetheless, the elastic region in metals decreases when the temperature increases and vanishes at the melting point. Additionally, metals at elevated temperatures present a singular rate sensitive deformation. Therefore, a numerical description of such phenomena become more realistic with the introduction of rate dependent strain i.e., viscoplastic models, which takes into account irreversible time-dependent deformations.

1.2 Objectives

1.2.1 General Objectives

The main objective of this dissertation is to develop a numerical simulator, under the view point of EbFVM, that analysis the thermal and mechanical behavior as the solidification occurs during the manufacture of steel, in a process called continuous casting.

1.2.2 Specific Objectives

The main objective can be better split into the following specific objectives:

- Study of the thermal aspects during the cooling stages using the two-dimensional transient heat conduction (conservation of energy) equation with phase change in conjunction with numerical-experimental film coefficients;
- From the view point of the thermal behavior, it is also calculated the thermal-mechanical distribution in order to verify the elastic-plastic-viscoplastic stress state;
- In addition, it is expected that the simulations must be capable of to provide a more efficient cooling set, for this particular use, to better solidify low carbon steel ingots, by reducing some causes liked to the presence of defects.

1.3 Short view of this work

Since crack formation can occur with total deformation in the order of 2%, the small strain hypotheses is widely applied in numerical models that involves continuous casting procedure (ZHU, 1996; FACHINOTTI; CARDONA, 2003). Under the hypotheses of plasticity, this work assumes Ramberg-Osgood model, the classical second invariant, J_2, and associative theory of plasticity over small strain assumption. Additionally, the viscoplastic model is based on the Odqvist's viscoplastic law. The data for both plastic and viscoplastic model are fitted from the work of Kelly *et al.* (1988) and Huespe *et al.* (2000).

This project was first introduced by Anjos (2013), which evaluated the heat transfer coefficient at the strand/mold interface using one-dimensional Finite Volume Method (FVM) and C++ language. From these coefficients, the thermal and thermal-elastic behavior were analyzed using triangular elements in conjunction with Element based Finite-Volume Method (EbFVM), and Fortran language by Pimenta (2014). In this work is introduced a more mature implementation that covers plasticity and viscoplasticity models. The implemented scheme is further applied to the solidification phenomena during continuous casting of low carbon steel, evaluating quantitatively the thermal and mechanical behavior.

1.4 Motivation & Originality

A fair number of phenomena that have practical interest in science and engineering are successfully described by using mathematical models properly. In classical physics, for instance, a very important mathematical equation that is able to accurately predict various aspects of the behavior of solids and fluids is the conservation of linear momentum (VOLLER, 2009;

CRISFIELD *et al.*, 2012). Another important relation is the conservation of energy equation, which is also capable of analyze, at the macroscopic level, the thermal distribution in solids and fluids domains. Additionally, the solidification mechanism in the continuous casting technique is well described by the application of these equations.

Nevertheless, the exact solution of the most physical models is restricted to a great number of simplifications. More precisely, as the physical model description of an arbitrary natural process became close to the observed phenomena, the complexity is increased due to a massive manifestation of a set coupled of nonlinear equations. This issue is addressed by the application of numerical approaches which, through approximated solutions, permit the description of a significant deal of complex problems in areas such as engineering, mathematics, and physics (PIMENTA, 2014).

Experimental observations also play an important role in science and engineering. Empirical practices give a valuable insight of the process being analyzed and their methodologies include capabilities to support, refute, or validate a hypothesis. Typically, these procedures are designed to minimize the effect of multiples-variables to a single independent variable i.e., the observations take place into a controlled environment which is the laboratory. The advantages of numerical applications over entirely experimental studies lies in the flexibility of the numerical models, which in some extent could be decomposed in multiples physical sources, where each source is separately studied. Another important disadvantage aspect associated with experimental procedures over numerical ones is the relative high cost. However, numerical approaches are validated with exact solutions as well as experimental results. Not to mention, empirical techniques are undoubtedly indispensable methodologies that allow the calibration of the physical models.

In particular, the investigation of the thermal and mechanical behavior during the solidification stages of metals, in the continuous casting scenario, is almost an impracticable task for empirical procedures alone due to the harsh environment (THOMAS, 2018). On the other hand, computational methods to modeling those mentioned aspects require the application of many complex physical phenomena which lead to numerical difficulties (ZHU, 1996). Therefore, the necessity of the application of a stable and accurate approach added with some model simplifications are essential. The EbFVM is a very promising method in Computational Solid Mechanics (CSM) (FILIPPINI *et al.*, 2014; PIMENTA; MARCONDES, 2019), since its introduction in the field in 1991 by Fryer *et al.* (1991). This method is successfully used in

Computational Fluid Dynamics (CFD) (TAYLOR *et al.*, 2003) due to its local conservation of the physical properties being evaluated granted to the integration procedure used (MALISKA, 2004).

Throughout the literature there are important contributions on the thermal and thermal-mechanical analyses employed to the enhancement of the cooling stages in the context of continuous casting process, as they can be seen in Bolle and Moureau (1946), Soeyanto (1995), Chen *et al.* (2009), and Anjos (2013). Herein, the EbFVM is used to study the two-dimensional thermal field in conjunction with numerical-experimental heat transfer coefficients, and the thermal-mechanical behavior during the solidification stages in continuous casting of ingots. In practice, a half of the ingot's cross section is monitored from the view point of Lagrangian frame of reference and analyzed under plane strain and elastic-viscoplastic assumption. This investigation is applied to improve the heat transfer effectiveness by presenting cooling alternatives which could avoid or minimize the presence of off-corner and midway cracks.

It is important to emphasise that EbFVM has been received a lot of attention in linear elastic CSM applications. On the other hand, just few works have addressed the use of EbFVM in nonlinear CSM area (TAYLOR *et al.*, 1995; TAYLOR *et al.*, 2003; PIMENTA; MARCONDES, 2019). The application proposed in this work, therefore, can be considered as an important contribution in this field, since we employed the aforementioned method to solve elastic-plastic-viscoplastic problems. As an additional motivation, according to the best of this author's knowledge this is the first application of EbFVM on the solidification process within the context of continuous casting technique.

1.5 Outline of the Dissertation

The rest of this thesis is structured as follows:

Chapter 2 gives an elementary description of the microstructure of iron and carbon alloys during the solidification. A general view about the cooling mechanism, in each stage of the continuous casting of steel, and standard conditions of this industrial process are also discussed. Subsequently is presented particular aspects that are subject of this application.

In Chapter 3, the physical models used to characterize the thermal and the stress state behavior are introduced. A necessary thermodynamics summary that gives a better context over the continuum mechanics is also reviewed.

Chapter 4 presents a brief historical outlook of the EbFVM approach. This chapter likewise contains the EbFVM integration procedure and its application to the non-linear thermal and mechanical models.

Chapter 5 is meant to display the benchmark test cases which are used to validate the thermal-mechanical numerical model.

The numerical results and cooling alternatives for the secondary stage of the continuous casting of ingots is presented in Chapter 6.

In Chapter 7, the conclusions, from the discussed results in the previous chapters, are presented. It is also laid out the model's validity and contains suggestions for improvements and future work.

2 SOLIDIFICATION PROCESS IN CONTINUOUS CASTING

2.1 Carbon steel during-phase transformation

According to the amount of carbon atoms (C) dissolved into the solid iron (Fe), there is a theoretical separation that distinguish between steel and cast iron. If the amount of C diffused in the liquid iron remains with concentrations levels well below 2.14%, the product is steel, and if concentrations levels is above that, the final product is cast iron. Such division can be seen in Fig. 1 (CALLISTER; RETHWISCH, 2011). In the illustration bellow is presented as portion of the iron-carbon phase diagram, which is often labeled as the Fe–Fe_3C phase diagram.

Figure 1 – Fe-Fe_3C phase diagram with schematic representation of a BCC and FCC unit cells.

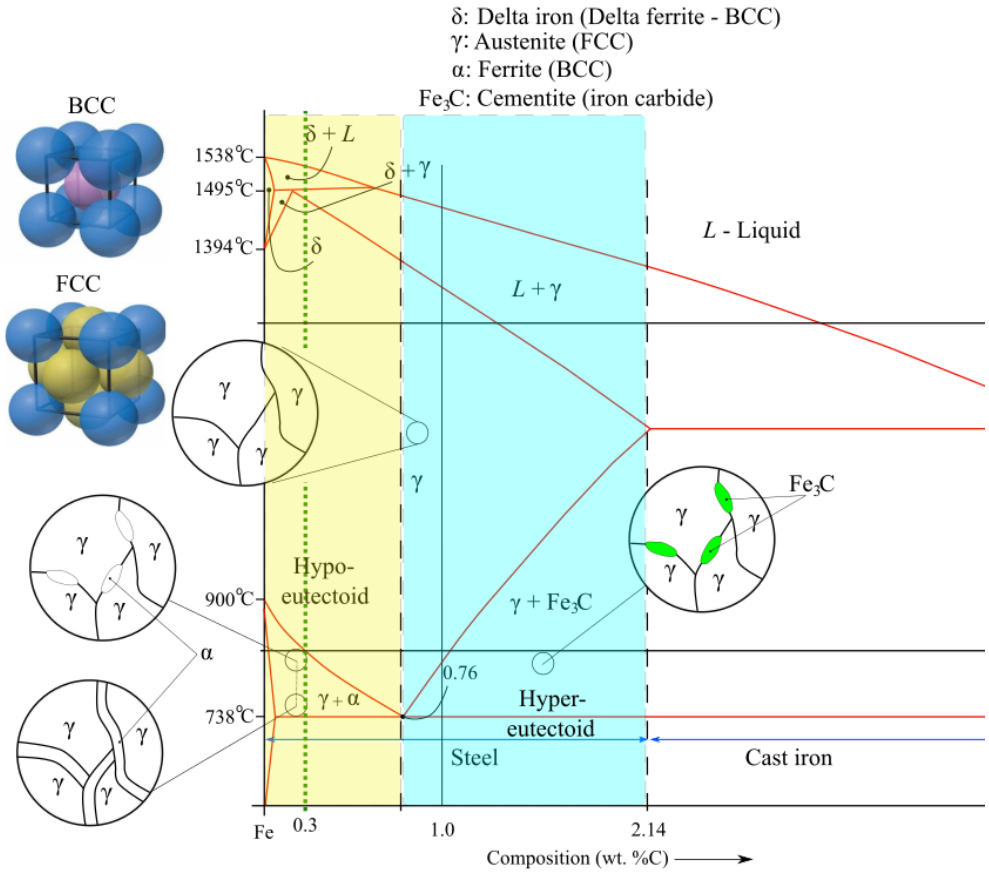

In particular, during the cooling of alloys containing ~ 0.3 wt.% carbon (see Fig. 1), the first stage of the solidification concerns to the nucleation of primary δ-dendrites (δ-ferrite), which presents a Body Centered Cubic (BCC) crystalline structure, in the liquid phase, $L \rightarrow \delta + L$. During this solidification stage there is a reheating due the heat released from the growing nuclei in the course of recalescence, which is responsible to ceases the nucleation

process. The existing nuclei grows rapidly into dendritic grains, encroaching on each other at the end of recalescence. As the temperature decreases, austenite (γ) which presents Face Centered Cubic (FCC) crystalline structure, starts to precipitate from the δ phase $(\delta \rightarrow \delta + \gamma)$ until the last phase one is entirely transformed into austenite. In Fig. 2 is illustrated the growth of δ-dendritic in the liquid phase, as well as initial formation of austenite (γ) from δ phase. The alloy is further cooled passing through the so called austenite zone until the temperature is favorable to precipitation of α-ferrite phase $\alpha \rightarrow \gamma$. In this stage, steel having carbon concentration between 0.02 and 0.76 wt.% is further classified as hypo-eutectoid. Finally, the cooling stage is completely accomplished when the remaining austenite is converted into pearlite, which appears through nucleation at austenite interfaces as a mixture of ferrite and cementite (Fe_3C – or iron carbide) phases (ZOU; TSENG, 1992; SOEYANTO, 1995).

Figure 2 – Initial stage of the solidification process. Growth of primary ferrite and subsequent austenite formation.

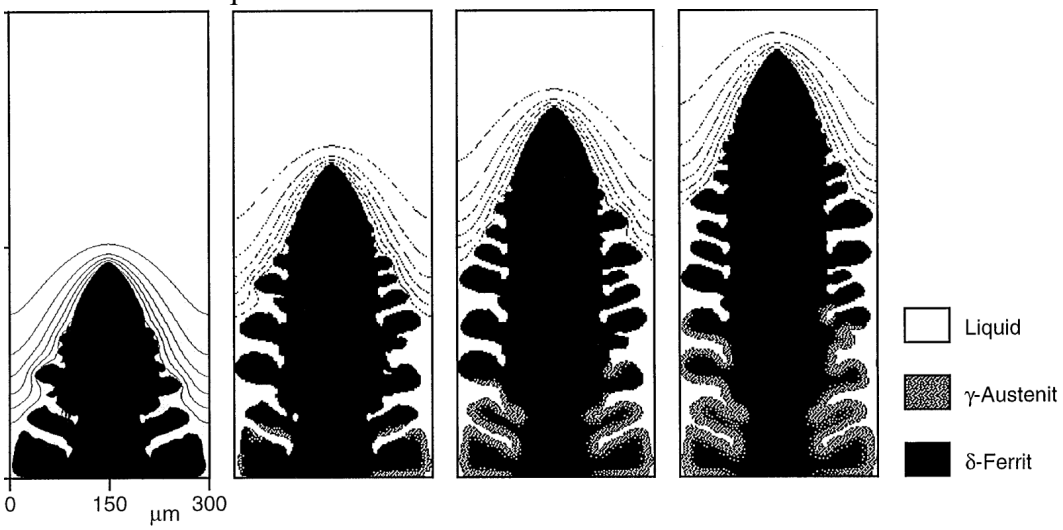

Source: Tiaden (1999).

Essentially, steels are alloys constituted mostly by iron (Fe) and carbon (C) elements, which are classified accordingly with the weight percent (wt.%) of C added to Fe. The dissolution of C in the Fe structure is dependent upon temperature. Since pure Fe has its melting point at 1540 °C, C (graphite) readily dissolves into the liquid iron. As the solidification takes place, this mixture undergoes several microstructural modifications, in which C atoms could be embedded within the unit cells of solid iron. When C atoms do not react with Fe there is precipitation of Fe_3C, since iron carbide is formed as the solubility limit of carbon in $\alpha-$ferrite is exceeded at temperature of 727 °C (CALLISTER; RETHWISCH, 2011). Each phase configuration leads to materials with different mechanical properties and consequently distinct engineering applications.

When the solidified steel (0.02 - 0.76 wt.% C) presents a temperature well below 738°C, the previous austenite, when cooled slowly enough, is decomposed into a mixture of ferrite, which is soft and ductile, and cementite, hard and brittle. Such phase combination is called pearlite and has a lamellar structure distinguished by a pattern of alternating ferrite and cementite layers. Mechanically, pearlite has properties intermediate between the soft, ductile (from ferrite) and the hard, brittle (from cementite) (CALLISTER; RETHWISCH, 2011). It is pointed out that hypo-eutectoid steel is constituted of pro-eutectoid ferrite and pearlite and the amount of both is dependent upon the carbon concentration. On the other hand, a fast cooling (quenching) from austenite phase does not allow C atoms to diffuse out of the crystalline structure in enough quantities to produce cementite. As a consequence of quenching, the FCC structure of γ-Fe transforms into a highly strained Body Centered Tetragonal (BCT) form called martensite. Mechanically, martensite is extremely hard and brittle (KHAN, 1972).

2.2 General aspects of the cooling process in continuous casting

Continuous casting is the solidification technique of metals and alloys most used worldwide in the steel industry, as already mentioned. In this technique, molten metal is solidified continuously into a semi-finished alloy shaped as ingot, billet, bloom, or slab. The mean feature of this metallurgical procedure is associated with the dynamics of the solidification, since it is responsible for a significantly reduction of costs as well as the manufacturing time in comparison with the outdated solidification technique called stationary casting.

The dynamic solidification in the continuous casting is due to the cooling mechanism, which is responsible for a continuous heat extraction as the strand descends through the caster machine guided by a large number of rolls (SPUY *et al.*, 1999; MAZUMDAR; RAY, 2001), see Fig. 1. In the course of solidification, the energy released is associated with the extraction of sensible and latent heat. During this path, in general, the strand is subjected to three cooling zones. The first one (primary stage) is composed by a copper mold that is open-ended and water-cooled; the liquid metal initiates the solidification process in this level. At the mold outlet, the solidified shell must be thick enough to withstand the ferrostatic pressure (BRIMACOMBE *et al.*, 1984; MAZUMDAR; RAY, 2001; CHAUDHURI *et al.*, 2010; MORO *et al.*, 2017; THOMAS, 2018). In the secondary cooling, the heat loss is provided by a combination of radiation and several zones with independent controlled water sprays. This step is responsible for the maintenance of the shell growth as the strand moves towards the tertiary cooling stage, where the cooling process

is dominated by radiation and natural convection and the solidification process is ultimately finished (GARCIA *et al.*, 2006).

Figure 3 – Schematic representation of the continuous casting machine.

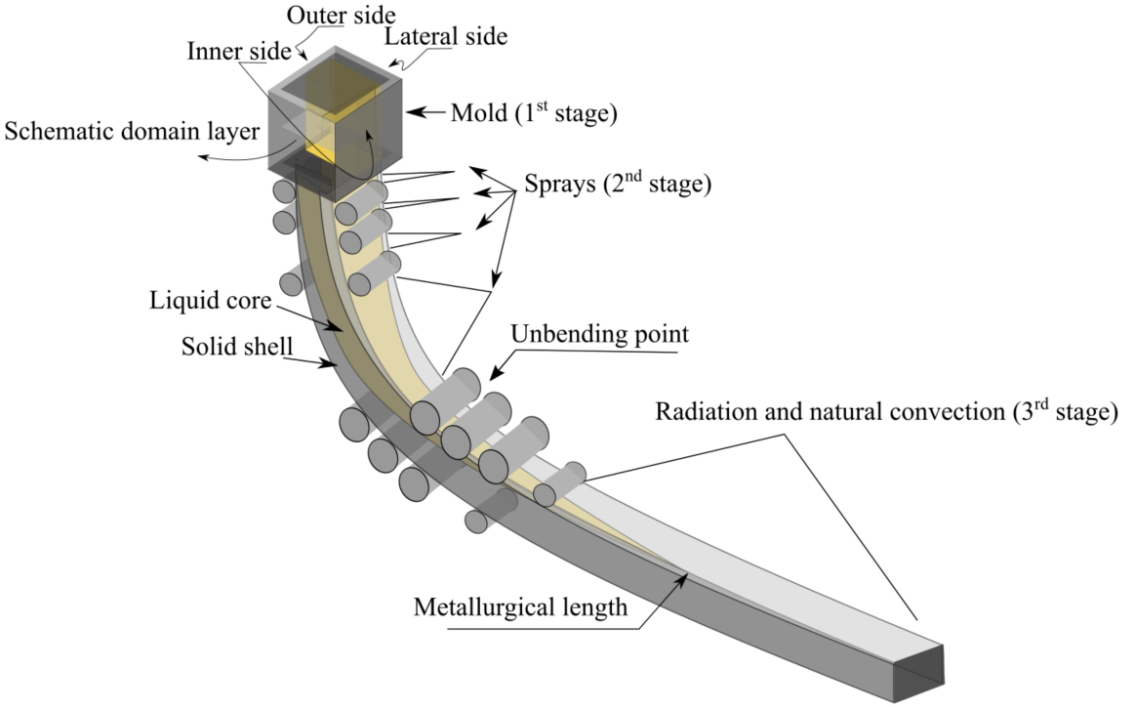

The cooling stages are vital to avoid flaws in continuous cast semi-finished products. In the course of the solidification, which causes phase change, as discussed in Section 2.1, not only the strand has its microstructure modified, but also the amount of stress that the strand is able to support without fracturing also changes; in other words, the ductility is affected. For carbon steel, there are three major thermal zones that need to be considered: the high temperature ($1200\ ^\circ\text{C} < T < T_s$), intermediary temperature ($850\ ^\circ\text{C} < T < 1200\ ^\circ\text{C}$), and low temperature ($700\ ^\circ\text{C} < T < 850\ ^\circ\text{C}$) (SOEYANTO, 1995; SILVA, 2016). Where T_s denotes the solidification temperature, which value is the range of $1495\ ^\circ\text{C} < T_s < 1500\ ^\circ\text{C}$.

The embrittlement presented in the high temperature interval, in particular, induces fractures formation under small deformation as 1%, due to the highly sensibility of the solid/liquid solidification front (SOEYANTO, 1995). This severe lack of ductility is experienced own to the presence of microsegregation of S (Sulfur) and P (Phosphorus) in the interdendritic liquid films, which causes local reduction of the solidus temperature (SILVA, 2016). On other hand, in the intermediate temperature range, the ductility loss is caused essentially by the presence of certain amount of precipitated elements, where the most influential ones are the precipitation of nitrates and sulfates at the austenite grain boundaries (THOMAS *et al.*, 1986). In the low

temperature zone, region characterized by the two-phase austenite-ferrite, the embrittlement is due to the weakening of the austenite grain boundary. This is attributed to the strain concentration of primary ferrite films (THOMAS *et al.*, 1986; SILVA, 2016) since at the same temperature, austenite is less ductile and has more resistance when compared to ferrite. Such phenomena are associated in part to the atomic diffusivity of ferrite, since its BCC structure has more slip systems (48) than FCC austenite (12) (ERICSON, 1977; SOEYANTO, 1995; CALLISTER; RETHWISCH, 2011).

2.3 Mold region or primary cooling stage

The main functionalities of the mold are to accommodate the liquid metal that is poured from the tundish via the nozzles, as well as to start the heat removal. In the mold region, Fig. 4, the heat extraction aims the formation of a solid shell, which must be capable of withstand the metal shrinkage, the ferrostatic pressure, and the bulging of the strand at the region of contact with the rolls.

Figure 4 – Representation of fluid-flow phenomena inside of the strand.

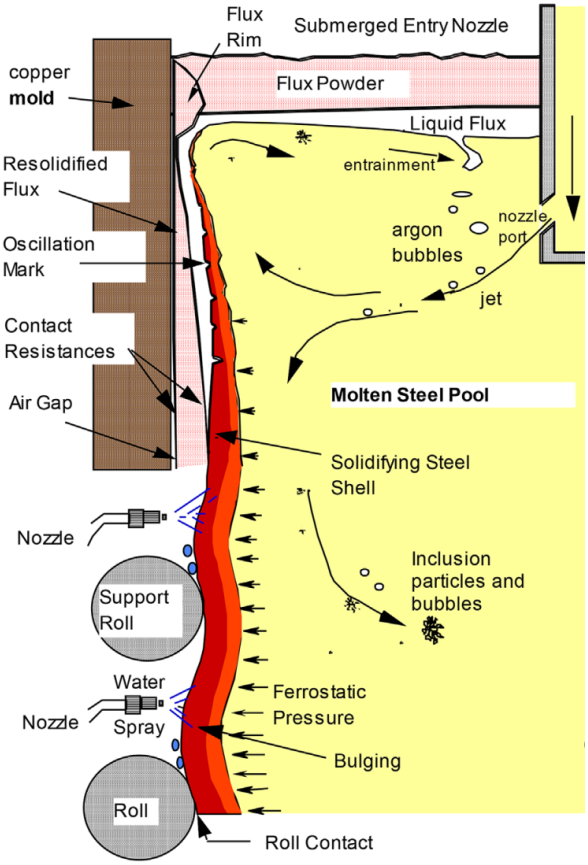

Source: Thomas (2002).

Due to the volumetric shrinkage and ferrostatic pressure, irregularities in the solid shell can arise. This phenomenon leads to a gap formation, which influences directly the heat flux removal (BARCELLOS, 2011; ANJOS *et al.*, 2018). Since the heat transfer is mainly governing by conduction that needs to go through the interfacial gap, it can induce a non-uniform solidified shell, provoking off-corner cracks that may lead to break-outs at the outlet of the mold (Fig. 4). Another common source of defects resides in the reheating, which may cause midway cracks formation, as the strand pass through the so-called inter-zones (CHAUDHURI *et al.*, 2010); the inter-zones can be defined as a transition to a cooling region with less heat transfer efficiency. In the reheating zone, the thermal variation must be retained below 150 ^{o}C for certain alloy composition, since the surface temperature of the stand is out of the low ductility zone (THOMAS *et al.*, 1986; SOEYANTO, 1995; GARCIA *et al.*, 2006; CHAUDHURI *et al.*, 2010).

Many authors believe that solidification at mold stage is the heart of the continuous casting process (BRIMACOMBE *et al.*, 1984; ZHU, 1996). To prevent flaws, numerical applications were used to investigate the thermal and mechanical behavior, where the pioneers works in this area were performed by Brimacombe (1976), Grill *et al.* (1976), Brimacombe and Sorimachi (1977), and Tszeng and Kobayashi (1989). More recent models apply a greater set of constitutive equations, which are calibrated using plant measurements. A simple approach is the employment of thermocouples to calibrate heat transfer models and to evaluate films coefficients via inverse models, as can be seen in Du *et al.* (2018a), Anjos *et al.* (2018) and Wang *et al.* (2016). It is known that the physical phenomena that takes place inside the mold is very complex and highly non-linear and such issue is probably the reason that there is no complete simulator available (for this industrial application). The simulator introduced in this work also presents simplifications and the complete description of the physical relations used as well as their simplified versions adopted are discussed in Chapter 3.

2.4 Sprays region or secondary cooling stage

The secondary cooling region is designed to maintain the strand shell growth. As it was mentioned, the solid shell must have sufficient strength to resist high levels of stress concentration due to bulging, bending, and straightening as the strand exit the mold (CHEUNG, 1999). The cooling mechanism is provided by a series of water sprays and water cooled rolls units, as it is illustrated in Fig. 2. Due to this process, the secondary cooling stage is responsible for the extraction of the highest amount of latent heat (BEZERRA, 2016).

Figure 5 – Schematic representation of the secondary cooling stage.

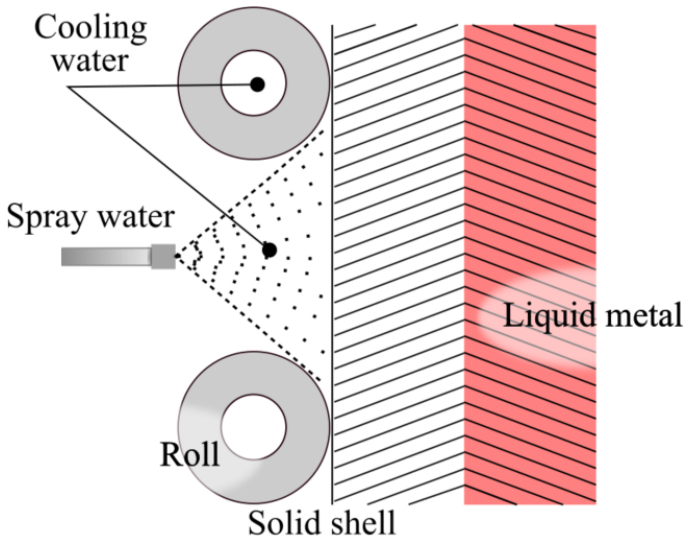

In the sprays region, another important issue is to prevent the formation of surface and center cracks as well as improper shape. In order to accomplish this task, the spray water flow should be regulated in a way that the system could control both temperature and thermal gradient levels (SOEYANTO, 1995). In fact, temperature control is essential as the strand pass through the secondary zone, since at the high temperature region (see Section 2.6) the phase transformation of $\gamma \rightarrow \alpha$ makes the solid shell lose the ability to resist certain loads magnitudes. These are internal and external loads applied by the casting machine. It is also fundamental to control the gradient of temperature, since this phenomenon account for the thermal strains. Depending upon the magnitude of the gradient of temperature, the thermal strain could exceed the strength of the metal causing the formation of cracks. In addition, excessive cooling could also result in high thermal strains (SOEYANTO, 1995). According to Soeyanto (1995), the surface temperature along the ingot must be above 850 °C to prevent the formation, in particular, of transverse cracks, which has its favorable scenario during the transformation of $\gamma \rightarrow \alpha$.

The cooling rate can be determined through the conservation of energy equations, which contain relevant parameters, such as the convective heat transfer coefficient for both water spray and water flux. In addition, a significant portion of the extracted heat strongly dependent on the water flux from the spray nozzles (GRILL *et al.*, 1976; BRIMACOMBE *et al.*, 1984; SOEYANTO, 1995; GARCIA *et al.*, 2006; BEZERRA, 2016). To each operational casting condition, as casting speed, initial casting temperature, and steel grade, changes in the heat flux also have to be made, since these particular circumstances introduce different solidification mechanisms.

Few works are devoted exclusively to the secondary cooling. In particular, Okuno *et al.* (1987) used a spray control apparatus based upon the heat transfer equations, in which the thermal behavior was studied during the casting operation. Another important contribution includes the work of Petrus *et al.* (2011), who applied a real-time numerical (using one-dimensional model) simulation of heat transfer and solidification process to present a new system to control secondary cooling water sprays in continuous casting of thin steel slabs. More recently, Hardin *et al.* (2003) introduced a two-dimensional heat transfer model for transient simulation in order to dynamically control the water flow in the secondary spray cooling.

2.5 Natural convection and radiation region or tertiary cooling stage

As the strand exits the secondary cooling, it enters in the so-called tertiary zone, where the heat extraction is made by the contact with rolls, as well as radiation and natural convection. This stage is also characterized by the straightening process, in which a great amount of deformation is applied to the ingot. The strand, at this point, continues to solidifies, since its core remain liquid and the main concerns are the quantity of reheating experienced by the surface, as well as the temperature of strand at cutoff point. In order to avoid transverse cracks, the core of the strand should be solidified at the unbending point (GARCIA *et al.*, 2006; BEZERRA, 2016).

2.6 Continuous casting metallurgical criterion

In order to achieve a desirable solidification outcome during the continuous casting process, certain criteria must be satisfied. In the literature, there are well-known suitable guidelines that help to prevent flaws in the semi-finished steel cast products. A few of these criteria were briefly mentioned in the introduction and they are dependent of the chemical composition. In context of the application proposed herein, they can be organized as follows:

I. **Minimum shell thickness of ingots at the outlet of the mold**

   According to Chaudhuri *et al.* (2010), the amount of heat extracted from the strand as it passes through the mold (primary cooling region) is around 5% of the total, which makes this stage an important step concerning the ingots quality (RAY *et al.*, 2004; BRIMACOMBE, 1976). The complex heat transfer of the mold stage depends, among other things, of the air gap between the strand and mold walls, which increases the thermal

resistance and decreases the heat transfer at the metal/mold interface. As the strand is pulled out by the rolls at the mold exit, the shell has to be thick enough to support the compressive stress and at the same time the ferrostatic pressure (CHEN *et al.*, 2009). Therefore, to reduce breakouts, at the exit of the primary cooling stage, the minimum solid thickness needs to be 10 % of the strand's cross. Specifically, for ingots with cross section of 100 mm $\times$ 100 mm, the shell thickness of 10 mm has to be attained (SANTOS *et al.*, 2003; SILVA, 2016).

II. **Temperature at the unbending point**

At the strengthener (or unbending point), the solidified strand shell is subjected to a high level of stress; compression (inner radius) and tension (outer radius). This amount of stress can lead to transverse cracks at the surface of the strand (GARCIA *et al.*, 2006; CHEN *et al.*, 2009; BEZERRA, 2016; SILVA, 2016). To avoid the formation of cracks in this stage, the temperature of the surface must be in the appropriate ductility temperature zone, which corresponds to the interval 850 °C $< T <$ 1200 °C, the so-called intermediary temperature range.

III. **Inter-zone reheating**

As the strand moves throughout the casting machine, the extracting heat rate changes at each cooling stage. When the strand arrives at a new cooling zone, the heat transfer efficiency decreases, causing a redistribution of the temperature from the core to the strand's surface, the so called reheating effect. The most pronounced reheating occurs during the entrance of the strand in the third zone and its mechanism leads to the expansion of the inner solid shell, imposing a tensile strain. Depending upon the temperature range that the surface undergoes during the reheating, midway cracks formation may arise (KULKARNI; BABU, 2005). This issue can be avoided by keeping the reheating below 150 °C as long as the surface's temperature is outside of the low ductility zone (SOEYANTO, 1995; SPUY *et al.*, 1999; CHEN *et al.*, 2009; CHAUDHURI *et al.*, 2010).

IV. **Metallurgical length**

As pictured in Fig. 3, the metallurgical length is characterized by the solidification of the strand's core. Therefore, to avoid shrinkage, the strand must be completely solidified before the cutoff point. Moreover, the entirely solidification after the strainer may lead to center crack formation (BRIMACOMBE; SORIMACHI, 1977; SILVA, 2016).

2.7 Issues in continuous casting

In this section is discussed the formation mechanisms of the most common defects in continuous casting of steel namely, cracks formation, breakouts, and Rhomboidity.

2.7.1 Crack formation

Cracks are considered to be a major problem during the solidification in continuous casting (BRIMACOMBE; SORIMACHI, 1977; KUMAR, 1991). These defects can be seen located at every place in cast steel, some types of cracks are illustrated in Fig. 6.

Figure 6 – Schematic diagram of a rhomboid ingot showing various types of cracks.

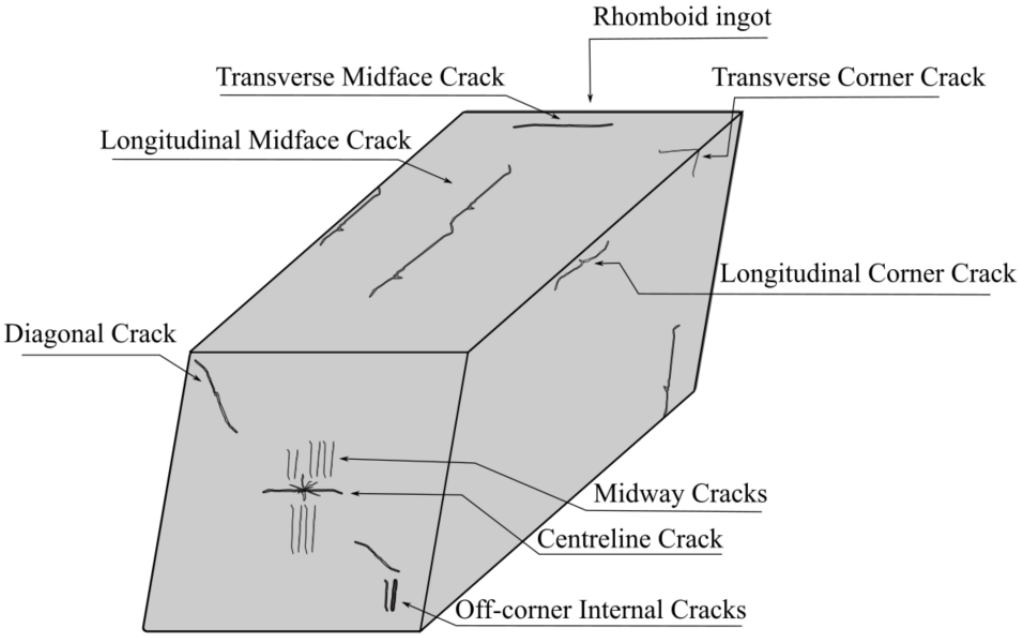

As pictured in Fig. 6, cracks formation may be internal and superficial. Internal cracks result from high loads tensile strains and stress on the solid regions that are in high temperature zone (BRIMACOMBE; SORIMACHI, 1977; KUMAR, 1991). Accordingly to the position within the strand, internal cracks can be further classified as:

I. **Diagonal Cracks** – The mechanism of diagonal crack formation is related to unsymmetrical cooling i.e., it occurs when two adjacent faces cool more rapidly then the others ones, which cause the ingot to contract and generates a diagonal strain between the colder faces. In cases where the magnitude of the strain is large enough, the strand deforms assuming a rhomboid shape (Fig. 6) with an acute angle between the colder faces and an obtuse angle between the hotter ones. In general, diagonal cracks run between the obtuse corners of

a rhomboid strand's section. In some cases these cracks may increase outwards towards the corners to form longitudinal cracks (BRIMACOMBE; SORIMACHI, 1977; KUMAR, 1991);

II. **Midway Cracks** – These defects are also called radial streaks, halfway cracks, and ghost lines. Midway cracks are produced by reheating of the surface of the strand, which causes surface expansion (SOPHER, 1958). In the interior, hotter and weaker regions of the solid shell (within the high temperature zone), are more likely to crack in the face of tensile strain cased by this expansion;

III. **Centreline Cracks** – Such defects are also known as core cracks, which appear in the central region of a cast steel section (Fig. 6) and they are formed at the and of solidification (SILVA, 2016). These problems may be unfolded when sudden decrease of the core's temperature at complete solidification, which could generate strains that can cause crack;

IV. **Off-corner Cracks** – The location of these cracks is about 15 mm from a given corner and also 4 to 6 mm from the strand's surface (KUMAR, 1991). According to Brimacombe *et al.* (1980), the mechanism of off-corner crack formation is related to bulging of a given strand's face in the lower part of the mould.

It is also convenient to notice that surface cracks, as illustrated in Fig. 6, can be classified as follows:

I. **Transverse Cracks** – These cracks are usually seen lactated at the midface or near the corners on the strand's surface (Fig. 6). Transverse defects are linked to the nature of oscillation marks as well as sticking and/or binding of the ingot in the mold (BRIMACOMBE *et al.*, 1980);

II. **Longitudinal Corner Crack** – These cracks can be seen placed at the hotter, obtuse corners of the strand. Regarding the mechanism of longitudinal corner crack formation, two process have been suggested. The first one is related on the formation of a considerable large mold/shell gap nearby the corners which imposes a reheating of the ingot's surface to temperatures approaching the high temperature zone of low ductility. The thermal shrinkage, which generates tensile stresses, and ferrostatic pressure are able to lead to the formation of cracks if the low ductility temperature zone above 1200 °C is achieved (BRIMACOMBE *et al.*, 1986; KUMAR, 1991). The second mechanism is based to rhomboidity, which is associated to oscillation marks on the strand's surface (KUMAR, 1991).

III. **Longitudinal Midface Crack** – Such defect is located on the midface of ingots and it is parallel to the withdrawal direction. Longitudinal midface crack is related to the existence of scratch gouge marks on the mold walls which is able to locally increase the gap size mold/shell adjacent to it. This mechanism leads to a severe decrease in the heat extraction rate over a small localized region on the strand's surface. Consequently, this area reheats and expands while the surface temperature reaches the high temperature zone. The colder steel surrounding the strand's surface restrain this expansion, which generate tensile stress at the solidification front leading to crack formation.

2.7.2 Breakouts

Breakouts are ruptures of the solid shell which imposes molten metal flows out. Such problem is considered to be a serious issue in the way that not only stops the production but it is also a risk. The mechanism associated with breakouts are linked to thin and weak solid shell at the mold outlet (BRIMACOMBE, 1976). Breakouts can be related to the presence of cracks specially if these cracks play as stress concentration sites (KUMAR, 1991).

2.7.3 Rhomboidity

Strands with severe rhomboid shape, Fig. 6, can be aggravated in pusher-type reheat furnaces and during rolling, since the corners may bend over and generate seams in the final product. The mechanism associated with the generation of rhomboidity involves oscillation mark formation as well as non-uniform heat extraction in the primary and the secondary cooling region (KUMAR, 1991). This problem can be originated in the mould and/or the sprays and it is associated with non-uniform shell growth in the primary region and/or asymmetric spray cooling.

2.8 Investigation outlook

As previously mentioned, this work focus on the investigation of the thermal and stress state behavior in the course of solidification of steel. In order to provide a more accurate description of the thermal-mechanical process, the proposed numerical model employs bi-linear quadrilateral elements in conjugation with unstructured meshes. The numerical domain admits half of the strand's cross section, which intends to verify possible uneven thermal and mechanical

behavior, as illustrated in Fig. 7.

Figure 7 – Illustrative locations of the tracking points in the numerical domain.

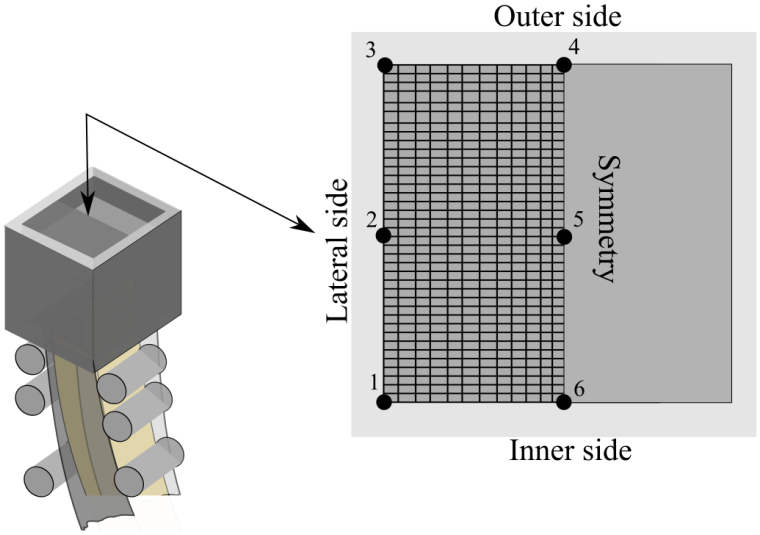

In order to have a comprehensive thermal description, the simulator includes a numerical-experimental film coefficient for each cooling stage of the continuous casting. In the mold region, in particular, distinct film coefficients for the inner, outer, and lateral sides are used. These heat transfer parameters were estimated by Anjos *et al.* (2018) during the casting of low carbon steel ingots using the Inverse Heat Conduction Problem (IHCP) in conjunction with FVM. On the other hand, in the sprays zone, the empirical model of Bolle and Moureau (1946) is adopted and, in the tertiary zone, a constant heat effectiveness based on the work of Brimacombe (1976) is applied. In the thermal stress context, three models were incorporated in the simulator namely, Ramberg-Osgood law assuming both isotropic hardening and perfect plasticity as well as the representation using Odqvist's viscoplastic law.

As for the continuous casting application, the simulations were performed assuming AISI[1] 1028 steel and two casting conditions. In the first one, the casting velocity of 2.8 m/min and initial temperatures of 1545 °C are employed; and in the second case, the casting velocity of 3.2 m/min and initial temperatures of 1535 °C are used. Moreover, to better capture different gradients of temperature, especially in the mold region, six points at the stand's surface, as shown in Fig. 7, are tracked over the entirely simulation.

[1] American Iron and Steel Institute (AISI).

3 PHYSICAL MODEL

In this section is presented the general physical models used to describe the thermal and mechanical behavior under the elastic-visco-plastic and infinitesimal deformation assumptions.

3.1 Heat transfer equation

From the first law of thermodynamics is possible to obtain the conservation of energy for a continuum material. Such representation has been proven suitable in the analysis of the temperature behavior of a body under different phases changes. This conservation principle assumes the form (RODRIGUEZ *et al.*, 2009),

$$\frac{\partial(\rho c T)}{\partial t} + \rho c(\mathbf{v}\cdot\nabla)T = \nabla\cdot\left(\bar{\bar{k}}\cdot\nabla T\right) + \dot{q}, \tag{3.1}$$

where T is the temperature, t is the time, $\bar{\bar{k}}$ is the second order thermal conductivity tensor, c is the specific heat at constant pressure, ρ is the metal density, $\mathbf{v}$ is the liquid steel velocity, and $\dot{q}$ is the latent heat source due to the phase change.

For an isotropic material, the conductivity tensor $\bar{\bar{k}}$ can be rewritten simply as follows

$$\bar{\bar{k}} = k(T)\begin{bmatrix} 1 & 0 \\ 0 & 1 \end{bmatrix}. \tag{3.2}$$

In addition, in the application proposed herein, the advection term $\rho c(\mathbf{v}\cdot\nabla)T$ is neglected, since such parameter introduces high nonlinear difficulties. Therefore, the heat transfer equation with phase change can be ultimately outlined by

$$\rho(T)\,c(T)\,\frac{\partial T}{\partial t} = \frac{\partial}{\partial x}\left(k(T)\,\frac{\partial T}{\partial x}\right) + \frac{\partial}{\partial y}\left(k(T)\,\frac{\partial T}{\partial y}\right) + \dot{q}, \tag{3.3}$$

The latent heat source that represents the liquid-solid phase transformation, Eq. (3.3), is explicitly provided by

$$\dot{q} = \rho(T)\,L\frac{\partial f_{\mathrm{S}}}{\partial t}, \tag{3.4}$$

where L is the latent heat of fusion, f_{S} is the solid fraction function during the phase change (PIMENTA, 2014; BARCELLOS, 2011; SANTOS *et al.*, 2003), which is a function of temperature. Then, Eq. (3.4) can be properly represented as

$$\dot{q} = \rho(T)\,L\frac{\partial f_{\mathrm{S}}}{\partial T}\frac{\partial T}{\partial t}. \tag{3.5}$$

There are various approaches that express the solid fraction, f_S, in terms of the temperature (BEZERRA *et al.*, 2016). The one adopted by this work is the formulation employed in Anjos (2013) that uses the lever rule (GARCIA *et al.*, 2006),

$$f_S = \begin{cases} 0, & T > T_L \\ \dfrac{1}{1-k_\circ}\left(\dfrac{T_L - T}{T_F - T}\right), & T_S \leq T \leq T_L \text{ (Lever Rule)}, \\ 1, & T < T_S \end{cases} \tag{3.6}$$

where $k_\circ$ is the partition coefficient, T_L is the temperature of the liquid phase, T_S is the temperature of the solid phase, and T_F is the casting temperature.

The function in Eq. (3.6) assumes the thermodynamic equilibrium of the system, i.e. the chemical composition is uniform within each phase where complete diffusion of the solute is achieved. In addition, the partition coefficient is defined as the ratio of the solute concentration within the solid phase, C_S, and the solute concentration within the liquid, C_L, phase:

$$k_\circ = \frac{C_S}{C_L}. \tag{3.7}$$

Substituting Eq. (3.5) into (3.3), the heat conduction equation can be simplified with the introduction of the effective specific heat, $c'(T)$

$$\rho(T)\, c'(T) \frac{\partial T}{\partial t} = \frac{\partial}{\partial x}\left(k(T)\frac{\partial T}{\partial x}\right) + \frac{\partial}{\partial y}\left(k(T)\frac{\partial T}{\partial y}\right), \tag{3.8}$$

where c' is expressed by

$$c' = c - L\frac{\partial f_s}{\partial t}. \tag{3.9}$$

The density, specific heat as well as the thermal conductivity are assumed temperature dependent and they are written in terms of the solid fraction f_S as

$$\rho(T) = \rho_S f_S(T) + (1 - f_S(T))\,\rho_L, \tag{3.10}$$

$$c(T) = c_S f_S(T) + (1 - f_S(T))\, c_L, \tag{3.11}$$

$$k(T) = k_S f_S(T) + (1 - f_S(T))\, k_L, \tag{3.12}$$

where the subscripts S and L refer to solid and liquid phases, respectively.

The non-linear expression described in Eq. (3.8) does not take into consideration the convective effect of the liquid phase during the cooling stages (as previously mentioned). Then, to address this issue, the thermal conductivity for the liquid phase k_L is replaced by an effective

conductivity, k_{eff}, which is written as $k_{eff} = \vartheta k_{\mathrm{L}}$, where ϑ is a constant (SILVA, 2016). For the application proposed in this work, such constant is equal to 7, as it was adopted by Anjos *et al.* (2018). Others important thermophysical data used in the numerical procedure are given in Table 1.

Table 1 – Thermophysical properties of the AISI 1028 steel.

	Solid		Liquid
Conductivity (W/mK)	30		29
Specific heat (kJ/kgK)	642		600
Density (kg/m^3)	7850		7000
Phase temperature (°C)	1495		1509
Latent heat (kJ/kg)		277000	
T_{F} (°C)		1530	
k_0		0.2	

Additionally, it is assumed that the heat loss from the strand surface to the environment is given by

$$-k\nabla T \cdot \boldsymbol{n} = h\left(T_{\mathrm{w}} - T_{\mathrm{env}}\right), \tag{3.13}$$

where h represents the heat transfer coefficient at outer, inner and lateral sides (see Fig. 3); these coefficients were obtained by the numerical-experimental procedure delineated in (ANJOS *et al.*, 2018). These coefficients gather numerically the radiation and forced cooling effects. Moreover, T_{w} is the ingot's surface temperature and T_{env} is the temperature of the environment. At the symmetry axis, adiabatic condition is imposed (i.e., $h = 0$).

For the mold region, in particular, the heat transfer coefficient is evaluated along the casting direction, as it is pictured in Fig. 8. According to the study conducted by Anjos (2013), this film coefficient can be considered as an exponential function dependent of the cross section position $z(t)$,

$$h(z) = A + Be^{z(t)/C}, \tag{3.14}$$

where the constants parameters A, B, and C are calculated for each side face of the ingot's face and their values are shown in Table 2.

For the secondary cooling zone was implemented the empirical model of Bolle and Moureau (1946), which define the heat transfer coefficient as dependent of the water flow rate $\dot{m}$. Therefore, the expression for the sprays region is given by

$$h\left(\dot{m}\right) = 0.366\dot{m}^{0.556}, \tag{3.15}$$

Figure 8 – Orientation of the casting direction illustrated in the mold region.

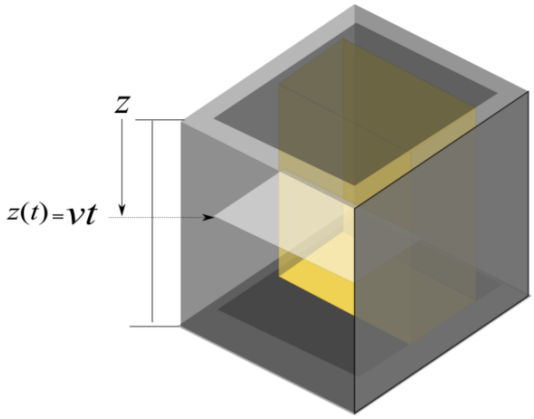

Table 2 – Constants of the heat transfer coefficient function.

Side	A [W/m^{2}K]	B [W/m^{2}K]	C [m]
Outer	1652.549	0.076	1012.3554
Inner	1382.753	0.11003	892.5904
Lateral	1323.349	0.10339	908.72076

Source: Anjos *et al.* (2018).

Finally, for the tertiary cooling stage is imposed a constant heat transfer coefficient throughout this cooling stage. The values assumed in the simulations are shown in Table 3.

Table 3 – Numerical heat transfer parameters applied in the secondary and tertiary cooling stages.

	secondary cooling			tertiary cooling
Velocity [m/min]	1st zone [l/s]	2nd zone [l/s]	3rd [l/s] zone	h[W/m^{2}K]
2.8	1.55	1.50	1.25	145
3.2	2.10	1.95	1.50	150

3.2 Thermodynamic background of the mechanical model

In this section an overall view of thermodynamics of continuum is presented. Herein we focus only on those forms of energy that are relevant to solid mechanics.

3.2.1 The laws of thermodynamics

3.2.1.1 First law of thermodynamics: Energy conservation

The first law of thermodynamics states that the energy cannot be created nor destroyed. However, it can be transferred from a location to another and converted to other forms of energy. In continuum mechanics, this statement is equivalent to say that the work done, W, by or upon the system and the heat, Q, transferred or received by the system are related to the change in the total energy of the system, ΔU. Therefore, considering an arbitrary domain with volume V and boundary ∂V, the rate of internal energy per time is given by (ASARO; LUBARDA, 2006)

$$\dot{U} = \frac{d}{dt}\int_V \rho e\, dV, \tag{3.16}$$

where e is the state variable called internal energy per unit of mass (or internal-energy density) (LUBLINER, 2008).

In order to present a fundamental concept of energies forms associated with the internal energy within the thermodynamic viewpoint, other important relations must be defined. That is for the kinetic energy, K, of a body that occupy a region V, one can express

$$K = \frac{1}{2}\int_V \rho v_i v_i\, dV, \tag{3.17}$$

where v_i is the velocity field. The heat flow transferred or received, $\dot{Q}$, by the body is represented through two terms: the heat flow generated within the volume V (by the external agencies) and the heat flow due to external agents via the boundary, ∂V, of the volume, V. The two aforementioned terms are given by

$$\dot{Q} = \int_V \rho R\, dV - \oint_{\partial V} q_i n_i\, dS, \tag{3.18}$$

where R is the volumetric density of the internal heat production, q_i is the heat flux vector, and n_i is the outward unit normal to ∂V. In addition, the external forces are related to the power acting on the body, $\dot{W}$, by assuming

$$\dot{W} = \int_V f_i v_i\, dV + \oint_{\partial V} T_i v_i\, dS, \tag{3.19}$$

where f_i and T_i are body and surface forces, respectively.

The above expression, Eq. (3.19), can be further rewritten in terms of the second order stress tensor, σ_{ij}, and body force vector b_i, as

$$\dot{W} = \int_V \left[\left(\frac{\partial \sigma_{ij}}{\partial x_j} + \rho b_i \right) v_i + \sigma_{ij} \frac{\partial v_i}{\partial x_j} \right] dV. \tag{3.20}$$

Therefore, the first law of thermodynamics is written as

$$\frac{d}{dt}(U+K) = \dot{Q} + \dot{W}, \tag{3.21}$$

or explicitly using the Gauss's theorem

$$\frac{d}{dt}\int_V \rho\left(e + \frac{1}{2}v_i v_i\right) dV = \int_V \left[\rho R - \frac{\partial q_i}{\partial x_j} + \left(\frac{\partial \sigma_{ij}}{\partial x_j} + \rho b_i\right) v_i + \sigma_{ij}\frac{\partial v_i}{\partial x_j}\right] dV. \tag{3.22}$$

Within the theory of infinitesimal deformations, the total strain deformation can be written as $\dot{\varepsilon}_{ij} = \frac{1}{2}\left(\frac{\partial v_i}{\partial x_j} + \frac{\partial v_j}{\partial x_i}\right)$. In addition, since $\sigma_{ij}\frac{\partial v_i}{\partial x_j} = \sigma_{ij}\dot{\varepsilon}_{ij}$ and $\dot{K} = \int_V \left(\frac{\partial \sigma_{ij}}{\partial x_j} + \rho b_i\right) v_i\, dV$, so that

$$\frac{d}{dt}\int_V \rho e\, dV = \int_V \rho R\, dV + \int_V \sigma_{ij}\dot{\varepsilon}_{ij}\, dV - \int_V \frac{\partial q_i}{\partial x_i} dV. \tag{3.23}$$

and one finally can obtain the local energy-balance equation as

$$\rho(\dot{e} - R) = \sigma_{ij}\dot{\varepsilon}_{ij} - \frac{\partial q_i}{\partial x_i}. \tag{3.24}$$

3.2.1.2 Second law of thermodynamics: Clausius–Duhem Inequality

The second law of thermodynamics states that the entropy (or disorder) of an isolated system always increases over time. This principle introduces in addition to the internal energy and rate of heating two new variables namely, temperature and entropy. In addition, the second law postulates, via Clausius equation, that the rate of entropy production is always greater than or equal to the rate of heating divided by the temperature

$$\frac{d}{dt}\int_V \rho s\, dV \geq \int_V \frac{R}{T} dV - \oint_{\partial V} \frac{q_i n_i}{T} dS, \tag{3.25}$$

where s is the entropy per unit of mass and T is the absolute temperature. Usually, left hand side of (3.25) is expressed in terms of the absolute entropy, $\bar{S}$, as function of the specific entropy s per unit of mass and the density as

$$\bar{S} = \int_V \rho s\, dV. \tag{3.26}$$

By applying the Gauss's theorem to the last term of the right hand side of (3.25), one can express

$$\frac{d}{dt}\int_V \rho s\, dV \geq \int_V \frac{R}{T} dV - \int_V \frac{\partial}{\partial x_i}\left(\frac{q_i}{T}\right) dV, \tag{3.27}$$

which can be further written as

$$\frac{d}{dt}(\rho s)+\frac{\partial}{\partial x_i}\left(\frac{q_i}{T}\right)-\frac{R}{T}\geq 0. \tag{3.28}$$

The fundamental inequality that contains the first and second laws is obtained by replacing R in Eq. (3.28) with Eq. (3.24)

$$\rho\left(T\frac{ds}{dt}-\frac{de}{dt}\right)+\sigma_{ij}\dot{\varepsilon}_{ij}-\frac{q_i}{T}\frac{\partial T}{\partial x_i}\geq 0. \tag{3.29}$$

The Clausius-Duhem inequality is subsequently obtained through the introduction of the specific free energy ψ, which is written as

$$\psi = e - Ts. \tag{3.30}$$

Differentiating the above equation in relation with time

$$\frac{d\psi}{dt}=\frac{de}{dt}-T\frac{ds}{dt}-s\frac{dT}{dt} \quad \text{or} \quad T\frac{ds}{dt}-\frac{de}{dt}=-\left(T\frac{d\psi}{dt}+s\frac{dT}{dt}\right), \tag{3.31}$$

when Eq. (3.31) is substituted in Eq. (3.29) it gives

$$\sigma_{ij}\dot{\varepsilon}_{ij}-\rho\left(\dot{\psi}+s\dot{T}\right)-\frac{q_i}{T}\frac{\partial T}{\partial x_i}\geq 0. \tag{3.32}$$

3.2.2 Thermodynamics in continuum mechanics

In continuum mechanics, the so-called local theory is commonly employed (SANTAOJA, 2004) to describe the deformation mechanism of body materials (metals, concretes, rocks, ices, among them). This assumption postulates that the thermodynamic state of a given material medium at a specific point and time depends only of certain number of state variables at that instant, which relies on the point considered (FACHINOTTI; CARDONA, 2003; LEMAITRE; CHABOCHE, 1994). Take Hooke's law for instance, the local theory states that the stress, σ, depends only on the value of deformation, ε, at a particular body point and time ($\sigma \propto \varepsilon$).

Within the thermomechanics framework there is a combination of thermodynamics and continuum mechanics. Such approach employs internal variables that induces a number of parameters which are beyond the controllable ones. These internal variables can be scalars or tensors of any order and usually outline the mechanical response of a solid material (SANTAOJA, 2004) and account for the internal state of matter, which are associated with density of dislocation, crystalline microstructure, composition of microcracks and cavities, etc (DUNNE; PETRINIC,

2005; LEMAITRE; CHABOCHE, 1994). According to Lemaitre and Chaboche (1994), the internal variables are, indeed, state variables and often are treated as observable ones.

Some state variables are the scalars: absolute temperature (controllable and observable), T, and isotropic hardening r_k (taken as a set of internal variables associated with the phenomenon of hardening); the second order tensors: total deformation, ε_{ij} (controllable and observable – assuming small strains assumption) and the internal variables elastic strain, ε^e_{ij}, and inelastic strain, ε^i_{ij}.

3.2.3 Thermodynamic potential

The state of a solid material is described by the specific Helmholtz free energy ψ, via Legendre transformation (WONG *et al.*, 2011; GURTIN *et al.*, 2010). The gradient of ψ represents *a priory* the constitutive state laws of an arbitrary body, as it will be shown in this section. Therefore, assuming:

$$\psi = \psi\left(\varepsilon_{ij}, \varepsilon^e_{ij}, \varepsilon^i_{ij}, T, r_k\right).$$

This definition is consistent with the decomposition of the strain tensor, where the total strain deformation is written in terms of elastic (reversible) and inelastic (irreversible) strains, as

$$\varepsilon_{ij} = \varepsilon^e_{ij} + \varepsilon^i_{ij}. \tag{3.33}$$

In the context of elastoplasticity and viscoplasticity theory, the elastic strain is presented only in their additive representation $\varepsilon^e_{ij} = \varepsilon_{ij} - \varepsilon^i_{ij}$ (a sum of reversible and irreversible process). Such property allows to redefine the specific Helmholtz free energy as follows

$$\psi = \psi\left(\varepsilon_{ij} - \varepsilon^i_{ij}, T, r_k\right) = \psi\left(\varepsilon^e_{ij}, T, r_k\right),$$

which gives

$$\frac{\partial \psi}{\partial \varepsilon^e_{ij}} = \frac{\partial \psi}{\partial \varepsilon_{ij}} = -\frac{\partial \psi}{\partial \varepsilon^i_{ij}}.$$

From the derivative of ψ with respect to time, one obtain,

$$\frac{d\psi}{dt} = \frac{\partial \psi}{\partial \varepsilon^e_{ij}}\dot{\varepsilon}^e_{ij} + \frac{\partial \psi}{\partial T}\dot{T} + \frac{\partial \psi}{\partial r_k}\dot{r}_k. \tag{3.34}$$

and now substituting the above expression in the Clausius-Duhem inequality, Eq. (3.32), one has (ASARO; LUBARDA, 2006)

$$\left(\sigma_{ij}-\rho\frac{\partial\psi}{\partial\varepsilon_{ij}^{e}}\right)\dot{\varepsilon}_{ij}^{e}+\sigma_{ij}\dot{\varepsilon}_{ij}^{i}-\rho\left(s+\frac{\partial\psi}{\partial T}\right)\dot{T}-\rho\frac{\partial\psi}{\partial r_k}\dot{r}_k-\frac{q_i}{T}\frac{\partial T}{\partial x_i}\geqslant 0, \tag{3.35}$$

where s the specific entropy per unit mass, ρ the density and q_i the heat flux vector.

In order to cancel off some terms in this inequality, Eq. (3.35), the classical hypothesis of thermodynamics (LEMAITRE; CHABOCHE, 1994; LUBLINER, 2008) can be employed. From this viewpoint, considering that only elastic deformation takes place at constant $\left(\dot{T}=0\right)$ and uniform $\left(\dfrac{\partial T}{\partial x_i}=0\right)$ temperature, it follows:

$$\sigma_{ij}-\rho\left(\frac{\partial\psi}{\partial\varepsilon_{ij}^{e}}\right)=0.$$

In addition, assuming the above expression and the thermal deformation in which $\varepsilon_{ij}^{i}=0$, $\dot{r}_k=0$, and $\dfrac{\partial T}{\partial x_i}=0$, one is able to obtain

$$s+\left(\frac{\partial\psi}{\partial T}\right)=0.$$

Therefore, in terms of the specific Helmholtz free energy, the state law equations can be derived using classical thermodynamics hypothesis as follows

$$\sigma_{ij}:=\rho\frac{\partial\psi}{\partial\varepsilon_{ij}^{e}}, \tag{3.36}$$

$$s:=-\frac{\partial\psi}{\partial T}, \tag{3.37}$$

$$A_k:=\rho\frac{\partial\psi}{\partial r_k}, \tag{3.38}$$

where A_k is the hardening thermodynamic force associated with the scalar internal variable r_k.

As can be seen in Eq. (3.32), the second law of thermodynamics introduces constraint over possible directions related to thermodynamic process through the inequality (ASARO; LUBARDA, 2006). Moreover, the introduction of the state function so-called entropy, s, accounts for the measurement of microstructural disorder of the system. This disorder is sensitive to interaction of the system with its neighborhood, which can take place by heat transfer; and also as a result of irreversible local rearrangements of microstructure generated as a consequence of deformation (dislocation movement) (HULL; BACON, 2001; ASARO; LUBARDA, 2006). Finally, the establishment of ψ as a scalar function which is concave with respect to T and convex with respect to the others variables satisfy the requirement imposed by the Clausius-Duhem inequality.

3.2.4 Thermoelasticity

For isotropic materials, under linear elastic theory, the thermodynamic potential ψ requires a quadratic representation in terms of the state variables, strain and temperature, which is also the invariant of the strain tensor (FACHINOTTI; CARDONA, 2003; ASARO; LUBARDA, 2006)

$$\psi := \psi^e = \frac{\lambda_T \varepsilon_{kk}^2 + 2\mu_T \varepsilon_{ij}\varepsilon_{ij} - 6\kappa_T \alpha_T (T - T_{\text{ref}})\delta_{ij}}{2\rho} - \frac{c_\varepsilon}{2T_{\text{ref}}}(T - T_{\text{ref}})^2, \tag{3.39}$$

where λ_T and μ_T are the isothermal Lamé elastic constants, $\kappa_T = \lambda_T + 2\mu_T/3$ is the isothermal bulk modulus, and the parameters α_T and c_ε are respectively, the coefficient of volumetric thermal expansion and specific heat at constant strain. These values are dependent of the reference temperature, T_{ref}.

From the definition introduced in Eq. (3.36) and (3.39), one can obtain the law of state so-called Duhamel-Neumann equation (DEMIRDŽIĆ; MUZAFERIJA, 1994):

$$\sigma_{ij} = 2\mu_T \varepsilon_{ij} + \lambda_T \varepsilon_{kk}\delta_{ij} - (2\mu_T + 3\lambda_T)\alpha_T (T - T_{\text{ref}})\delta_{ij}. \tag{3.40}$$

As it was stressed by Fachinotti and Cardona (2003) and Thomas *et al.* (1987), the product of $\alpha_T(T - T_{\text{ref}})$, in Eq. (3.40), implies small thermal variations, since it leads to $(T - T_{\text{ref}})/T_{\text{ref}} \ll 1$. The application of such assumption in continuous casting of steel is questionable, especially in the view of low carbon steel, where considerable changes in volume during the phase transition of $\delta \rightarrow \gamma$ takes place. Therefore, Thomas *et al.* (1987) suggests to replace the thermal expansion $\alpha_T(T - T_{\text{ref}})$ by the following Thermal Linear Expansion (TLE) (HUESPE *et al.*, 2000)

$$\beta_T(T, T_{\text{ref}}) = \int_{T_{\text{ref}}}^{T} \alpha(T')\, dT'. \tag{3.41}$$

Therefore, Eq. (3.40) is rewritten as

$$\sigma_{ij} = 2\mu_T \varepsilon_{ij} + \lambda_T \varepsilon_{kk}\delta_{ij} - (2\mu_T + 3\lambda_T)\beta_T \delta_{ij}. \tag{3.42}$$

3.2.5 Elastic domain and its validity

In most solid materials there is a region in the stress space limited by a boundary called yield surface, which can be expressed in terms of von Mises criterion by

$$f(\sigma_{ij}, A_i) = \sqrt{\frac{3}{2} S_{ij} S_{ij}} - \sigma_y, \tag{3.43}$$

where S_{ij} is the deviatoric part of the stress tensor, i.e.

$$S_{ij} = \sigma_{ij} - p\delta_{ij}, \tag{3.44}$$

since p accounts for the hydrostatic pressure and it is defined as

$$p = \frac{1}{3}\left(\sigma_{xx} + \sigma_{yy} + \sigma_{zz}\right), \tag{3.45}$$

Therefore, the deviatoric stress tensor can be represented as

$$S_{ij} = \begin{bmatrix} \sigma_{xx} & \sigma_{xy} & \sigma_{xz} \\ \sigma_{yx} & \sigma_{yy} & \sigma_{yz} \\ \sigma_{zx} & \sigma_{zy} & \sigma_{zz} \end{bmatrix} - \frac{1}{3}p \begin{bmatrix} 1 & 0 & 0 \\ 0 & 1 & 0 \\ 0 & 0 & 1 \end{bmatrix}. \tag{3.46}$$

The invariants of the deviatoric, S_{ij}, stress tensor J_1, J_2, and J_3 are used to determine the von Mises criterion, σ_v, such as (CRISFIELD *et al.*, 2012)

$$\begin{aligned} \sigma_v &= \sqrt{3J_2} \\ &= \sqrt{\frac{\left(\sigma_{xx} - \sigma_{yy}\right)^2 + \left(\sigma_{yy} - \sigma_{zz}\right)^2 + \left(\sigma_{zz} - \sigma_{xx}\right)^2 + 6\left(\sigma_{xy}^2 + \sigma_{yz}^2 + \sigma_{zx}^2\right)}{2}} \\ &= \sqrt{\frac{3}{2}S_{ij}S_{ij}}. \end{aligned}$$

Materials subjected to a load variation within the elastic domain experience a reversible deformation characterized by the movements of atoms, molecules or cells without breaking any original atomic bonds, resulting in zero dissipation. Moreover, the limit of the elastic region depends on the temperature as well as the previous load history. As the temperature increases, leading to irreversible deformations, the elastic domain diminishes until it becomes zero at the melting point. Differently, as the mechanical load increases, the elastic domain also increases through a phenomena known as hardening (LEMAITRE; CHABOCHE, 1994).

3.2.6 Dissipation potential

At the microscopic level, a tensile stress applied on a solid material that exceeds the elastic limit is characterized by breaking and restoration of atomic bonds, with consequent movement of atoms way beyond from their equilibrium positions. Such mechanism is responsible for heat dissipation, and originates irreversible deformation. This inelastic behavior is different for crystalline and amorphous structures. For crystalline microstructures, it occurs under a

process called slip, which is associated with motion of dislocation (HULL; BACON, 2001). On the other hand, for amorphous materials inelastic deformation is a result of viscous flow phenomena, where atoms/ions slide over each other without any preferential direction.

As it was made for the elastic description, the introduction of a scalar potential should be able to propose complementary constitutive equations that describe the evolution of the internal variables ε_{ij}^{i}, r_i, in case of inelastic deformation. Therefore, assuming the potential function $\varphi(\sigma_{ij},A_i,g_i)$, which is also called dissipation potential, one can obtain the following evolution laws through the normality rule (associated flow rule) (FACHINOTTI; CARDONA, 2003)

$$\dot{\varepsilon}_{ij}^{i} := \frac{\partial \varphi}{\partial \sigma_{ij}}, \tag{3.47}$$

$$-\dot{r}_k := \frac{\partial \varphi}{\partial A_k}, \tag{3.48}$$

$$-\frac{q_k}{T} := \frac{\partial \varphi}{\partial g_k}, \tag{3.49}$$

where $g_k = \dfrac{\partial T}{\partial x_k}$.

The condition of $\varphi(\sigma_{ij},A_i,g_i)$ begin convex function relative to σ_{ij}, r_i and g_i, implies $\varphi = 0$ at the origin, under the normality rule (NETO *et al.*, 2011). This result satisfies the Clausius-Duhem inequality, nonetheless it does not ensure necessarily condition for thermodynamic stability (FALLAH *et al.*, 2000; LEMAITRE; CHABOCHE, 1994).

The analysis employed in this work additionally admits the weak coupling of the thermal and mechanical behavior. Under such assumption, the temperature T is not used as a state variable, which implies that the heat flow, in Eq. (3.49), is also not taking into account. However, T is considered as a parameter, where the material properties, in the constitutive equation, depend upon. Finally, materials that behave according to the normality rule are known as standard materials (LEMAITRE; CHABOCHE, 1994; GURTIN *et al.*, 2010).

3.2.7 Plasticity

The plasticity theory make use of three fundamental concepts namely: yield criterion that defines the elastic limit, the flow rule that establish the relationship between stresses and strains when the material has become plastic, and the consistency condition which is employed to prevent the stress from exceeding the yield limit.

In particular, the necessary theory of plasticity used to describe plastic flow in metal

is relatively simple, since metals are in most cases incompressible, insensitive to the influence of hydrostatic pressure and, accurately follows the so-called associated flow rule. On the other hand, granular materials such as rocks, soils, concrete are somewhat more complex to be analysed, but the plasticity theory is still capable of modeling those materials (LUBLINER, 2008).

3.2.7.1 The yield surface

The elastic limit defined by Eq. (3.43) states that any value in which $f\left(\sigma_{ij},A_i\right) < 0$ characterizes the elastic region. Therefore, the yield function, $f\left(\sigma_{ij},A_i\right)$, specify a surface in stress space, which to its greatest extent contains six independent components, and A_i defines n specific material parameters. For simplicity, the yield surface is illustrated in the two-dimensional case in Fig. 9, where the boundary, $f = 0$, represents the set of maximal permissible stresses (KIM, 2014). This means that the state of stress is designated by a point either inside or over the yield surface.

Figure 9 – Two-dimensional representation of the yield surface.

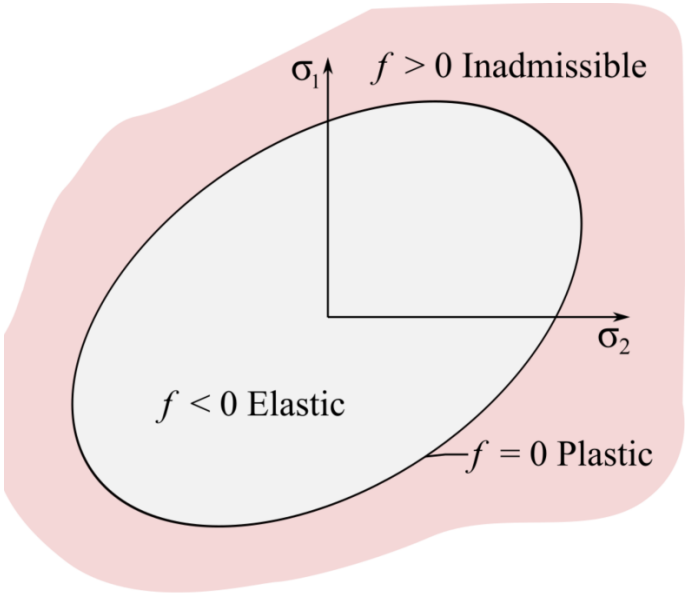

In particular cases such as perfect plasticity, the state of stress is altered by a redistribution of the different stress components so that the stress state can be imagined as point that slides along the yield surface. When hardening is included, the stress state point will remain over the boundary $f\left(\sigma_{ij},A_i\right) = 0$, which will be shifted following the hardening rules as the loading progresses. During the unloading, the stress point moves from the boundary of the yield surface to the inside, recovering its elastic properties.

3.2.7.2 Definition of the plastic deformation using von Mises criterion

The dissipation function φ within the viewpoint of rate-independent load behavior is positive, homogeneous of degree one and non-differentiable (LEMAITRE; CHABOCHE, 1994; FACHINOTTI; CARDONA, 2003). To address this issue the potential φ can be defined as an indicator function (or a characteristic function) of the criterion, $f(\sigma_{ij},A_k)$, introduced in Subsection 3.2.5, i.e.

$$\varphi = 0 \;\text{ if }\; f < 0 \;\;\rightarrow\;\; \dot{\varepsilon}^i = 0 \tag{3.50}$$

$$\varphi = +\infty \;\text{ if }\; f = 0 \;\;\rightarrow\;\; \dot{\varepsilon}^i \neq 0. \tag{3.51}$$

This is equivalent to write:

$$\dot{\varepsilon}^i_{ij} = \dot{\gamma}\frac{\partial F}{\partial \sigma_{ij}} \;\text{ if }\; \begin{cases} f = 0 \\ \dot{f} = 0, \end{cases} \tag{3.52}$$

where F is a potential function in which by the assumption of *associative* theory is equal to f and $\dot{\gamma}$ is a multiplier parameter that satisfies the *Kuhn-Tucker conditions* (or loading-unloading conditions):

$$\dot{\gamma} \geq 0, \quad f \leq 0, \quad \dot{\gamma} f = 0, \tag{3.53}$$

and the *consistency condition*

$$\dot{\gamma}\dot{f} = 0. \tag{3.54}$$

From the associative theory view point, the state laws in Eqs. (3.47) and (3.48) are rewritten as

$$\dot{\varepsilon}^i_{ij} := \dot{\gamma}\frac{\partial f}{\partial \sigma_{ij}}, \tag{3.55}$$

$$-\dot{r}_k := \dot{\gamma}\frac{\partial f}{\partial A_k}. \tag{3.56}$$

Therefore, the loading-unloading definition and the consistence condition defined above can be better organized by

I. **Elastic limit**. (Yield surface) represents the boundary region of the elastic domain, which does not depend on the plastic strain
$f\left(\sigma_{ij}\right) = 0.$

II. **Outside of elastic limit**. When a strain hardening material is under a inelastic load, the yield surface expands gradually followed by increasing of plastic strain and the elastic limit change
$f\left(\sigma_{ij},\varepsilon^{i}_{ij}\right)=0.$

III. **Loading**. During an inelastic loading $(f>0)$ the stress state is on the yield surface while the stress increment is conducted toward the outside of this surface, i.e.,
$d\sigma_{ij}\dfrac{\partial f}{\partial \sigma_{ij}}>0 \quad$ plastic loading process $\quad \dot{\gamma}>0.$

IV. **Unloading**. As for unloading, $f<0$, the material is in the elastic domain, and
$d\sigma_{ij}\dfrac{\partial f}{\partial \sigma_{ij}}<0 \quad$ elastic unloading $\quad \dot{\gamma}=0.$

V. **Neutral loading**. In this case, the stress state moves along the yield surface, i.e.,
$d\sigma_{ij}\dfrac{\partial f}{\partial \sigma_{ij}}=0 \quad$ neutral loading process $\quad \dot{\gamma}=0.$

VI. **Consistency condition**. The called *Prager consistency condition* is necessary in order to close the set of constitutive equations and also to eliminate the unknown parameter $d\lambda$ from the system of equations, so that
$df=\dfrac{\partial f}{\partial \sigma_{ij}}d\sigma_{ij}+\dfrac{\partial f}{\partial \varepsilon^{i}_{ij}}d\varepsilon^{i}_{ij}=0.$

Henceforth, in the context of associative plasticity assumption, this work follows the yield function $f(\sigma_{ij},A_i)$ as flow potential.

3.2.8 Isotropic elastoplastic hardening

Under the isotropic hypothesis and for purpose of this application, the hardening variable r_k is assumed to be the scalar r, which is an internal variable and it is also associated to the equivalent inelastic strain accumulated in the close time interval $[0,t]$ (FACHINOTTI; CARDONA, 2003), or in another way

$$r=\int_0^t \sqrt{\frac{2}{3}}||\varepsilon^{i}_{ij}(\tau)||\,d\tau \tag{3.57}$$

where $||\varepsilon^{i}_{ij}(\tau)||$ is the Euclidean norm of the tensor ε^{i}_{ij}. This internal variable r is used to describe the equivalent inelastic strain rate, when it is unified with the constitutive model.

As the plastic load occurs, the yield surface changes due to the accumulated inelastic deformation. The description of such phenomenon is due to the so called hardening rule. Therefore, considering that the material follows to the von Mises yield criterion, with the hardening behavior defined by *Ramberg-Osgood law* (LEMAITRE; CHABOCHE, 1994)

$$A_k(r):=A(r)=K_p r^{1/M} \tag{3.58}$$

where K_p is the plastic strength coefficient and M is hardening exponent. These are material properties dependent of temperature. According to Fachinotti and Cardona (2003), the isotropic exponent $1/M$ was accepted to be dependent over the *Zener-Hollomon* function

$$Z = \dot{\varepsilon} e^{\left[\frac{\bar{Q}}{R_g T}\right]}$$

where $\bar{Q}$ is the material activation energy and R_g the universal gas constant. The parameter Z is evaluated from data estimates of the strain rate $\dot{\varepsilon}$ and temperature. As stated by Fachinotti and Cardona (2003), these numerical information are not available on the literature.

From the consistency condition in Eq. (3.54) and Ramberg-Osgood, Eq. (3.58), the inelastic law is written as

$$\dot{\varepsilon}^i_{ij} = \frac{3}{2}\frac{M}{K_p}\left\langle \frac{\sigma_{eq} - \sigma_y}{K_p} \right\rangle^{M-1} \left\langle \dot{\sigma}_{eq} \right\rangle \frac{S_{ij}}{\sigma_{eq}}, \tag{3.59}$$

where $\sigma_{eq} = \sqrt{\frac{3}{2} S_{ij} S_{ij}}$ and $\langle \cdot \rangle$ is the Macauley brackets and it is used define the so-called ramp function

$$\langle x \rangle = \begin{cases} x, & x \geq 0 \\ 0, & x < 0. \end{cases}$$

This elastoplastic model, assuming linear isotropic hardening ($M = 1$), was proposed to describe the thermomechanical behavior of continuous casting of several steel carbon concentrations. Special attention is given for the works of Dvorkin and Canga (1990), that modeled 0.1 wt.% C carbon steel, and Huespe *et al.* (2000), that worked with 0.3 wt.% C carbon steel. These applications followed the well-known model proposed by Kelly *et al.* (1988). In particular, the elastoplastic study presented here act in accordance with analysis found in Huespe *et al.* (2000).

3.2.9 Viscoplasticity

The bench of continuum mechanics that describes the rate-dependent inelastic behavior of solids is called viscoplasticity theory. In this field, the flow of matter can be described by creep and, in opposition of rate-independent plasticity, it depends on time. In other words, the material response, during a plastic load is regarded as dependent of the load/unload rate. For materials that obeys the viscoplasticity hypotheses such as metals and alloys, it corresponds to process related to the movement of dislocation in grains (climb, deviation, polygonization) with superposed effects of intercrystalline gliding (LEMAITRE; CHABOCHE, 1994; HULL;

BACON, 2001). These effects undertake in general when the material temperature is greater than around one third of the absolute melting temperature.

From experimental observations, the comportment of the materials is commonly load rate-dependent. However, if the load timescale is within a range where the viscoplastic effect can be neglected, the plasticity theory is able to provide an accurate description of the material's mechanic behavior (LEMAITRE; CHABOCHE, 1994; LUBLINER, 2008; NETO *et al.*, 2011). Under certain degree, the rate independent plasticity is proven to be a limit case of the viscoplasticity model.

Viscoplastic models are widely used to numerically investigate the thermomechanical nature throughout the solidification process as the strand exits the casting machine. Nonetheless, in the literature, there are no standard viscoplastic model fully suitable for such numerical application, ab this reason is mostly due to the lack of experimental data (HUESPE *et al.*, 2000). In this work, it is used the *Odqvist's law*, since this model is simple to be numerically implemented and provides low computational cost. The Odqvist's law assumes an elastic domain whose length is characterized by the initial stress σ_y and it is consistent with the dissipation potential φ

$$\varphi = \frac{K_\varepsilon}{N_\varepsilon + 1} \left\langle \frac{\sigma_{eq} - \sigma_y}{K_\varepsilon} \right\rangle^{N_\varepsilon + 1}, \tag{3.60}$$

this representation can define the inelastic plasticity tensor via the gradient of the potential $\nabla_{\sigma_{ij}} \varphi$, i.e.

$$\dot{\varepsilon}^i_{ij} = \nabla_{\sigma_{ij}} \varphi = \sqrt{\frac{3}{2}} \left\langle \frac{\sigma_{eq} - \sigma_y}{K_\varepsilon} \right\rangle^{N_\varepsilon} \frac{S_{ij}}{||S_{ij}||}, \tag{3.61}$$

Where N_ε is a non-dimensional rate-sensitivity parameter and K_ε is the viscosity-like parameter of the material.

Numerical models using the proposed law can be found in the works of Williams *et al.* (1979), Lewis *et al.* (1984), and Inoue (1987) that adopted the simplification $N_\varepsilon = 1$ in Eq. (3.60). Herein is assumed the Odqvist's law and the data fitted from the model proposed by Bellet and Heinrich (2004).

3.3 Constitutive elasto-plastic-viscoplastic relationships

In this subsection is discussed the physical models which describe the behavior of solids over small deformation.

3.3.1 Strain tensor decomposition

The plasticity and viscoplasticity theories are able to characterize the mechanical behavior of materials beyond the boundaries of the elastic limit (NETO *et al.*, 2011). Basically, these concepts can determine whether a given stress state falls within the elastic or inelastic domain by means of the yield criterion function and present mechanisms to preform correction of the stress state in case of inelastic load. Additionally, the assumption of von Mises yield criterion with isotropic hardening law, in situation of plasticity, is considered a very efficient procedure in the analysis of stress state of metallic materials.

From the viewpoint of the infinitesimal strain theory, which also assumes small displacements and rotation, the total deformation rate tensor $\dot{\varepsilon}_{ij}$ can be decomposed into strain rate tensors containing elastic $\dot{\varepsilon}^e_{ij}$, inelastic $\dot{\varepsilon}^i_{ij}$, and thermal $\dot{\varepsilon}^{th}_{ij}$ (ZHU, 1996),

$$\dot{\varepsilon}_{ij} = \dot{\varepsilon}^e_{ij} + \dot{\varepsilon}^{th}_{ij} + \dot{\varepsilon}^i_{ij}. \tag{3.62}$$

In the above expression, the inelastic strain rate $\dot{\varepsilon}^i_{ij}$ is associated with both time-independent plasticity and time-dependent creep.

3.3.2 Stress-Strain tensor relationship

The stress tensor can be expressed, in the context of linear elastic assumption, from Eq. (3.39) by means of the generalized Hooke's law,

$$\sigma_{ij} = \rho \frac{\partial \psi}{\partial \varepsilon_{ij}}, \tag{3.63}$$

which is commonly seen as

$$\sigma_{ij} = D^e_{ijkl} \varepsilon^e_{kl}, \tag{3.64}$$

where σ_{ij} is known as the second rank Cauchy stress tensor, D^e_{ijkl} is the fourth rank isotropic elastic modulus tensor, and ε^e_{kl} is the second rank elastic strain increment tensor. In terms of Lamé's constants, λ_T and μ_T, the elastic modulus can be written as

$$D^e_{ijkl} = \lambda_T \delta_{ij} \delta_{kl} + \mu_T \left(\delta_{ik} \delta_{jl} + \delta_{jk} \delta_{il} \right). \tag{3.65}$$

The Lamé's parameters are related to Young's modulus E and Poisson's ratio ν through the following expression:

$$\lambda_T = \frac{\nu E}{(1+\nu)(1-2\nu)} \quad \text{and} \quad \mu_T = \frac{E}{2(1+\nu)}. \tag{3.66}$$

As it was mentioned in the previous section, these material parameters are thermal dependent. Therefore, the stress tensor rate is expressed, including the inelastic parameters, (via manipulation of Eq. (3.62) and D^{ep}_{ijkl}) as follows:

$$\dot{\sigma}_{ij} = D^{ep}_{ijkl}(\dot{\varepsilon}_{kl} - \dot{\varepsilon}^{th}_{kl} - \dot{\varepsilon}^{i}_{kl}) + \dot{T}\frac{\partial D^{ep}_{ijkl}}{\partial T}(\varepsilon_{kl} - \varepsilon^{th}_{kl} - \varepsilon^{i}_{kl}), \tag{3.67}$$

where D^{ep}_{ijkl} is the elastic-plastic material tensor, i.e. in the elastic scenario $D^{ep}_{ijkl} = D^{e}_{ijkl}$ and in case of inelastic load, $D^{ep}_{ijkl} = D^{p}_{ijkl}$. As one is able to notice, the second term of the right hand side of the above equation introduces an additional contribution to the elastic-plastic stress tensor rate due to temperature variation. In solidification models, this term is often neglected (CHAUDHURI *et al.*, 2010; HUESPE *et al.*, 2000; ZHU, 1996). Therefore, the representation that describes the stress state with mechanical parameters thermal dependent is given by

$$\dot{\sigma}_{ij} = D^{ep}_{ijkl}(\dot{\varepsilon}_{kl} - \dot{\varepsilon}^{th}_{kl} - \dot{\varepsilon}^{i}_{kl}). \tag{3.68}$$

The infinitesimal strain tensor is written in terms of the displacements as:

$$\varepsilon_{ij} = \frac{1}{2}\left(\frac{\partial u_i}{\partial x_j} + \frac{\partial u_j}{\partial x_i}\right), \tag{3.69}$$

where u_i is the displacement vector.

In problems involving temperature variation, the thermal deformation produced is expressed as

$$\varepsilon^{th}_{ij} = \beta_{ij}\left(T - T_{ref}\right). \tag{3.70}$$

where β_{ij} is the thermal expansion tensor of the material, T is the local temperature and T_{ref} is the reference temperature. From the assumption of isotropy, the thermal expansion tensor can be written as

$$\beta_{ij} = \alpha\delta_{ij}, \tag{3.71}$$

where α is the linear expansion coefficient.

The thermal strain deformation defined in Eq. (3.70) was employed in the benchmark tests presented in Chapter 5. However, in the continuous casting simulations, the thermal strain is better described by the Eq. (3.41), i.e.

$$\varepsilon^{th}_{ij} = \beta_T(T, T_{\text{ref}})\,\delta_{ij}. \tag{3.72}$$

This expression includes experimental observations, from melting to the room temperature, which was first suggested by Jablonka *et al.* (1991). Such physical aspect is caused by both temperature differences and phase changes (ZHU, 1996). Moreover, the thermal linear expansion function (TLE), $\beta_T(T, T_{\text{ref}})$, is obtained from solid-phase density measurements by Harste *et al.* (1988), as well as liquid density measurements which was given by Jimbo and Cramb (1993). The TLE is, therefore, written as (LI; THOMAS, 2004)

$$\beta_{\text{phase}} = \sqrt[3]{\frac{\rho(T_{\text{ref}})}{\rho(T)}} - 1, \tag{3.73}$$

where, for the multiphase region, the effective density is given in terms of the different phases $(\alpha, \gamma, \delta, l)$ fractions, $\bar{f}$, and phase density, as

$$\rho\left(\text{kg/m}^3\right) = \rho_\alpha \bar{f}_\alpha + \rho_\gamma \bar{f}_\gamma + \rho_\delta \bar{f}_\delta + \rho_l \bar{f}_l, \tag{3.74}$$

where each individual phase is represented as

$$\begin{aligned}
\rho_\alpha &= 7881 - 0.324T(^\circ\text{C}) - 3\times 10^{-5} T^2(^\circ\text{C}) \\
\rho_\gamma &= \frac{100\,(8106 - 0.51T(^\circ\text{C}))}{(100 - \%\text{C})\,(1 + 0.008\%\text{C})^3} \\
\rho_\delta &= \frac{100\,(8011 - 0.47T(^\circ\text{C}))}{(100 - \%\text{C})\,(1 + 0.013\%\text{C})^3} \\
\rho_l &= 7100 - 73\%\text{C} - (0.8 - 0.09\%\text{C})\,(T(^\circ\text{C}) - 1550)\,.
\end{aligned} \tag{3.75}$$

Numerically, the thermal strain rate is evaluated within time interval $[t, t+\Delta t]$. Therefore, assuming the backward-difference scheme

$$\dot{\varepsilon}_{ij}^{th} \approx \frac{\beta_{T(t+\Delta t)} - \beta_{T(t)}}{\Delta t}\delta_{ij}, \tag{3.76}$$

where

From the associated plasticity flow, in case of rate independent plasticity, the inelastic deformation is writing by the Prandtl-Reuss relations as

$$\varepsilon_{ij}^{i} = \sqrt{\frac{3}{2}}\bar{\varepsilon} N_{ij}, \tag{3.77}$$

where $\bar{\varepsilon}$ is an internal variable and N_{ij} is the unit direction tensor of the inelastic strain, which is expressed by

$$N_{ij} = \sqrt{\frac{3}{2}}\frac{S_{ij}}{|S_{ij}|}. \tag{3.78}$$

And the inelastic strain rate form is given by

$$\dot{\varepsilon}_{ij}^{i} = \sqrt{\frac{3}{2}}\dot{\bar{\varepsilon}}\, N_{ij}, \tag{3.79}$$

At each individual material point, the implicit time integration of the stress-strain rate relationship, Eq. (3.68), is expressed in terms of the known strain, in the previous time step n, and the unknown strain tensor in the actual time $n+1$, as follows

$$\Delta\sigma_{ij}^{n+1} = D_{ijkl}^{ep,n+1}\left[\varepsilon_{kl}^{n+1} - \varepsilon_{kl}^{n} - \varepsilon_{kl}^{n+1,th} + \varepsilon_{kl}^{n,th} - \varepsilon_{kl}^{n+1,i} + \varepsilon_{kl}^{n,i}\right]. \tag{3.80}$$

The total deformation is based upon the calculated incremental displacement field given via the solution of the equilibrium equations. For the inelastic deformation rate, in the first time step is assumed to be zero and, in case of plastic load, a numerical procedure described in Subsection 4.5.2 is employed to evaluate the actual inelastic step. A bi-dimensional linear description is presented in Appendix A.

3.4 Conservation of linear momentum

The fundamental equation to describe motion and deformation of continuum in solids and fluids is the Euler equation through the linear momentum. This analysis can be made using the Eulerian approach, where the balance of momentum is made on a fixed control volume in space; or via the Lagrangian framework, since the variation in momentum is tracked in a particularized volume of the continuum that movies through space (VOLLER, 2009). From the EbFVM view point, the most convenient scenario is the one outlined by the Eulerian approach. Therefore, using Newton's second law of motion, in the Eulerian frame of reference, the conservation of momentum is written for a fixed control volume, V, as

$$\frac{d}{dt}\int_V \rho\mathbf{v}\,dV = \int_V \rho\mathbf{b}\,dV + \oint_S \mathbf{t}\,dS - \oint_S (\mathbf{v}\cdot\mathbf{n})\rho\mathbf{v}\,dS, \tag{3.81}$$

where ρ is the density, $\mathbf{v}$ is material velocity (from a fixed frame of reference), $\mathbf{b}$ is body force vector and $\mathbf{t}$ is the traction vector, which gather the fraction forces that act tangential and normal on the boundary surface S of the volume V. In addition, the left hand side of (3.81) represents rate of change in the linear momentum of the fixed volume V, which is equalized by the body force in volume V, the traction on the surface S and the net of linear momentum that flows into V through the boundary S.

The traction vector is often expressed in terms of the second order Cauchy stress tensor σ_{ij} and the unit outward normal $\mathbf{n}$ vector, as

$$t_i = \sigma_{ij} n_j, \tag{3.82}$$

and the expression in Eq. (3.81) can be rewriting in index notation as follows:

$$\frac{d}{dt}\int_V \rho v_i \, dV = \int_V \rho b_i \, dV + \oint_S \sigma_{ij} n_j \, dS - \oint_S (v_j n_j) \rho v_i \, dS. \tag{3.83}$$

The stress state of an arbitrary body, under infinitesimal strain theory, is investigated during a (thermomechanical) load by restricting rotation and translation of the material body. For the sake of this application, body force vector is neglected. As a result of these simplifications, the linear momentum is presented by

$$\oint_V \sigma_{ij} n_j \, dS = 0. \tag{3.84}$$

From the above equation, Eq. (3.84), important analysis can be performed in the context of structural field, which contemplates plasticity and viscoplasticity material behavior. However, the understanding of such aspects is possible only via its numerical solution (see discussion in Section 1.4). A complete description of this numerical procedure is given in Section 4.4.

4 DISCRETIZATION PROCEDURE

4.1 General aspects of the EbFVM

Since the introduction of the first digital computer, in the 20th century, a wide number of discretization techniques have been proposed for the solution of partial differential equations. However, three methods have received more attention i.e, Finite Element Method (FEM), Finite Difference Method (FDM), and Finite Volume Method (FVM) (VOLLER, 2009). During this period, FEM established itself as the standard approach in solid mechanics analysis (ZIENKIEWICZ; TAYLOR, 1991; DEMIRDŽIĆ; MARTINOVIĆ, 1993). On the other hand, FDM and FVM have been established as very efficient procedures in Computational Fluid Dynamics (CFD) (MALISKA, 2004; TAYLOR *et al.*, 2003; TAYLOR *et al.*, 1995).

In the last few decades, FEM has been improved and applied in areas, such as electromagnetism and fluid dynamics (ZIENKIEWICK; TAYLOR, 1989; VOLLER, 2009). FVM and FDM have also been enhanced and nowadays they have been successfully applied to a significantly number of physical problems, as for instance, acoustics (BILBAO; HAMILTON, 2017), solid-fluid iteration (SLONE *et al.*, 2003), and radiative transfer phenomenon (ZHANG *et al.*, 2017). A key issue that differentiate FVM from FEM and FDM is the ability of the first aforementioned method to guarantee local conservation of the physical properties being evaluated (FERNANDES *et al.*, 2013; MALISKA, 2004; PATANKAR, 1980; BALIGA; PATANKAR, 1980). Such behavior is a desired property in any numerical method (FILIPPINI *et al.*, 2014; TAYLOR *et al.*, 2003; WHEEL, 1996), see for instance the Hybrid Finite Element Method (WOODWARD; DAWSON, 2000; FORSYTH; KROPINSKI, 1997; BAUSE; KNABNER, 2004; SRIVASTAVA; YEH, 1992).

FVM is divided into two main approaches (VOLLER, 2009; TAYLOR *et al.*, 2003), which are cell-centered (DEMIRDŽIĆ; MARTINOVIĆ, 1993; WHEEL, 1996) and cell-vertex (TAYLOR *et al.*, 1995; JASAK; WELLER, 2000; FALLAH *et al.*, 2000). The first procedure is an important variant of FDM, where each element or cell of the grid is a Contol Volume (CV) and the independent variables are evaluated at geometric center of each element. This approach has been largely used in the context of structured grids, such as Cartesian (MOCZO *et al.*, 2007), cylindrical (VERZICCO; ORLANDI, 1996), and boundary-fitted coordinates (RYSKIN; LEAL, 1984). Despite boundary-fitted coordinates is more suitable to represent complex geometries than the others just mentioned, it still has drawbacks to model certain complex geometry

shapes (TAYLOR *et al.*, 2003). This issue was overcome with the introduction of unstructured meshes, see for instance (SULIMAN *et al.*, 2014). The second procedure borrows from FEM the idea of elements and shapes functions (FERNANDES *et al.*, 2017; FERNANDES, 2014; MARCONDES; SEPEHRNOORI, 2010; VOLLER, 2009). In the cell-vertex approach, the CV is constructed around each node of the grid, Fig. 10, (VOLLER, 2009; TAYLOR *et al.*, 2003). This methodology has advantages over the cell-centered approach, since it is well suitable for problems where the unknowns have to be determined at the boundary region (TAYLOR *et al.*, 2003) and it also can be easily implemented for either structured and unstructured grids.

Figure 10 – EbFVM discretization. Element, sub-control volumes and control volumes.

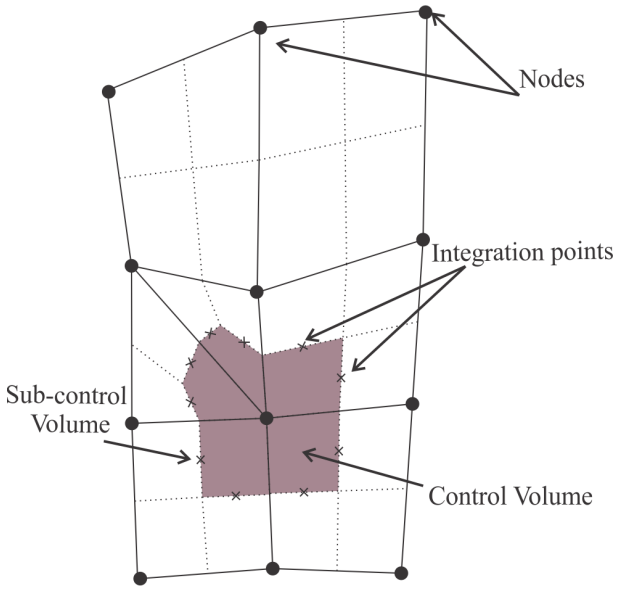

The FVM, in the context of the unstructured meshes, was initially called Control Volume based Finite Element Method (CVFEM) (VOLLER, 2009; BALIGA; PATANKAR, 1980). According to Maliska (2004), the CVFEM nomination gives a wrong idea that this method uses FEM based on control volumes. He suggested to replace the CVFEM terminology by EbFVM, since in this methodology still has a conservative approach at the CV level that only borrows from FEM the idea of elements and shape functions (MARCONDES; SEPEHRNOORI, 2010). Henceforward, such nomenclature is adopted in this work.

The pioneer application of the EbFVM was devoted to analyze the numerical solution of Poisson's Equation in the field of electromagnetism using triangular elements by Winslow (1966). Subsequently, EbFVM was applied to heat transfer and fluid flow problems using triangular elements by Baliga and Patankar (1980) and quadrilateral elements by Schneider

and Zedan (1983). To the best the author's knowledge, the first application of EbFVM in Computational Solid Mechanical (CSM) was proposed by Fryer *et al.* (1991) for solving elastic stress-strain equations. Further applications in this field was followed by Bailey and Cross (1995), to analyze the three-dimensional linear-elastic problems. Later on the EbFVM was extended to nonlinear for two- and three-dimensional viscoplaslasticity by Taylor *et al.* (1995) and Taylor *et al.* (2003), respectively, and by Fallah *et al.* (2000) to analysis nonlinear geometrical problems.

4.2 EbFVM discretization procedure

As mentioned previously, the EbFVM guideline uses from FEM the idea of elements and shape functions. Nevertheless, in the EbFVM context, the elements are further subdivided into sub-control volumes, where the number of divisions depend upon the number of nodes of each element. Take for instance the bi-linear quadrilateral elements, as pictured in Fig. 11, in which all individual element has four sub-control volumes. Additionally, the CV is formed by every sub-control volume that shares the same node, giving rise to a cell-vertex formulation.

Figure 11 – EbFVM discretization for a bi-linear quadrilateral elements.

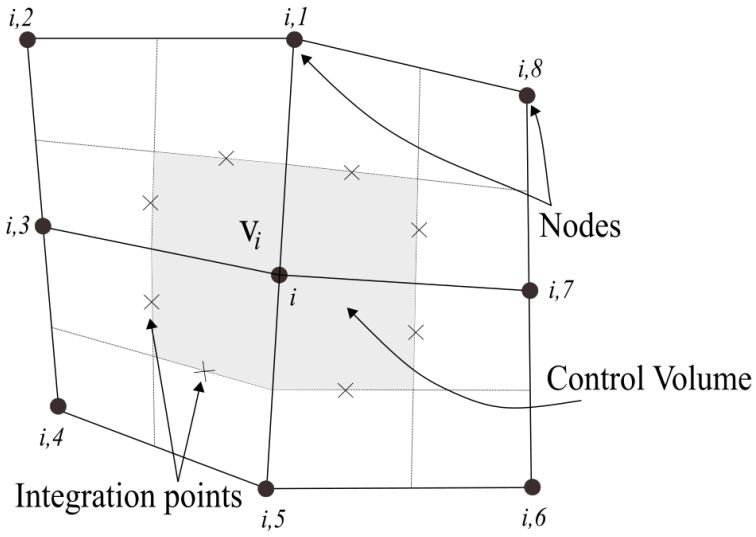

In simple terms, the shape functions are used to evaluate the unknowns' variables in the physical plane by mapping those terms in the computational one, as can be depicted in Fig. 12. Assuming $\phi(x,y)$, for instance, as the unknown variable, it can be evaluated at any point within an arbitrary element as

$$\phi(x,y) \approx \sum_{i=1}^{4} N_i \phi_i. \tag{4.1}$$

where the shape functions, N_i, for a bi-linear quadrilateral element, are given by (CRISFIELD *et al.*, 2012):

$$N_1(\xi,\eta) = \frac{1}{4}(1-\xi-\eta+\xi\eta), \tag{4.2}$$

$$N_2(\xi,\eta) = \frac{1}{4}(1-\xi+\eta-\xi\eta), \tag{4.3}$$

$$N_3(\xi,\eta) = \frac{1}{4}(1+\xi+\eta+\xi\eta), \tag{4.4}$$

$$N_4(\xi,\eta) = \frac{1}{4}(1+\xi-\eta-\xi\eta), \tag{4.5}$$

Figure 12 – Bi-linear Quadrilateral element. a) physical plane, and b) computational plane.

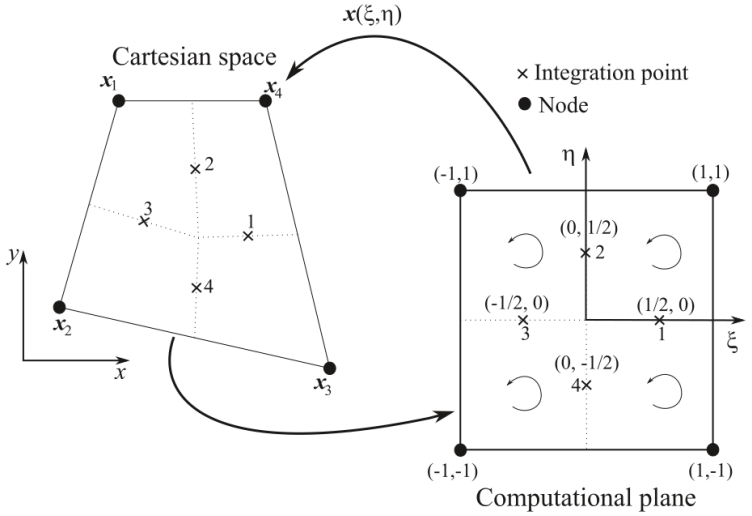

In order to evaluate numerically the derivatives of the unknowns, it is convenient the introduction of the relations below:

$$\frac{\partial N_i}{\partial x} = \frac{1}{|J|}\left(\frac{\partial y}{\partial \eta}\frac{\partial N_i}{\partial \xi} - \frac{\partial y}{\partial \xi}\frac{\partial N_i}{\partial \eta}\right), \tag{4.6}$$

$$\frac{\partial N_i}{\partial y} = \frac{1}{|J|}\left(\frac{\partial x}{\partial \xi}\frac{\partial N_i}{\partial \eta} - \frac{\partial x}{\partial \eta}\frac{\partial N_i}{\partial \xi}\right), \tag{4.7}$$

where $|J|$ is the Jacobian of the transformation, which is given by

$$|J| = \left(\frac{\partial x}{\partial \xi}\frac{\partial y}{\partial \eta} - \frac{\partial x}{\partial \eta}\frac{\partial y}{\partial \xi}\right). \tag{4.8}$$

The integration process that is presented next occurs along the interfaces of each sub-control volume. Additionally, the areas of each interface, in x- and y-directions, following a

counterclockwise orientation, are explicitly given by

$$n_x \Delta s = h \sum_{i=1}^{4} \left(\frac{\partial N_i}{\partial \xi} d\xi + \frac{\partial N_i}{\partial \eta} d\eta \right) y_i, \tag{4.9}$$

$$n_y \Delta s = -h \sum_{i=1}^{4} \left(\frac{\partial N_i}{\partial \xi} d\xi + \frac{\partial N_i}{\partial \eta} d\eta \right) x_i, \tag{4.10}$$

where h is the thickness of the domain.

For more information about EbFVM integration procedure, the reader is invited to see for instance (VOLLER, 2009; MALISKA, 2004).

4.3 EbFVM integration of heat conduction equation

The EbFVM discretization method uses the integration procedure as described in Section 4.2. For quadrilaterals elements, the integration of Eq. (3.8) in space and time is performed at each individual sub-control volume V_i, which is pictured in Fig. 11. Therefore, using the Gauss theorem, one obtain

$$\int \int_{V_i} \frac{\partial}{\partial t} \left(\rho c' T \right) dV dt = \int \oint_{\partial S_i} [\boldsymbol{n}] \left[k \nabla T \right] dS dt. \tag{4.11}$$

The integration procedure over the volume V_i adopted by EbFVM is based on the mid-point rule $\int_{\mathrm{V}_i} \phi \, d\mathrm{V} \approx \phi \, \Delta \mathrm{V}_i$. Therefore, the left-hand side of Eq. (4.11) is numerically written in the form

$$\int \int_{V_i} \frac{\partial}{\partial t} \left(\rho c' T \right) dV \approx \left(\rho c' T \Big|^{n+1} - \rho c' T \Big|^{n} \right) \Delta V dt. \tag{4.12}$$

As for the surface integral in Eq. (4.11), it is expressed in terms a sum of integrals over the CV interfaces and each of one of these integrals are likewise evaluated by the application of the mind-point rule (JASAK; WELLER, 2000), i.e.,

$$\int \oint_{\partial S_i} [\boldsymbol{n}] \left[k \nabla T \right] dS dt \approx \Delta t \sum_{j=1}^{nip} \left(\kappa \sum_{i=1}^{nve} \nabla N_i \cdot \Delta \vec{S} \Big|^{n+\theta} \right)_j T_i^{n+\theta}, \tag{4.13}$$

where nip is the number of integration points and nve is the number of vertex associated with the sub-control volume.

From the combination of Eqs. (4.12) and (4.13), the linearized set of equations can finally be written as

$$\left(\rho c' T \Big|^{n+1} - \rho c' T \Big|^{n} \right) \Delta V = \Delta t A^{\mathrm{cv}, n+\theta} \left(\theta T^{n+1} + (1-\theta) T^{n} \right), \tag{4.14}$$

where $\theta \in [0,1]$ represents the Finite Difference Method scheme for time interpolation and A^{cv} is the coefficient matrix, which is expressed by

$$A^{\mathrm{cv},n+\theta} = \sum_{j=1}^{ip} \left(k\left(T^{n+\theta}\right) \sum_{i=1}^{nve} [\boldsymbol{n}] \left[\nabla N_i \Delta S\right] \right)_j , \tag{4.15}$$

For this work, it is adopted an explicit interpolation approach, $\theta = 0$. In this methodology, the numerical solution at the actual time-level is obtained using the values from the previous time-level. Nevertheless, to ensure stability, the time step must be carefully chosen to ensure positive coefficients.

4.4 EbFVM integration of momentum equation

For quasi-static load processes, the momentum equation introduced in Eq. (3.84) can be reduced to the form

$$F_{i,\mathrm{ext}} - F_{i,\mathrm{int}} = 0, \tag{4.16}$$

where $F_{i,\mathrm{ext}}$ and $F_{i,\mathrm{int}}$ are the internal and external force vector, respectively. The above expression is equivalent to the momentum equation (3.84) of an arbitrary solid, with a volume V and boundary ∂V, under translation and rotation equilibrium (NETO *et al.*, 2011), i.e.

$$F_{i,\mathrm{int}} - F_{i,\mathrm{ext}} = \oint_{\partial V} \sigma_{ij} n_j \, dS. \tag{4.17}$$

By implicitly decomposing the vector of unknown stress components at time $n+1$, which is denoted as σ_{ij}^{n+1}, into:

$$\sigma_{ij}^{n+1} = \sigma_{ij}^{n} + \Delta\sigma_{ij}^{n+1}, \tag{4.18}$$

and substituting this decomposition into Eq. (4.16), it results

$$F_{i,\mathrm{ext}}^{n+1} - \oint_{\partial V} \sigma_{ij}^{n} n_j \, dS - \oint_{\partial V} \Delta\sigma_{ij}^{n+1} n_j \, dS = 0. \tag{4.19}$$

From the numerical viewpoint, Eq. (4.19) can be rewritten considering the form presented in Eq. (3.80), for each sub-control volume of individual element (*ne*) of the finite element domain

$$\sum_{e=1}^{ne} \oint_{\partial V^{(e)}} \Delta\sigma_{ij}^{n+1} n_j \, dS = \sum_{e=1}^{ne} \oint_{\partial V^{(e)}} D_{ijkl}^{ep,n+1} \left[\Delta\varepsilon_{kl}^{n+1} - \Delta\varepsilon_{kl}^{n+1,th} - \Delta\varepsilon_{kl}^{n+1,i} \right] n_j \, dS. \tag{4.20}$$

The expression above can be rearranged in order to assume

$$\sum_{e=1}^{ne} \oint_{\partial V^{(e)}} D_{ijkl}^{ep,n+1} \Delta\varepsilon_{kl}^{n+1} n_j \, dS = \Delta F_{i,\text{ext}}^{n+1} - \Delta F_{i,\text{int}}^{n+1} - \Delta F_{i,\text{th}}^{n+1}, \tag{4.21}$$

where $\Delta F_{i,\text{th}}^{n+1}$ is the force due to the thermal variation. A more detailed discretization procedure is presented in Appendix B.

By taking the matrix notation for the strain tensor $\left[\Delta\varepsilon_{ij}\right] = \left[L_{ij}\sum_{p=1}^{nve} N_p\right]\left[\Delta u_{j(p)}\right]$, the left hand side of Eq. (4.21) can rewritten as

$$\sum_{e=1}^{ne} A_{ij}^{e,n+1} \Delta u_j^{n+1} = \Delta F_{i,\text{ext}}^{n+1} - \Delta F_{i,\text{int}}^{n+1} + \Delta F_{i,\text{th}}^{n+1}, \tag{4.22}$$

where A_{ij}^{e} is the so-called stiffness matrix for an arbitrary sub-control volume. Once gathering the contributions of each sub-control volume, the stiffness matrix of the control volume, A_{ij}, is formed. Such expression is evaluated at the integration points k and globally it is given in terms of the number of the nodes (*nve*) associated with the control volume. Therefore, taking any control volume, one is able to explicitly express

$$A_{ij}^{n+1} = \sum_{k=1}^{ip} \int_{\partial V_k} n_j D_{ijlm}^{ep,n+1} \left[\sum_{p=1}^{nve} L_{lm} N_p\right]_k dS_k, \tag{4.23}$$

where n is the outward unit vector and it is convenient defined as

$$n_j = \begin{bmatrix} n_x & 0 & n_y \\ 0 & n_y & n_x \end{bmatrix}. \tag{4.24}$$

In the context of the Voigt's notation, the differential operator L_{ij} is given by

$$L_{ij} = \begin{bmatrix} \frac{\partial}{\partial x} & 0 \\ 0 & \frac{\partial}{\partial y} \\ \frac{\partial}{\partial y} & \frac{\partial}{\partial x} \end{bmatrix}, \tag{4.25}$$

The vector force that takes into account the thermal variation at each vertex is expressed as follows:

$$F_{i,\text{th}}^{n+1} = \sum_{k=1}^{ip} \int_{\partial V_k} n_j D_{ijlm}^{ep,n+1} \varepsilon_{lm}^{n+1,th} \, dS_k. \tag{4.26}$$

and internal force vector is

$$F_{i,\text{int}}^{n+1}\left(u_i^{n+1}\right) = \sum_{k=1}^{ip} \int_{\partial V_k} \sigma_{ij}^{n+1} n_j \, dS_k, \tag{4.27}$$

When an inelastic load takes place, the equilibrium equation (4.19) is non-linear, then a special approach to solve such problem must be considered. This is the main concern of the Subsection 4.5 that describe in details the linearization method used.

4.5 Nonlinear numerical procedure

In this section is discussed the nonlinear procedure applied to the linearization of non-equilibrium equations, namely Newton-Raphson method. Such technique is broadly employed in numerical methods to analyze the solution of both coupled and uncoupled nonlinear equations. This application is used to the structural level (or global one), as well as to perform corrections over the stress-state at the material level (or integration points). The solution is solely achieved, at each time increment, when the global and local levels are within a given tolerance.

4.5.1 Non-equilibrium equations at the nodal level

When an inelastic load increment takes place, the equilibrium relationship, Eq. (4.22), is nonlinear. Therefore, assuming a state of non-equilibrium for an initial estimated displacement u_i^n, one can rewrite Eq. (4.22) in a residual form introducing the iterative term δu as

$$A_{ij}^{n+1}\delta u_j^n = F_{i,\text{ext}}^{n+1} - F_{i,\text{th}}^{n+1} - F_{i,\text{int}}^{n} = R_i^n. \tag{4.28}$$

It is well known that Newton-Raphson approach is commonly used to linearize nonlinear equations and, providing at the same time fast convergence rate, since it has quadratic convenience near the root. During the iterative process, one is able to ensure that the equilibrium condition is achieved using

$$\delta u_i^n = -\left[\frac{dR_i}{d\delta u_j}\right]^{-1} R_j^n, \tag{4.29}$$

where $\left[\dfrac{dR_i}{d\delta u_j}\right] \equiv A_{ij}$.

The displacement vector is updated using the following approximation:

$$u_i^{n+1} = u_i^n + \delta u_i^n, \tag{4.30}$$

and the increment Δu_i^{n+1} is evaluated using the last converged displacement calculated in the previous increment u_i^*

$$\Delta u_i^{n+1} = u_i^{n+1} - u_i^*. \tag{4.31}$$

The next step is to visit each element and calculate the stress increment at each integration point, k, using Eq. (3.80), which is rewritten in an incremental form as

$$\Delta\sigma_{ij}^{n+1} = D_{ijlm}^{ep,n+1}\sum_{p=1}^{nve}\left[L_{lm}N_p\Delta u_{m(p)}^{n+1} - N_p\Delta\varepsilon_{lm(p)}^{n+1,th}\right]_k, \tag{4.32}$$

and the new stress tensor is updated, in each integration point k, in terms of the previous converged stress-state σ_{ij}^{*}

$$\sigma_{ij}^{n+1} = \sigma_{ij}^{*} + \Delta\sigma_{ij}^{n+1}. \tag{4.33}$$

With the stress field given by Eq. (4.33) and using Eq. (3.43), one is able to observe whether the nature of the stress state is elastic or inelastic in each integration point of each element. As it was mentioned in Subsection 3.2.7, in the context of rate independent plasticity, if $f < 0$, the stress state is elastic. Therefore, Eq. (4.33) represents the current stress field and $D_{ijkl}^{ep,n+1} = D_{ijkl}^{e,n+1}$, i.e. no corrections are necessary for this case. Otherwise, if $f \geq 0$, corrections on the stress state, as well as upon the tangent modulus $D_{ijkl}^{ep,n+1}$ $\left(D_{ijkl}^{p,n+1} = \dfrac{\partial\sigma_{ij}}{\partial\varepsilon_{kl}}\right)$ must be performed. The same can be said in the context of viscoplasticity with initial yield stress. The approach responsible for this process is presented in the next section (Sec. 4.5.2), and it is called *return mapping*.

The next step, in the nonlinear solution process, is calculate the internal force vector at the nodes. If no yields in strength take place, the stress obtained with Eq. (4.33) is going to be used; on the other hand, if the material yields, the stress tensor is evaluated with the stress field provided by the return mapping.

Independently of whether the stress state is elastic or inelastic, the new internal force must be calculated by integrating the previous stress tensor evaluated at the integration point. Such integration procedure is performed by Eq. (4.27) and from this information, the new residual vector is given by

$$R_i^{n+1}\left(u_i^{n+1}\right) = F_{i,\text{th}}^{n+1} + F_{i,\text{ext}}^{n+1} - F_{i,\text{int}}^{n+1}\left(u_i^{n+1}\right). \tag{4.34}$$

The iteration process stops when a given convergence criterion is satisfied. For the purpose of this application is adopted the L^2 norms of the ratio of the residual R and external force vector F_{ext} as a convergence criterion, which can be expressed by

$$\frac{\|R\|}{\|F_{\text{ext}}\|} < \xi, \tag{4.35}$$

where ξ is the tolerance. In this work, ξ is set to 10^{-10} for all cases studies investigated.

The flowchart of the incremental procedure for the solution of the non-equilibrium equations is shown in Flowchart 4.5.1. This methodology requests the update of the stiffness matrix, at each integration point of the element, at each force increment when yield occurs.

Flowchart 4.5.1: Non-equilibrium integration procedure

I. Initial guess

$$u_i^* := u_i^n; \quad R_i^n := F_{i,\text{th}}^{n+1} + F_{i,\text{ext}}^{n+1} - F_{i,\text{int}}^{n}\left(u_i^n\right)$$

II. Evaluate the tangent matrix at each integration point k

$$D_{ijkl}^{ep,n+1} = \frac{\partial \sigma_{ij}^{n+1}}{\partial \varepsilon_{kl}^{n+1}}$$

III. Evaluate the stiffness matrix

$$A_{ij}^{n+1} = \sum_{k=1}^{ip} \int_{\partial V_k} n_j D_{ijlm}^{ep,n+1} \left[\sum_{p=1}^{nve} L_{lm} N_p \right]_k dS_k$$

IV. The new iterative displacement field is calculated

$$\delta u_i{}^n = -A_{ij}^{-1} R_j\left(u_i^n\right)$$

V. The displacement field is updated

$$u_i^{n+1} = u_i^n + \delta u_i^n \text{ and } \Delta u_i^{n+1} = u_i^{n+1} - u_i^*$$

VI. Stress tensor is evaluated at the integration point

$$\Delta \sigma_{ij}^{n+1} = D_{ijlm}^{e,n+1} \sum_{p=1}^{nve} \left[L_{lm} N_p \Delta u_{m(p)}^{n+1} - N_p \Delta \varepsilon_{lm(p)}^{n+1,th} \right]_k$$

$$\sigma_{ij}^{n+1} = \sigma_{ij}^* + \Delta \sigma_{ij}^{n+1}$$

VII. *Return Mapping* routine

Input (σ_{ij}^{n+1}) Output $(\sigma_{ij}^{n+1}, D_{ijkl}^{ep,n+1})$

VIII. Evaluate the internal force and the new residual vector

$$R_i^{n+1}\left(u_i^n\right) = F_{i,\text{th}}^{n+1} + F_{i,\text{ext}}^{n+1} - F_{i,\text{int}}^{n+1}\left(u_i^n\right)$$

IX. Check the tolerance $\frac{\left\|R^{n+1}\right\|}{\left\|F_{\text{ext}}^{n+1}\right\|} < \xi$. If ξ satisfies, then set $(\cdot)^n := (\cdot)^{n+1}$ and **EXIT**. Otherwise, **GO TO** III.

4.5.2 Implicit numerical integration of the return mapping

For the treatment of the nonlinear equations involved in this theory is assumed an implicit integration scheme in time, which is linearized via the Newton–Raphson method. The reasons behind that choice lie on the stability and quadratic convergence rate near the root. Therefore, in case of plasticity or viscoplasticity loads, the aforementioned numerical approach is used to correct the stress state, at the integration point, in terms of the internal parameters when required. The index notation is not used in section for the sake of clarity.

It is important to mention that the integration performed in this section works for 2D and 3D domains without any restriction with exception for plane stress; since, for such case, is necessary also ensure that the out-of-plane component σ_{zz} is equal to zero at each iteration. The implementation used in this work for plane stress in particular is based on Neto *et al.* (2011).

In the return mapping procedure, the stress field calculated in Eq. (4.33) is adopted as the candidate stress tensor

$$\sigma^{n+1} = \sigma^{c} \tag{4.36}$$

Once the material yields, the condition of a plastic load is verified and the stress state must be corrected with the insertion of the inelastic strain increment

$$\Delta\varepsilon^{i,n+1} = \Delta\bar{\varepsilon}^{n+1}\sqrt{\frac{3}{2}}\frac{S}{||S||}. \tag{4.37}$$

This representation is well suited in rate independent load cases. However, the multiplier parameter, $\bar{\varepsilon}$, in the rate dependent load context is presented according to the model in Eq. (3.61), i.e.

$$\Delta\bar{\varepsilon} = \begin{cases} \Delta t\left(\dfrac{\sigma_{eq}-\sigma_{y}}{K_{p}}\right)^{N_{\varepsilon}} & \text{if} \quad f=(\sigma,\sigma_{y})\geq 0 \\ 0 & \text{if} \quad f=(\sigma,\sigma_{y})<0 \end{cases} \tag{4.38}$$

and finally the stress-strain relation can be written with inclusion of the inelastic strain as

$$\sigma^{n+1} = \sigma^{c} - D^{e}\Delta\bar{\varepsilon}^{n+1}\sqrt{\frac{3}{2}}\frac{S(\sigma^{n+1})}{||S(\sigma^{n+1})||}. \tag{4.39}$$

where $\sigma^{c} = \sigma^{*} + \Delta\sigma^{n+1}$.

In order to differentiate the return mapping equations from the equilibrium procedure, the iterative superscript j is adopted instead of n.

Therefore, from Eqs. (4.39) and (3.43), the residual function written as follows

$$R_{\sigma}^{j} = [D^{e}]^{-1}\left(\sigma^{j} - \sigma^{c}\right) + \Delta\bar{\varepsilon}^{j}\sqrt{\frac{3}{2}}\frac{S(\sigma^{j})}{||S(\sigma^{j})||}, \tag{4.40}$$

$$R_{\bar{\varepsilon}}^{j} = \sigma_{eq} - \sigma_{y}(\Delta\bar{\varepsilon}^{j}). \tag{4.41}$$

Applying the Newton-Raphson method for Eqs. (4.40) and (4.41),

$$\begin{bmatrix} \delta\sigma^{j+1} \\ \delta\bar{\varepsilon}^{j+1} \end{bmatrix} = -[J]^{-1}\begin{bmatrix} R_{\sigma}^{j} \\ R_{\bar{\varepsilon}}^{j} \end{bmatrix}, \tag{4.42}$$

where J is the Jacobian matrix, which is given by

$$J = \begin{bmatrix} \dfrac{\partial R_{\sigma}}{\partial\sigma} & \dfrac{\partial R_{\sigma}}{\partial\bar{\varepsilon}} \\ \dfrac{\partial R_{\bar{\varepsilon}}}{\partial\sigma} & \dfrac{\partial R_{\bar{\varepsilon}}}{\partial\bar{\varepsilon}} \end{bmatrix}. \tag{4.43}$$

The new stress state and inelastic internal variable are updated as follows:

$$\sigma^{j+1} = \sigma^{j} + \delta\sigma^{j+1}, \tag{4.44}$$

$$\bar{\varepsilon}^{j+1} = \bar{\varepsilon}^{j} + \delta\bar{\varepsilon}^{j+1}. \tag{4.45}$$

These values are used to update the incremental terms

$$\Delta\sigma^{j+1} = \sigma^{j+1} - \sigma^{j}, \tag{4.46}$$

$$\Delta\bar{\varepsilon}^{j+1} = \bar{\varepsilon}^{j+1} - \bar{\varepsilon}^{j}. \tag{4.47}$$

The above parameters are used to update the residue vectors R_{σ}^{j+1} and $R_{\bar{\varepsilon}}^{j+1}$.

When the numerical iterative processes reach the convergence criterion, the tangent modulus $\left(D^{ep} = \left.\dfrac{\partial\sigma}{\partial\varepsilon}\right|^{n+1}\right)$ is evaluated using the following expression

$$\begin{bmatrix} \partial\sigma^{j+1} \\ \delta\bar{\varepsilon}^{j+1} \end{bmatrix} = \begin{bmatrix} D_{11} & D_{12} \\ D_{21} & D_{22} \end{bmatrix}\begin{bmatrix} \partial\varepsilon^{j+1} \\ 0 \end{bmatrix}, \tag{4.48}$$

where $\left.\dfrac{\partial\sigma}{\partial\varepsilon}\right|^{n+1} = D_{11}$. This result leads to $D^{ep} = D_{11}$, which is the new tangent matrix at the integration point. The *return mapping algorithm* is summarized in Flowchart 4.5.2. A more detailed description of the this procedure is given in Appendix B.2.

Flowchart 4.5.2: Return mapping algorithm

I. Check the stress state

$$\sigma^j = \sigma^c - D^e \Delta\bar{\varepsilon}^j \sqrt{\frac{3}{2}} \frac{S^j}{||S^j||}$$

$$f\left(\sigma^j, A^j\right) = \sqrt{3J_2(\sigma^j)} - \sigma_y(\bar{\varepsilon}^j)$$

If the stress state is within of the elastic region, i.e. $f < 0$, then

$$\sigma^{j+1} = \sigma^c, \quad \text{and} \quad \sigma_y(\bar{\varepsilon}^{j+1}) = \sigma(\bar{\varepsilon}^j)$$

and **EXIT**. Otherwise:

II. Calculate the residuals

$$R_\sigma^j = [D^e]^{-1}\left(\sigma^j - \sigma^c\right) + \Delta\bar{\varepsilon}^j \sqrt{\frac{3}{2}} \frac{S^j}{||S^j||}$$

$$R_{\bar{\varepsilon}}^j = \sqrt{3J_2\left(\sigma^j\right)} - \sigma_y(\bar{\varepsilon}^j)$$

III. Evaluate the Jacobian matrix

$$J = \begin{bmatrix} \frac{\partial R_\sigma}{\partial \sigma} & \frac{\partial R_\sigma}{\partial \bar{\varepsilon}} \\ \frac{\partial R_{\bar{\varepsilon}}}{\partial \sigma} & \frac{\partial R_{\bar{\varepsilon}}}{\partial \bar{\varepsilon}} \end{bmatrix}$$

IV. Determination of the corrections

$$\begin{bmatrix} \delta\sigma^{j+1} \\ \delta\bar{\varepsilon}^{j+1} \end{bmatrix} = -[J]^{-1} \begin{bmatrix} R_\sigma^j \\ R_{\bar{\varepsilon}}^j \end{bmatrix}$$

V. Update the variables

$$\sigma^{j+1} = \sigma^j + \delta\sigma^{j+1}$$

$$\bar{\varepsilon}^{j+1} = \bar{\varepsilon}^j + \delta\bar{\varepsilon}^{j+1}$$

and

$$\Delta\sigma^{j+1} = \sigma^{j+1} - \sigma^j$$

$$\Delta\bar{\varepsilon}^{j+1} = \bar{\varepsilon}^{j+1} - \bar{\varepsilon}^j$$

VI. Check the convergence criteria, i.e. $||R_\sigma^{j+1}||$ e $||R_{\bar{\varepsilon}}^{j+1}|| < \xi$.

If it is satisfied, then set: $\sigma^{n+1} = \sigma^{j+1}$ e $D^{ep} := D_{11}$, and **EXIT**. Otherwise, **GO TO** III.

5 NUMERICAL VALIDATION

In this chapter, the EbFVM numerical implementation is applied to different physical models in order to verify the efficiency and accuracy of the method. In particular, the solution provided by EbFVM is compared with well known analytical solutions, from the literature, as well as numerical ones (when the applied model does not provide such analytic solution), which is analyzed via commercial simulator under FEM viewpoint.

5.1 The classical one-dimensional semi-infinity Stefan problem

The classical one-dimensional semi-infinity Stefan problem that brings the analytical solution for an idealized liquid-solid moving boundary is used as a verification test case for the EbFVM numerical implementation. Initially, the semi-infinity domain is at uniform liquid temperature $T_l = 1494.45$ °C. At time $t = 0$, a constant temperature $T_0 = 1000$ °C (Dirichlet boundary condition) is instantaneously applied at the surface $x = 0$ and it remains unchanged during the cooling process. The rest of the boundaries are kept thermally isolated (Neumann boundary), as it is pictured in Fig. 13. In the numerical procedure, as the time increases, $t > 0$, the liquid region gradually solidifies with an imposed narrow mushy zone of 0.1 °C, which can be used as an approximation of the analytical single melting point temperature T_m (KORIC; THOMAS, 2008).

Figure 13 – One-directional solidification domain representation with bi-linear quadrilateral elements and its boundary conditions.

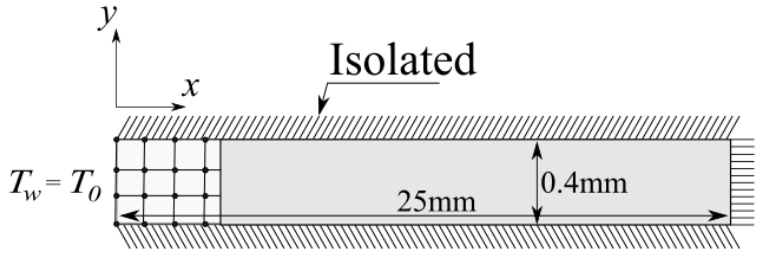

This analytical solution was first proposed by Carslaw and Jaeger (1959). Others equivalent examples of the Stefan problem often used to validate the solidification with moving boundary process can be seen in (VOLLER; CROSS, 1981; LI; THOMAS, 2003). These idealized problems are able to give a better insight of the dynamics of the solid-liquid interface in the phase change phenomena. For this current application, the two-dimensional EbFVM numerical

model uses a regular distributed density mesh containing 300 (5×60) bi-linear quadrilateral elements and the thermophysical properties shown in Table 4.

Table 4 – Parameters used in the numerical example.

Properties (Unit)	value
Conductivity (W/mK)	33.0
Specific heat (kJ/kgK)	0.661
Latent heat (kJ/kg)	272.0
Density (kg/m^3)	7500.0
Melting temperature, T_m (°C)	1494.4
Liquid temperature T_l (°C)	1494.45
Solidus temperature T_s (°C)	1494.35
Wall surface temperature, T_w (°C)	1000.0

Fig. 14 presents the solidification evolution of both numerical and analytical approaches at 5 time levels (1, 5, 10, 20, and 40 s). From the results, one can conclude that the numerical results are in good agreement with the analytical solution at each time level.

Figure 14 – Comparison of numerical and analytical temperature solution throughout a semi-infinite plane at different time levels.

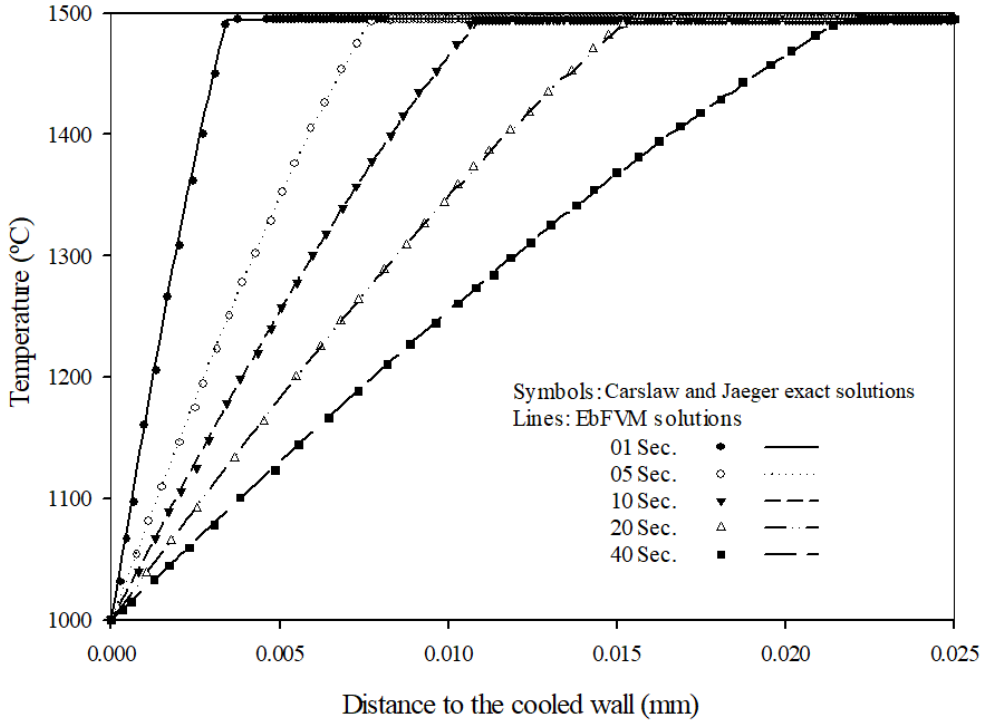

Guided by the results, it is worth to point out that the two-dimensional EbFVM implementation was able to handle a phase change problem and provide a satisfactory solution using a relatively coarse mesh.

5.2 Mechanics benchmark tests

In this section is presented cases studies to show the performance of the EbFVM in CSM field. These tests cases assume the material properties of aluminum and are divided into two parts: (I) Mechanical and (II) Thermal load. Herein, it was chosen the geometry illustrated in Fig. 15, where the pure mechanical load is applied in the domain described in Fig. 15a and thermal expansion is used in the geometry pictured in Fig. 15b.

Figure 15 – Investigated domains - a) plate with a circular hole; and b) section of cylinder.

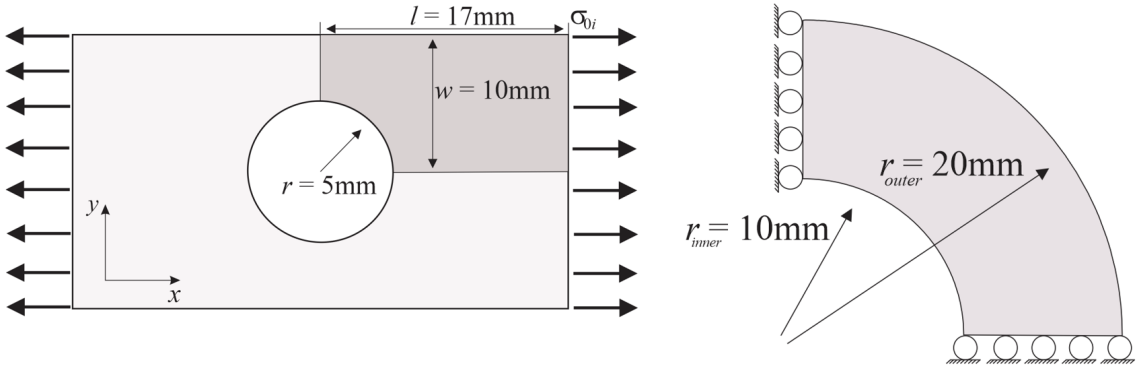

The mechanical properties of the aluminum, required to define the elastic modulus are given by: Young's modulus E = 70 GPa and Poisson's ratio $\nu = 0.2$. For the thermal load case study, in addition to the two aforementioned parameters, the thermal expansion coefficient is also used, $\alpha = 2.1 \times 10^{-5}$. The yield function for the linear plasticity relation was chosen as

$$\sigma_y(\bar{\varepsilon}) = \sigma_0 + H'\bar{\varepsilon} \tag{5.1}$$

where σ_0 is elastic limit stress, which is equal to 0.243 GPa. The angular coefficient, H', for linear plasticity, is equal to 0.2 GPa and for the perfectly plastic scenario, it is equal to 0.0 GPa.

The numerical results are compared with a reference solution, which is assumed to be the numerical result obtained with a refined mesh composed of 7,000 elements and 7,697 nodes. In order to better analyze the EbFVM accuracy, the results are also compared with the solution provided by the commercial simulator, ABAQUS, which uses the Galerkin-FEM.

5.2.1 Mechanical load

In this subsection, numerical tests are carried out using the geometry corresponding to a plate with a hole at the center. This plate is stretched at its minimum section in opposite

directions, as shown in Fig. 15. The analyses of this numerical experiment is performed from the point of view of perfect and linear plastic loads for plane strain and plane stress assumptions. For symmetry reasons, only one-quarter of plate is investigated, i.e. the gray region depicted in Fig. 15a.

For the domain in Fig. 15a, at the symmetry line, the boundary condition is given by prescribed displacements (Dirichlet condition) and uniform surface tension (Neumann condition) of $\sigma_{0i} = 0.1$ MPa at the minimum section. To avoid rotation and translation of the domain, only one degree of freedom is fixed at each symmetry lines. Therefore, the displacement in the $x-axis$ is fixed in the $y-$direction and, in the $y-axis$, the displacement is restricted in the $x-$direction. For all simulations, the total load (0.1 MPa) is divided into 10 increments and the tolerance of $\zeta = 10^{-10}$ is applied to check the global and local convergence levels in each load increment.

5.2.1.1 Plane strain approach

The convergence rate of the solution with mesh size is analyzed by for bolth EbFVM (Fig. 16a) and FEM (Fig. 16b). In order to make a fair comparison of the convergence rate of both approaches with the grid refinement, one generates each grid in ABAQUS and use it in the in-house simulator developed in this dissertation. Additionally, in the EbFVM context, the Newton-Raphson convergence rate at the global level is studied, using the last time load step, for the smallest size mesh employed.

Figure 16 – Equivalent stress using plane strain and perfectly plasticity assumptions. Analyzes of mesh size convergence. a) EbFVM; and b) FEM.

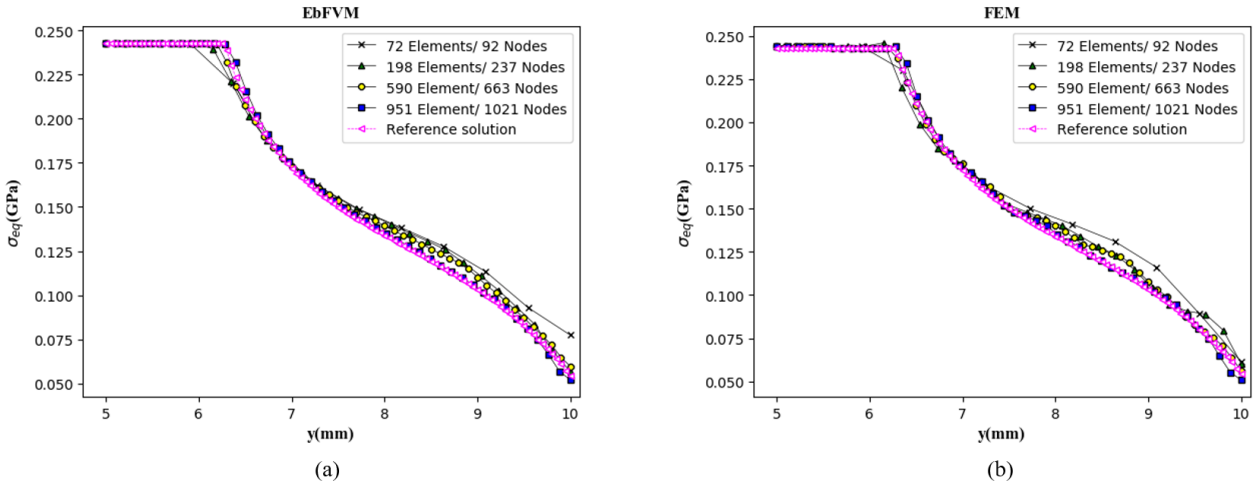

(a) (b)

From Fig. 16, one can notice the numerical experiments using EbFVM were able

to reach convergence rates equivalent to the ones using FEM. In particular, the mesh with 951 elements was enough to produce an acceptable approximated solution for both methods.

Using the mesh with 951 elements, the equivalent stress distribution, under plane strain and perfect plasticity assumption are shown in Figs. 17a and 17b, for EbFVM and FEM, respectively. Similar analyses are made, for linear plasticity, which are presented in Fig. 18. As an additional verification, the von Mises stress state along the minimum section of the plate obtained by EbFVM and FEM are compared in Fig. 19 and the convergence rate at the global level, for perfectly and linear plasticity are shown in Fig. 20.

Figure 17 – Equivalent stress field for plane strain and perfectly plastic assumption. a) EbFVM; and b) FEM.

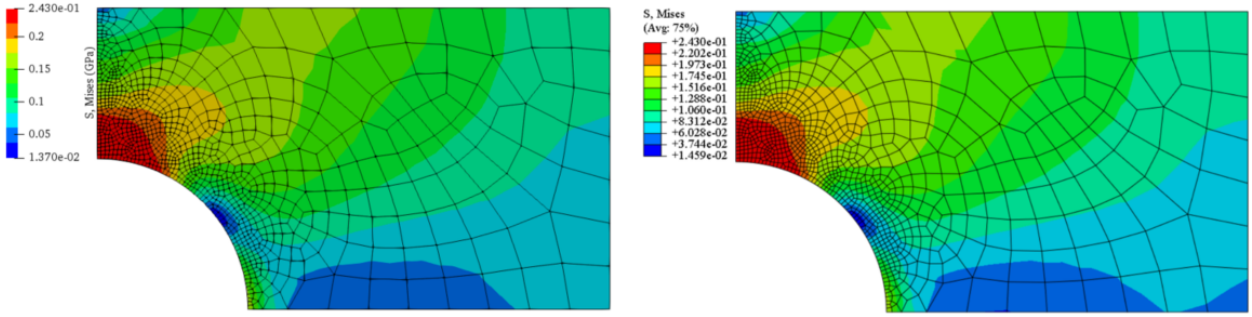

(a) (b)

Figure 18 – Equivalent stress field for plane strain and linear plasticity assumption. a) EbFVM; and b) FEM.

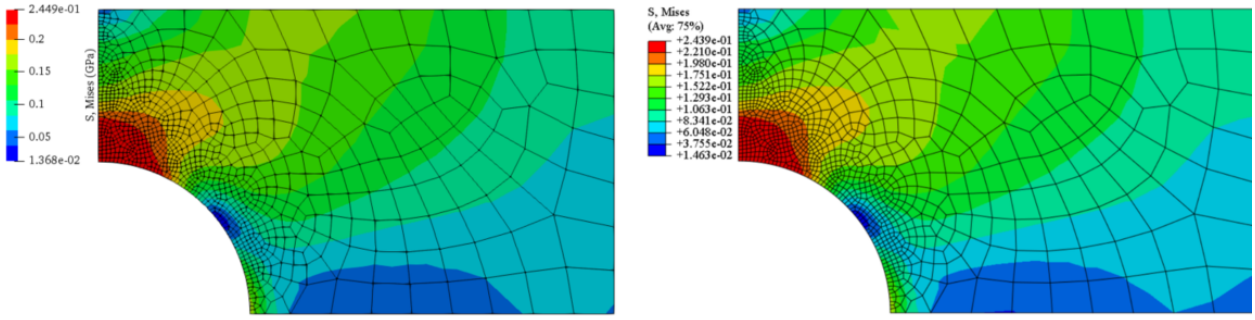

(a) (b)

It is important to acknowledge that, as expected, the numerical results of EbFVM and FEM are in good agreement as it can be observed in Figs. 17 through 19. Additionally, the convergence rate of the solution with the mesh size showed by EbFVM was analogous to the one achieved by FEM (Fig. 16). Quadratic convergence was achieved by the EbFVM at structural level (Fig. 20), which means this approach was able to handle efficiently the proposed nonlinear application.

Figure 19 – Plane Strain. Comparative equivalent stress between EbFVM and FEM. a) perfect plasticity; and b) linear plasticity.

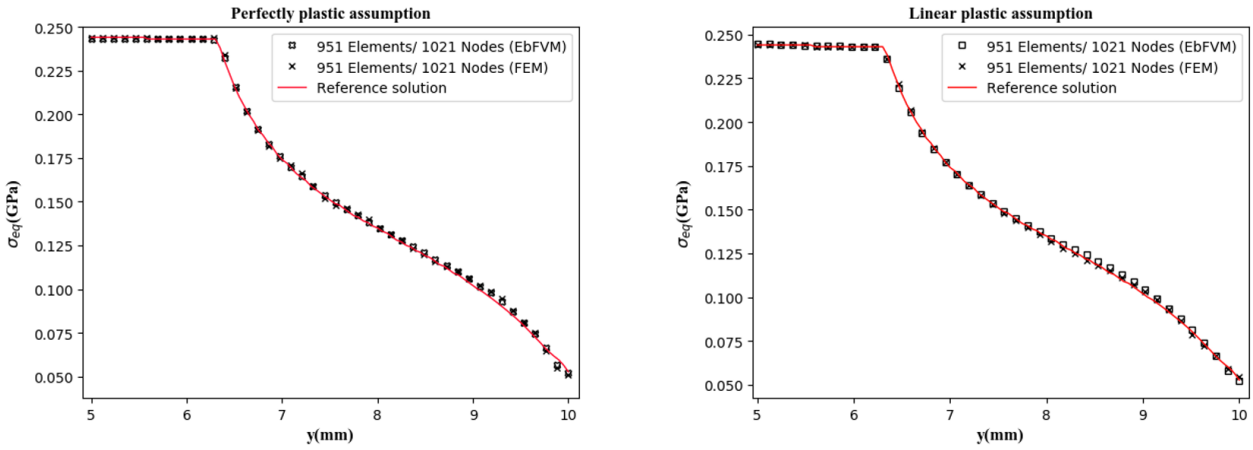

(a) (b)

Figure 20 – Plane Strain. Residue versus iterations for the last equilibrium increment for perfect and linear plasticity.

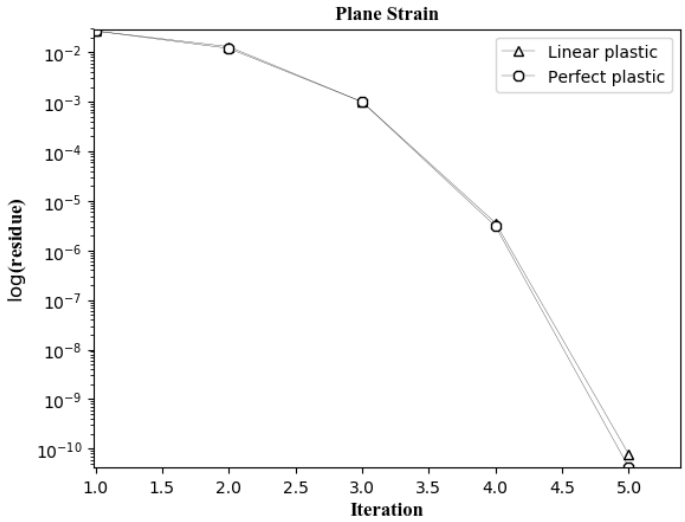

5.2.1.2 Plane stress approach

In order to make a full description of how EbFVM treats the two-dimensional CSM problems, herein the same analyses performed for plane strain is now applied to the plane stress. The major difference, in the numerical context, between plane strain and plane stress is that the last one needs to enforce a null normal stress in z-direction at the integration point. The results for plane stress are shown in Figs 21 through 23 using the finest mesh used for plane strain.

The equivalent stress state distribution is presented in Fig. 21 for perfect plasticity, and in Fig. 22 for linear plasticity. Additionally, von Mises stress profile along the minimum section of the plate is shown in Fig. 23.

Figure 21 – Equivalent stress field for plane stress and perfect plasticity assumption. a) EbFVM; and b) FEM.

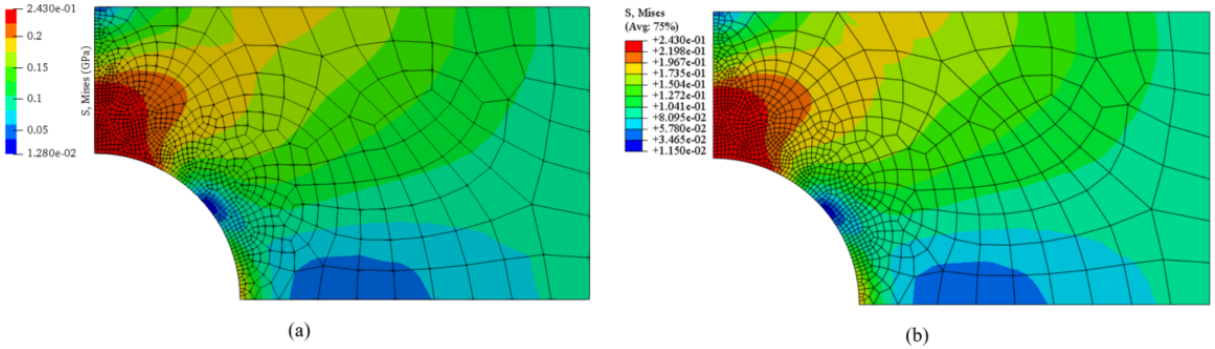

(a) (b)

Figure 22 – Equivalent stress field for plane stress and linear plasticity assumption. a) EbFVM; and b) FEM.

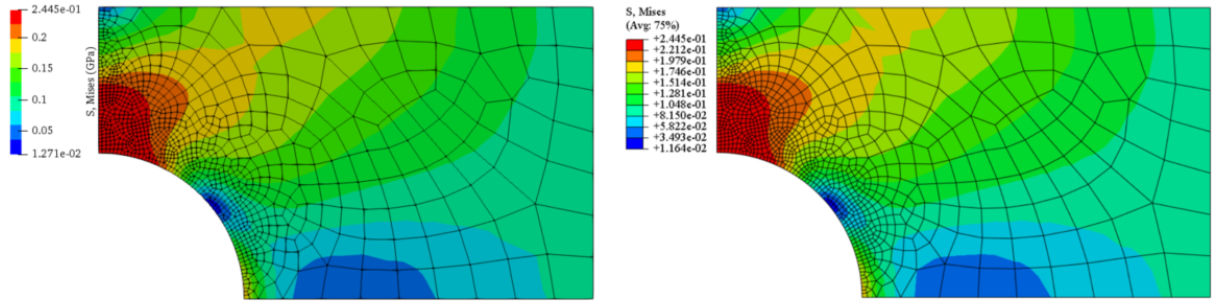

(a) (b)

Figure 23 – Plane Stress. Comparative equivalent stress between EbFVM and FEM. a) perfect plasticity; and b) linear plasticity.

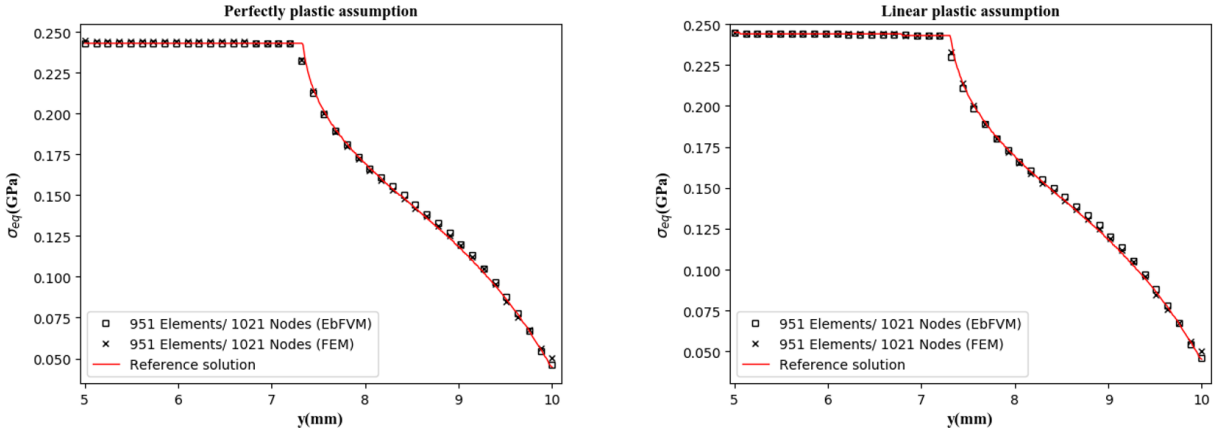

(a) (b)

As observed before, similar behavior already commented for plane strain is verified for plane stress. Once again, the results for both approaches are in good agreement to each another and with the reference solution, for perfect and linear plasticity. The results in terms of Newton-Raphson convergence rate in the plane stress context, for both perfect linear and perfect plasticity, are shown in Fig. 24. From this numerical information, it is possible to verify that five Newton iterations were more than enough to obtain a converged solution for both problems.

Additionally, one is able to observe quadratic convergence for linear and perfect plasticity.

Figure 24 – Plane Stress. Residue versus iterations for the last equilibrium increment for perfect and linear plasticity.

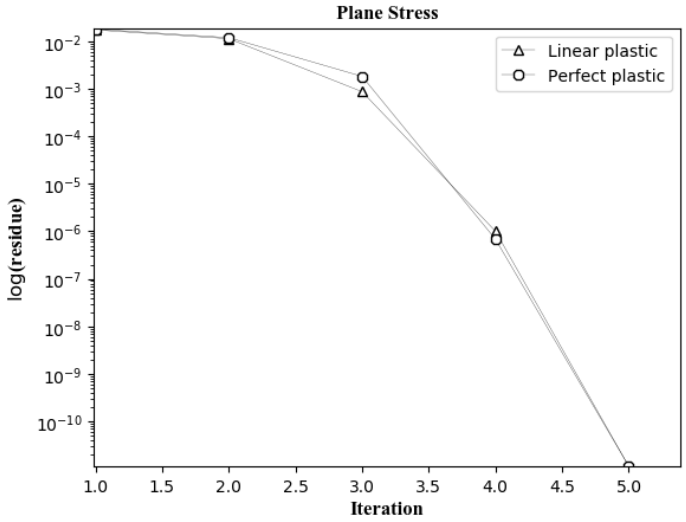

As it was noticed in Figs. 20 and 24, quadratic convergence is achieved by EbFVM for both numerical applications. Such property is important since problems that involve material nonlinearities are often numerically unstable using Newton's method.

5.2.2 Thermal load

5.2.2.1 Plane strain and stress test cases using constant material parameters

Now is investigated the nonlinear thermal load problem for the geometry shown in Fig. 15b. In order to numerically analyze the plastic loads, due to the thermal expansion, the energy and the momentum equations are solved separately. To the energy equation the following boundary conditions are applied: prescribed temperatures (Dirichlet) at the inner, $T_{inner} = 300\ ^{\circ}\text{C}$ and outer radius, $T_{outer} = 0\ ^{\circ}\text{C}$. Also, adiabatic (Neumann) boundary condition is imposed at the symmetry regions. The momentum equation is solved employing the temperature field as input at each time step in a procedure called weak coupling. In order to avoid rotation and translation of the domain Dirichlet boundary condition is applied by fixing one degree of freedom of the displacement at the symmetry surfaces, as depicted in Fig. 15b.

In order to compare the numerical solution obtained with EbFVM and FEM, the equivalent stress evaluated at the cross section corresponding to $y - axis$ and $x = 0$ is employed. The solution of both numerical approaches for perfect and linear plasticity are presented in Figs.

25 through 27 for plane strain and in Figs. 28 through 30 for plane stress, respectively. Unlike what was performed for the mechanical load described in previous section, herein only one mesh with 800 elements was used.

Figure 25 – Thermal plane strain. Comparative equivalent stress between EbFVM and FEM. a) Perfect plasticity and b) linear plasticity.

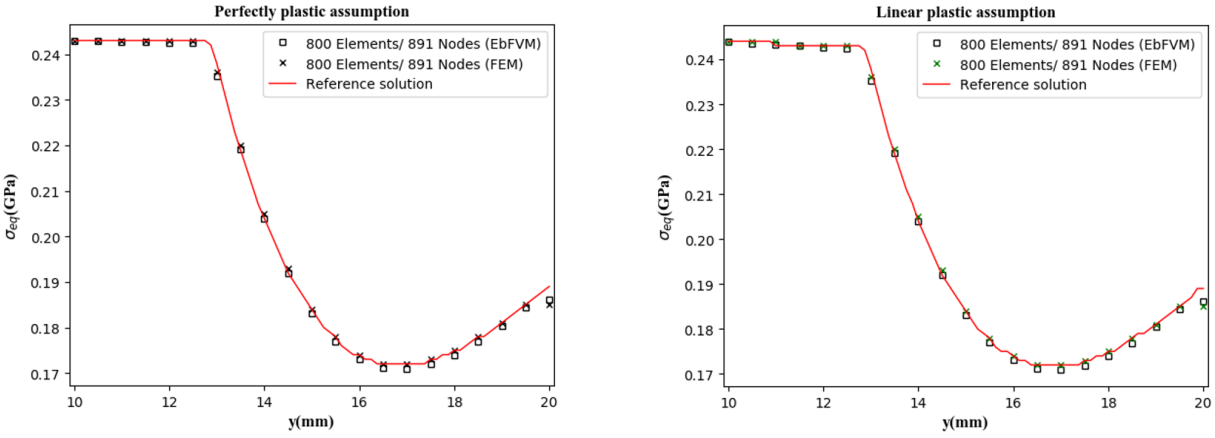

(a) (b)

Figure 26 – Plane strain. The von Mises distribution for perfect plasticity. a) Using EbFVM and b) using FEM.

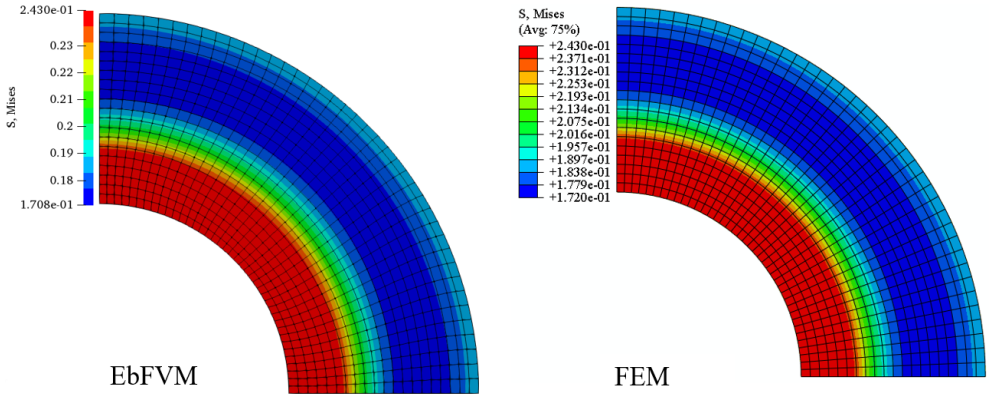

(a) (b)

From Figs. 25 through 30, one can verify that both numerical approaches are in agreement and the results are also close to the reference solution. A complete description of these applications are shown in more details in (PIMENTA; MARCONDES, 2019).

5.2.2.2 Linear thermal load with the shear modulus function of temperature

The goal of the numerical example carried out here is to verify the ability of the proposed numerical model in case that involve both thermal strain and non-homogeneous shear modulus (LI; THOMAS, 2004). From the view point of plane strain, the geometry depicted in

Figure 27 – Plane strain. The von Mises distribution for linear plasticity. a) Using EbFVM and b) using FEM.

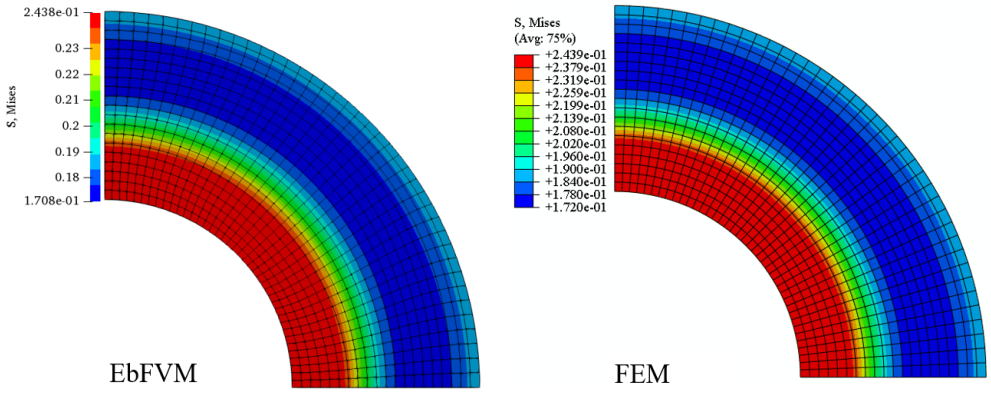

(a) (b)

Figure 28 – Thermal plane stress. Comparative equivalent stress between EbFVM and FEM. a) Perfect plasticity and b) linear plasticity.

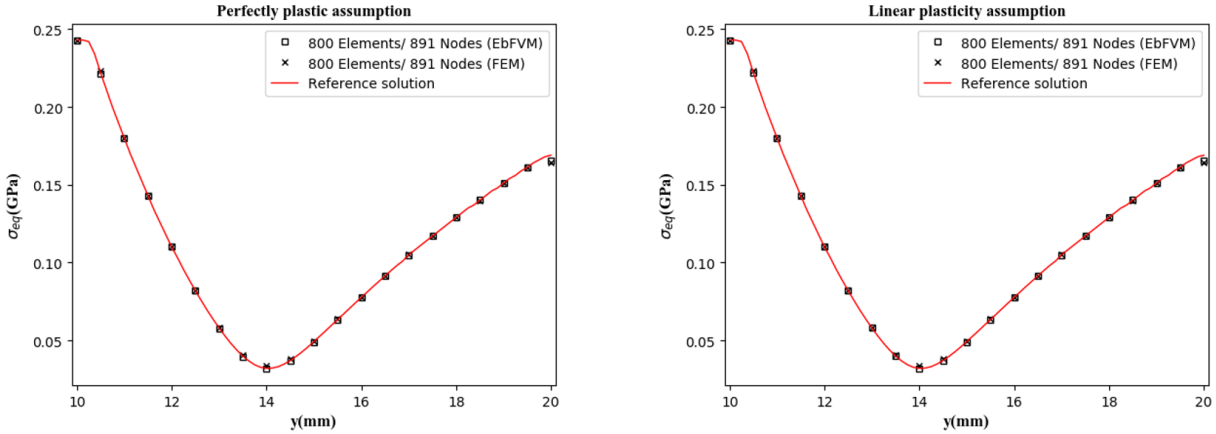

(a) (b)

Figure 29 – Plane stress. The von Mises distribution for perfect plasticity. a) Using EbFVM and b) using FEM.

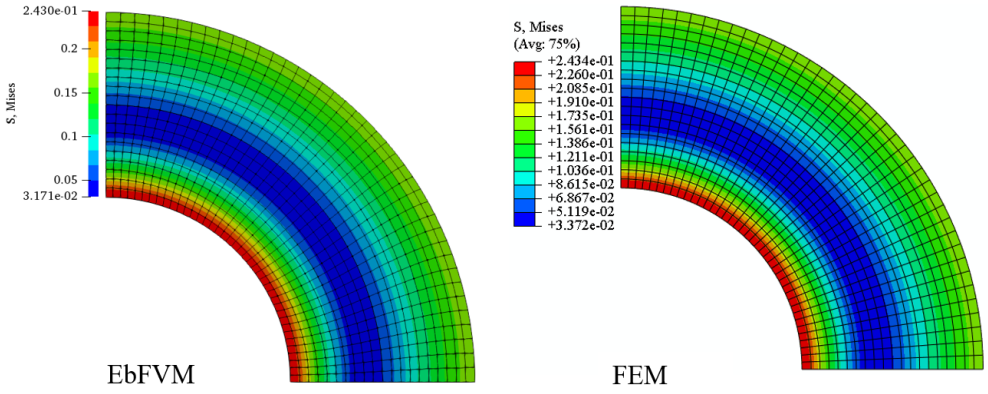

(a) (b)

Fig. 31 is subjected to a linear temperature distribution,

$$T(y) = 95y + 5,$$

Figure 30 – Plane stress. The von Mises distribution for linear plasticity. a) Using EbFVM and b) using FEM.

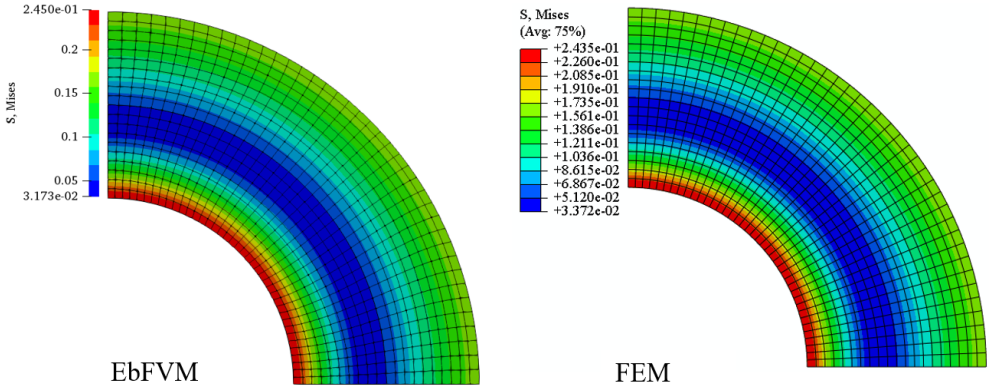

(a) (b)

as well as the shear modulus, $\mu(T)$, which is given by

$$\mu(T) = -aT + \mu_0,$$

where the angular and linear coefficients are $a = 15.23733$ MPa/°C and $\mu_0 = 7.95683 \times 10^4$ MPa, respectively. Further material properties besides the ones previously mentioned are the Poisson's rate, $\nu = 0.3$ and the thermal expansion coefficient, $\alpha = 0.125^{-4}$ °C^{-1}.

Figure 31 – Plate domain assuming shear modulus dependent of temperature

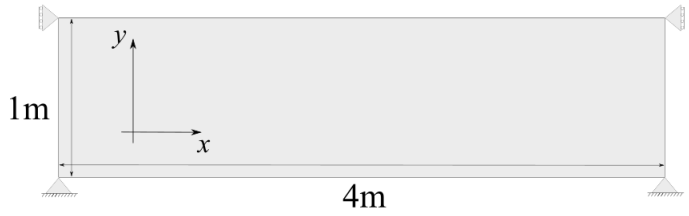

In order to verify how fast independently grid solutions are obtained, three uniformly distributed meshes are applied. The numerical results are compared with the analytical solutions given by Sladek *et al.* (1990), which are written as

$$\sigma_{xx}(y) = -2\alpha\frac{1+\nu}{1-\nu}\mu(T),$$

$$u_y(y) = \alpha\frac{1+\nu}{1-\nu}\left(\frac{95}{2}y+5\right)y.$$

As it can be verified in Fig. 32, accurate displacement solution is accomplished with the three mesh sets used (Fig. 32a). Although, in case of the stress component, σ_{xx}, along $y-axis$ ($x = 0.0$), an error of $\approx 6.64\%$ is verified with the coarsest mesh (50 elements and 66

nodes) as shown in Fig. 32b. However as expected, the error decreases when the mesh is refined.

Figure 32 – Numerical solutions and their computation with analytic ones: a) u_y displacement component; and b) σ_{xx} stress component along $y-axis$.

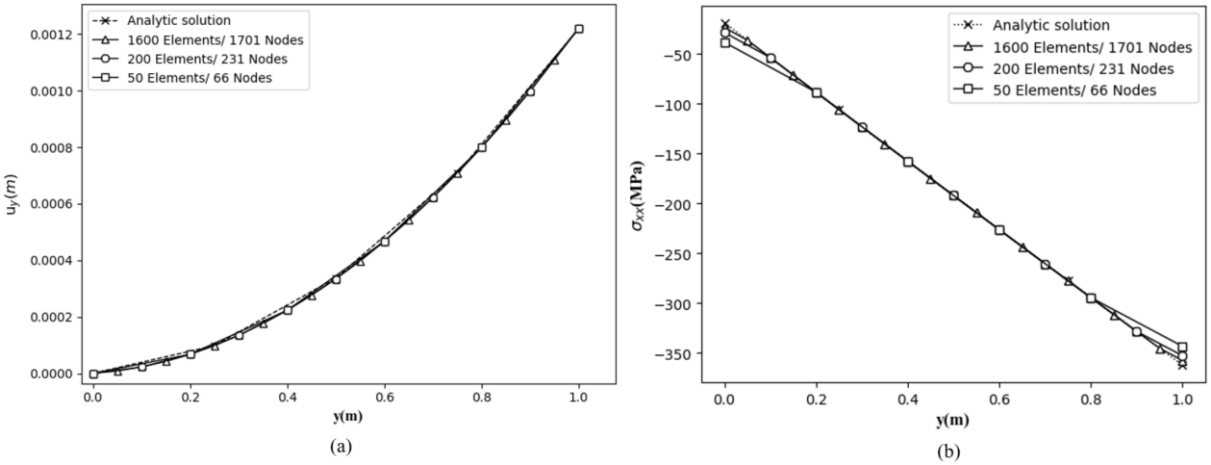

Similar results were provided by Zhu (1996) using FEM and according to this author, the numerical error of $\approx 6.64\%$ is considered to be within the engineering accuracy for this non-homogeneous problem.

5.2.3 Viscoplasticity

To the test cases carried out in this section is employed the power law form of the viscoplastic potential proposed by Perzyna and it is widely used in computational applications. Such representation is given by (NETO *et al.*, 2011).

$$\dot{\bar{\varepsilon}} = \begin{cases} \dfrac{1}{\mu_\varepsilon}\left[\dfrac{\sigma_{eq}}{\sigma_y} - 1\right]^{N_\varepsilon} & \text{if} \quad f(\sigma,\sigma_y) \geq 0 \\ 0 & \text{if} \quad f(\sigma,\sigma_y) < 0, \end{cases} \tag{5.2}$$

where μ_ε is the material viscosity-related parameter and N_ε is the rate sensitivity exponent.

The rate-dependent plasticity can be seen as a limit case of the viscoplastic theory, as it was discussed in Subsection 3.2.9. From this viewpoint, the benchmark procedure of the viscoplastic model may be obtained by using sufficient fast, as well as slow plastic load in order to verify the rate-independent limit. To demonstrate this behavior, herein is illustrated in Fig. 33 the applied force as a function of the displacement. For this case study is used the domain in Fig. 15a and material parameters: $\mu_\varepsilon = 500$ s, $N_\varepsilon = 0.5$, $E = 70$ GPa, $\nu = 0.3$, and time increments of $\Delta t = \{0.03, 0.05, 0.1, 1, 10, 1000\mathbf{s}\}$.

Figure 33 – Applied force as a function of displacement.

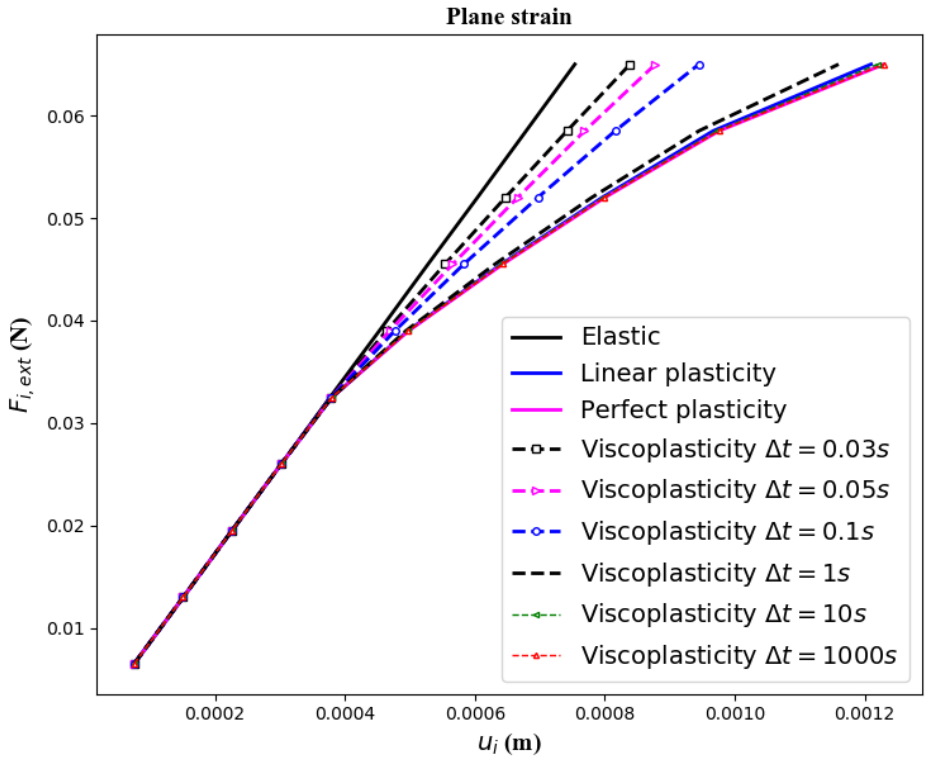

From Fig. 33, one is able to clearly notice that for a sufficient low load rate, the viscoplastic model recovers the behaviour of the rate-independent plasticity configuration with yield stress σ_0. Similar results can be accomplished in case of limit $\mu_\varepsilon \to 0$ (vanishing viscosity parameter) is considered. In addition, the rate-independent hypotheses theoretically behaves as a purely elastic process when the load rate is infinitely fast (or fast enough, which in this case is approximately $\Delta t = 0.03$ s), which is equivalent to say that the material has an infinitely viscosity ($\mu_\varepsilon \to \infty$). It is important to note that for any other load rate, as well as viscosity parameter, the corresponding external force *vs* displacement curve will lie between these two limits.

6 RESULTS

In this section is presented the numerical predictions of the thermal and thermo-mechanical behavior during the continuous casting of the steel grade AISI 1028. As it was previously discussed (Sec. 2.8), this solidification process is analyzed under two different casting conditions (I) casting velocity of 2.8 m/min with the initial temperature 1545 °C; (II) and casting velocity of 3.2 m/min with the initial temperature of 1535 °C.

In order to keep the simulations close to actual condition used in the numerical-experiment procedure introduced by Anjos *et al.* (2018), the casting water temperature, in the primary and secondary cooling stages, (T_{water}) and the environment temperature in the tertiary zone (T_{env}) were fixed and assumed to be equal to 28 °C and 25 °C, respectively.

As for the elastoplastic material model, the yield stress σ_y and the hardening modulus K_p are temperature dependent, together with Young's modulus E, Poisson's ratio ν and thermal linear expansion coefficient β (TLE). These mechanical properties for 0.3 wt% C steel are presented in Table 5.

Table 5 – Mechanical thermal dependent properties of steel (0.3 wt% C)

T (°C)	E(GPa)	ν	σ_y(MPa)	K_p(MPa)	β(TLE)
900	32.378	0.33	14.0	160.0	-0.01326
1000	20.00	0.33	11.0	160.0	
1100	14.542	0.33	8.0	160.0	
1200	12.896	0.33	5.5	160.0	-0.00675
1300	11.954	0.33	4.0	80.0	
1400	8.608	0.36	3.5	50.0	
1416				40.0	-0.00200
1450	5.062	0.40	1.9		
1490	0.097	0.41	0.5	7.0	-0.00029
1495	0.002	0.41	0.5	7.0	-0.00000

Source: Huespe *et al.* (2000).

To study the viscoplastic behavior is used the Odqvist's law, as previously discussed. Such representation, Eq. (3.61), gives the following non-linear equation:

$$f\left(\sigma_{ij},\bar{\varepsilon}\right)=\sqrt{\frac{3}{2}S_{ij}S_{ij}}-\left(\sigma_y+K_{\varepsilon}\dot{\bar{\varepsilon}}^{1/N_{\varepsilon}}\right) \tag{6.1}$$

where each parameter is temperature dependent. In the simulations this material information is based in the work of Bellet and Heinrich (2004) and they are shown in Table 6.

The numerical results are organized and discussed considering the three cooling stages individually for each casting velocity. In fact, the first is the mold region, subsequently

Table 6 – Thermal dependent viscoplasticity properties

T (°C)	K_ε(MPa/s$^{N_\varepsilon}$)	N_ε
845	859.4	0.201
895	635.4	
945	481.6	
995	373.1	
1045	294.7	
1095	236.8	
1145	193.2	
1195	159.9	
1245	134.0	
1345	97.2	
1395	84.0	
1439	74.3	0.201
1445	58.7	0.215
1473	5.8	0.266
1495	5.5	0.266

Source: Bellet and Heinrich (2004).

the sprays zone and radiation and natural convection, as it is discussed in Section 2.2. Such choice was made since the application of different heat transfer coefficient in each individual strand's faces is made only in primary cooling section. For the rest of the subsequent regions studied, the heat transfer coefficient equally changes for each strand's sides as the ingot's section descends through the casting machine. The stress state behavior, over the viewpoint of plane strain, is also presented for different points of the strand's surface as depicted in Fig. 7, which is repeated below. For the stress state distribution, the out-of-plane component is assumed, in view of that this information provide compressive and tensile information as the solidification occurs.

Figure 7 – Illustrative locations of the tracking points in the numerical domain.

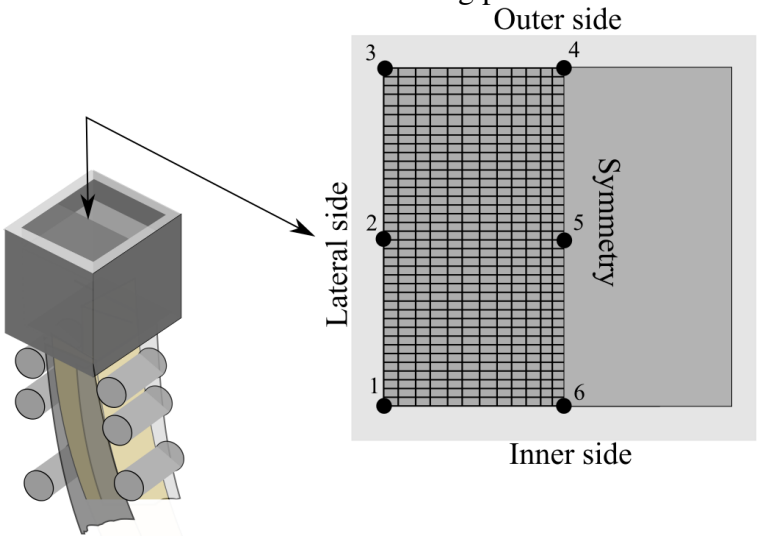

6.1 Mold region

For the mold region, the numerical solutions are presented for two casting conditions. These operational parameters are divided into two subsections, where in the first one is the casting velocity of 2.8 m/min and initial temperature 1545 °C. And the casting velocity of 3.2 m/min and initial temperature of 1535 °C is studied in second subsection.

6.1.1 First operational casting condition

The simulations under the view point of the casting velocity of 2.8 m/min and initial temperature 1545 °C is studied herein. In Fig. 34, the thermal distribution reveals the first stages of the solidification that corresponds to the preliminary shell formation at the meniscus and its growth as the strand exits the mold (i.e., at the positions: meniscus, 0.15, 0.29, 0.44 and 0.59). Moreover, the solidification evolution can be clearly seen through the decreasing of the liquid pool that presents a relatively large area at the meniscus. Owed to the rapid heat extraction, the solidified shell grows significantly fast.

Figure 34 – Thermal evolution during the casting velocity of 2.8 m/min at the primary cooling stage.

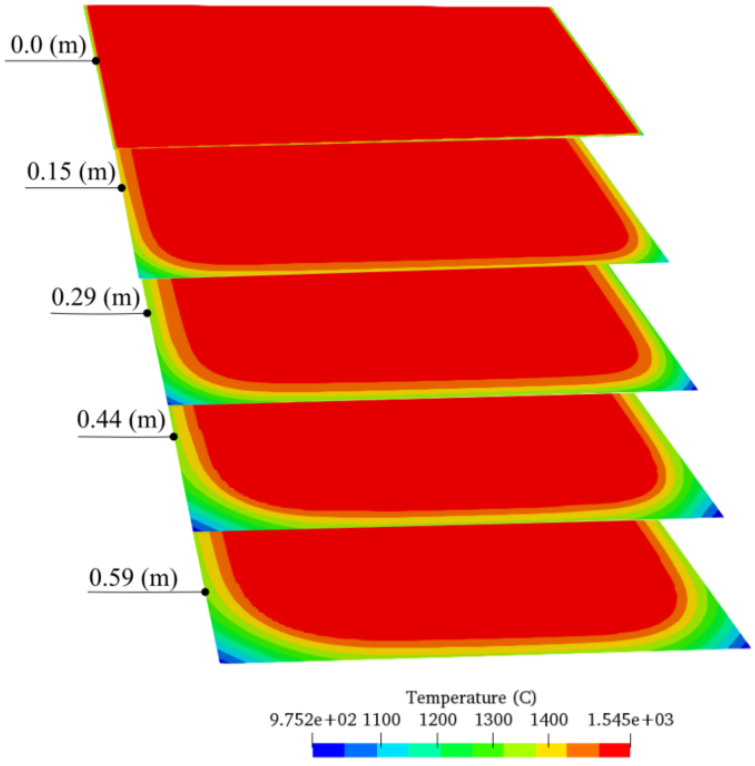

In Fig. 35 is provided the stress state at the mold exit that corresponds to the

solidification process history shown in Fig. 34. These representations also carry out different inelastic models that consider namely, the simplified form of Ramberg-Osgood law with both $K_p = 0$, Fig. 35a and the isotropic hardening ($K_p \neq 0$), Fig. 35b; and the viscoplastic model based on Odqvist's law, Fig. 35c. The temperature distribution is also presented in Fig. 35d, admitting the deformed configuration.

Figure 35 – Stress state and temperature distribution at the mold exit. The out-of-plane stress profile assumes: a) Ramberg-Osgood model with both $K_p = 0$; and b) isotropic hardening ($K_p \neq 0$); c) Odqvist's viscoplastic law; and d) thermal distribution during the casting velocity of 2.8 m/min.

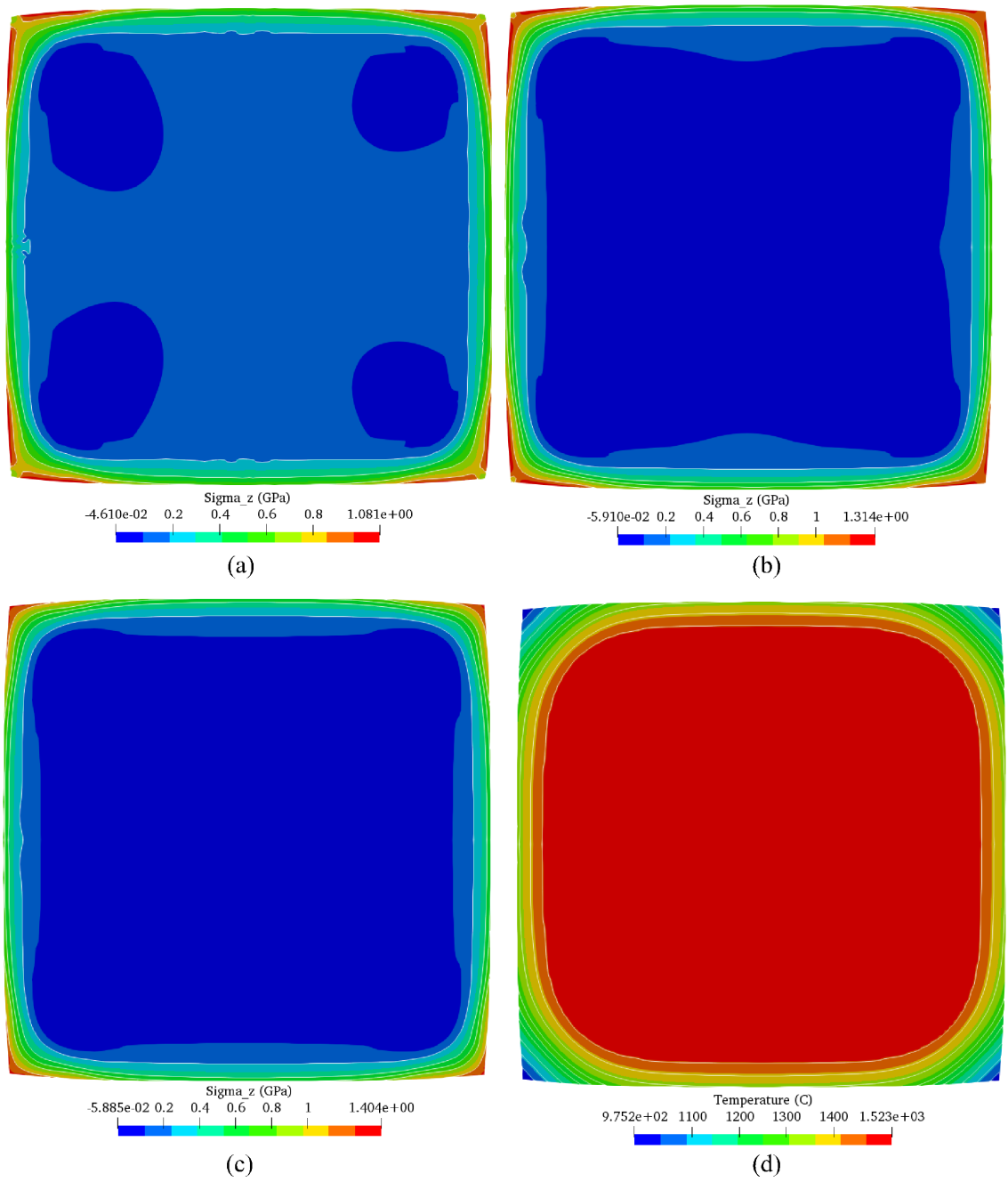

From Fig. 35, one is able to verify that the results present an evident change in shape of the strand (shrinkage). This process is responsible for the air gap formation, which decreases the heat transfer from the stand walls to the environment, leading to uneven temperature distribution. Another consequence of this phenomena is the unsymmetrical stress behavior that is observed in each inelastic model. Such outcome is direct related to the distinct effectiveness heat transfer coefficients obtained by Anjos (2013).

At the strand's corners are observed a compressive tensile stress (Figs 35 and 36), which is due to the cooling being more effective at this region. From the view point of Ramberg-Osgood model, such stress concentration can indicate a tendency of crack formation. However, the viscoplastic model indicates that the stress state can be alleviated (or decreased) as the time pass owed by the relaxation mechanism involved. In order to analyze the stress profile history at the corners (which corresponds to the points 1 and 3 in Fig. 7) during primary cooling stage, the stress components profile along the casting direction are presented in Fig. 36. From this perspective is possible to verify the aforementioned unsymmetrical stress response; such aspects are noticeable in all three models.

It is import to point out that the implemented numerical approach was able to predict the rapid increase in magnitude of the stress components, as the strand pass through the first cooling zone and the fast decreasing of those components at the beginning of the secondary cooling, as they are showed in Fig. 36. An explanation for this behavior lays on the intense heat extraction in the mold. Moreover, due to the less effective cooling process in the secondary stage, the stress components rapidly decrease.

In order to establish a comparative view of the three models, the equivalent displacement at midpoint of the side face is tracked as the strand descends through the casting machine i.e., in the course of the primary cooling stage until the entrance of the secondary one, Fig. 37. This information clearly pictures a small difference between Ramberg-Osgood model with isotropic hardening and the Odqvist's viscoplastic law. It is important to mention that Huespe *et al.* (2000) compared the Ramberg-Osgood plastic model (with isotropic hardening) with the viscoplastic law and data introduced by Kelly *et al.* (1988). This aforementioned application reported that the difference between the results was also very small and perhaps not significant.

From Figs. 35, 36 and 37, one can observe that the Ramberg-Osgoo, assuming $K_p = 0$, presents the highest values of equivalent displacement result among the applied models. However, such approach can still be used to supply safety parameters to avoid crack formation,

Figure 36 – Stress components at corner points. a) Ramberg-Osgood model with $K_p = 0$; b) Ramberg-Osgood model with isotropic hardening; and c) Odqvist's viscoplastic law.

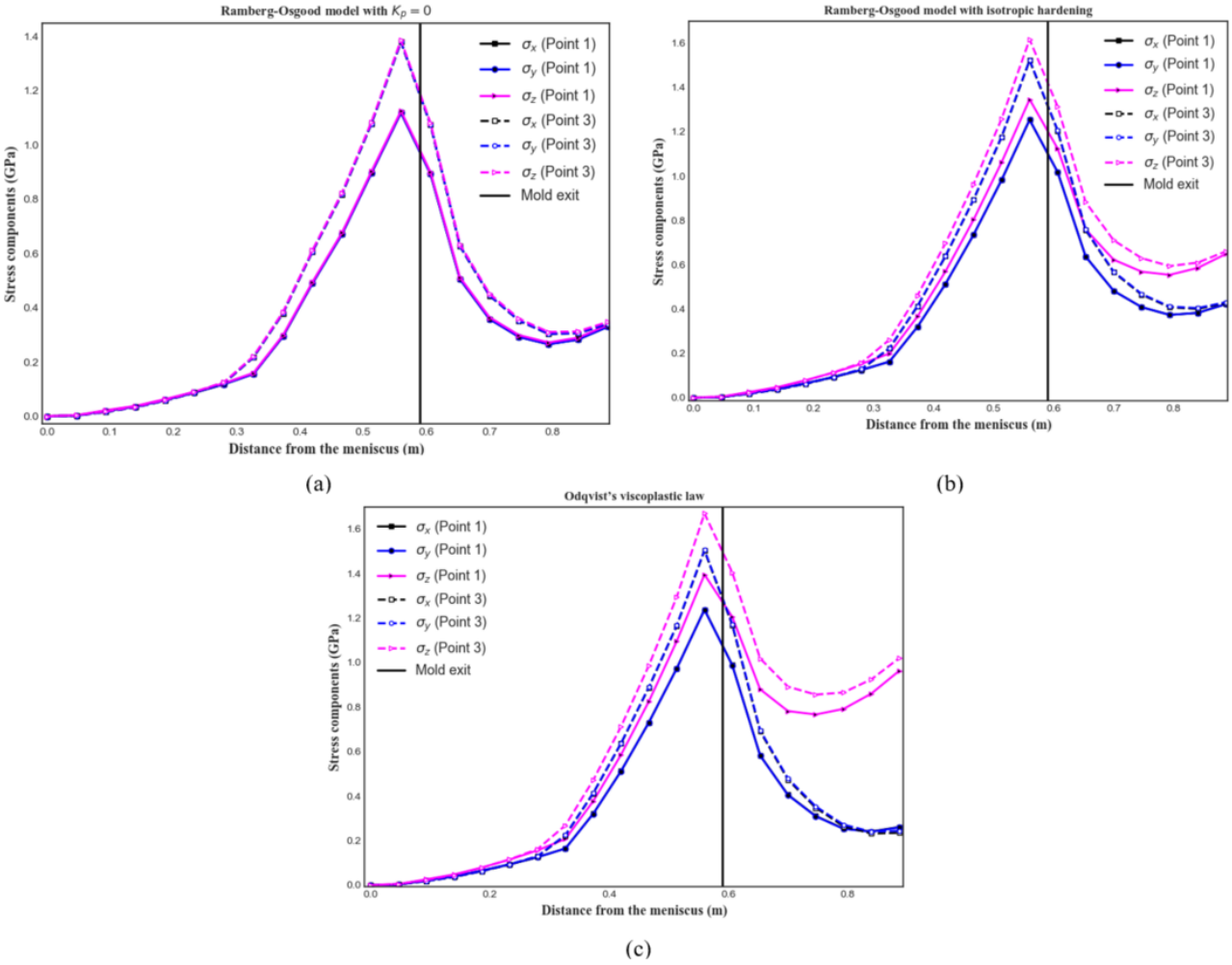

as it was employed in the works of Tszeng and Kobayashi (1989) and Du *et al.* (2018a).

6.1.2 Second operational casting condition

As for the second application is employed a higher casting velocity, specifically 3.2 m/min, and initial temperature of 1535 °C. The numerical analysis in the primary and the secondary cooling zones are presented in this section.

The thermal behavior as the strand initiates its solidification process is depicted in Fig. 38. In this stage, as it was pointed out for the first case, the solidification mechanism is considerable fast and starts at the meniscus. However, one is able to see that the shell growth formation is relatively smaller than the one in the previous numerical experiment. Such numerical information corroborates with the experimental results from (ANJOS *et al.*, 2018; ANJOS, 2013), which considers the casting velocity as one of the major parameters in metal making process.

Figure 37 – Equivalent displacement at midpoint of the lateral face along the primary and secondary cooling. This numerical solution assumes the casting velocity of 2.8 m/min.

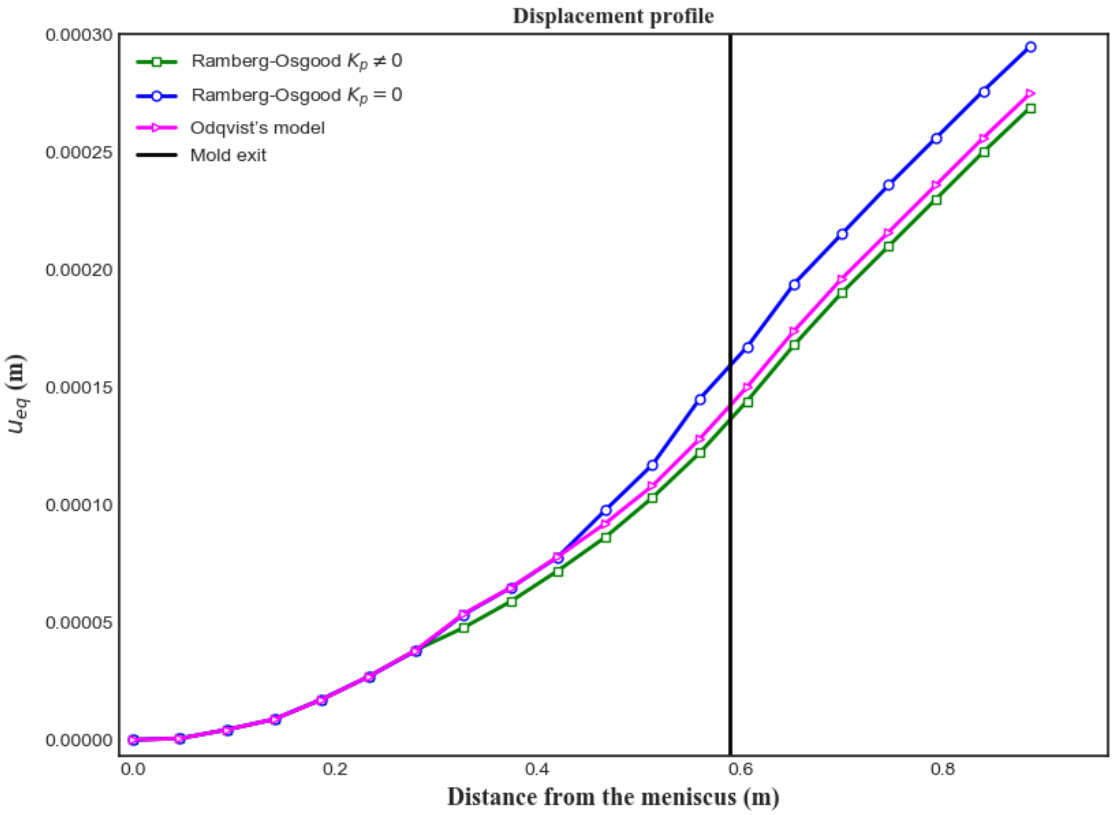

In Fig. 39 is presented the stress state at the mold exit as a result of the heat extraction history inside the primary cooling region. As it was similarly performed in the earlier section, the results carried out three inelastic models, which consider the simplified form of Ramberg-Osgood law assuming both $K_p = 0$, Fig. 39a, and the isotropic hardening ($K_p \neq 0$), Fig. 39b; as well as the viscoplastic model based on Odqvist's law, Fig. 39c. It is also presented the temperature distribution in Fig. 39d admitting the deformed configuration.

Since the viscoplasticity model is time sensitive, as the velocity increases, the stress state has a natural tendency to present higher stress concentration. Nonetheless, in compression with the previous casting velocity, 2.8 m/min, the out-of-plane stress component, in this current casting velocity, 3.2 m/min, decreases. This issue can be point out as a result of the initial casting temperature, once Ramberg-Osgood model also presented similar behavior. It is also evident, at the corner points, a considerable amount of compressive stress, as it is showed in Figs. 39a and 39b, such stress concentration, according to the Ramberg-Osgood model, can indicate the presence of off-corner crack formation.

Figure 38 – Thermal evolution during the casting velocity of 3.2 m/min at the primary cooling stage.

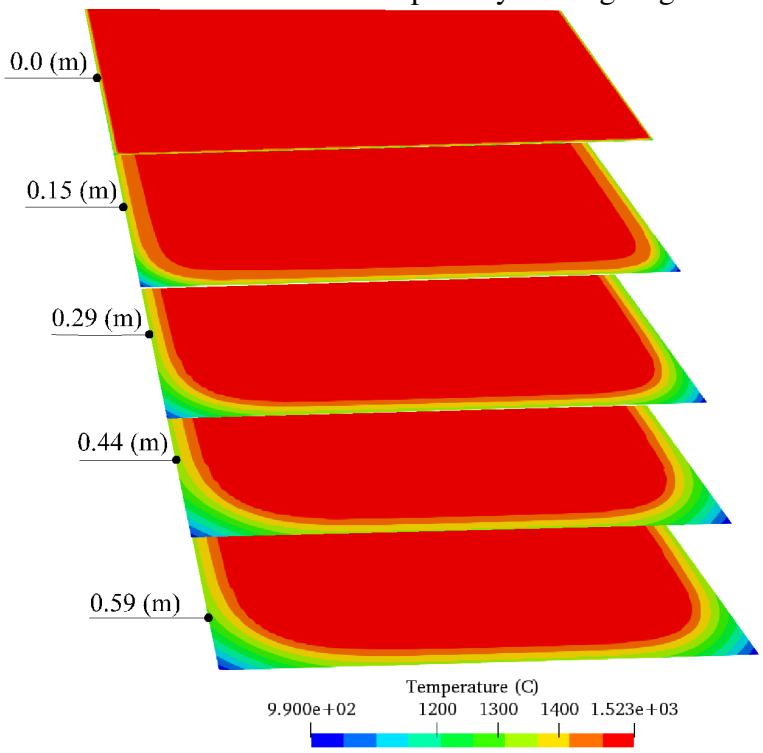

As it was observed in the previous casting simulations, one is able to notice a non-uniform stress distribution, Figs. 39 and 40, as well as a notable shrinkage of the strand. In particular, the stress components are shown for each corner point and inelastic model in Figs. 40a (Ramberg-Osgood with $K_p = 0$), 40b (Ramberg-Osgood with isotropic hardening), and 40c (Odqvist's viscoplastic law).

Following the same procedure presented in the previous section, the numerical solution provided the equivalent displacement, for each inelastic model, are compared in Fig. 41. From this observation, one is able to deduce that each inelastic approach provided similar results.

From Fig. 37 is clear that Ramberg-Osgood model assuming $K_p = 0$ was responsible to provide, among the compared models, the highest magnitude of equivalent displacement. Under the equivalent displacement viewpoint, in Fig. 41, the Odqvist's viscoplastic law is the model that assumes the result with the highest magnitude. In the context of stress concentration, the casting process with velocity of 3.2 m/min contributed with smaller levels of stress, as can be seem in Figs. 35, 36, 39, and 40.

Figure 39 – Stress state and temperature distribution at the mold exit. The out-of-plane stress profile assumes: a) Ramberg-Osgood model with both $K_p = 0$; and b) isotropic hardening ($K_p \neq 0$); c) Odqvist's viscoplastic law; and d) thermal distribution during the casting velocity of 3.2 m/min.

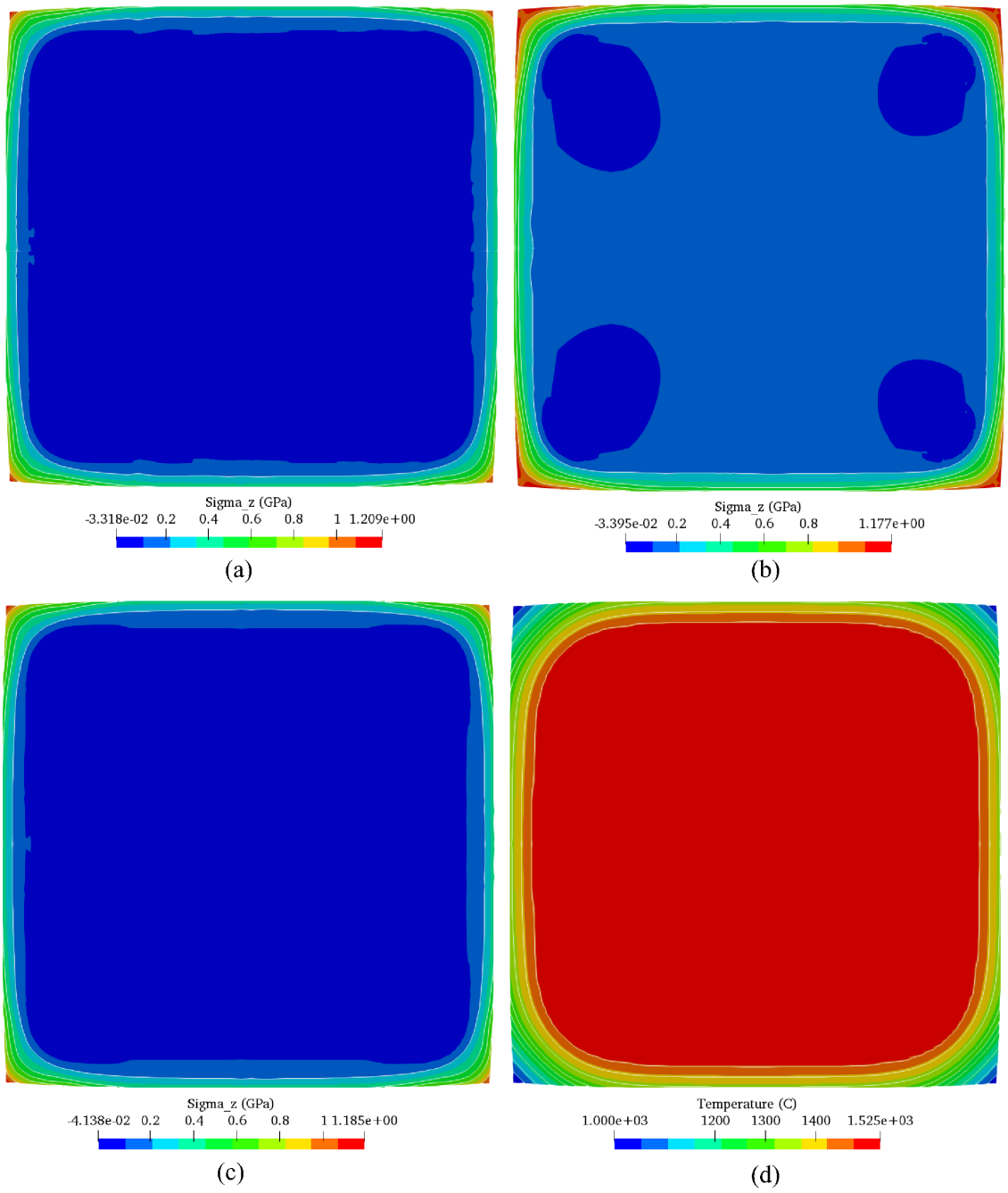

6.2 Thermomechanical profile of the continuous casting process

In this section an over all view of the cooling process is analyzed. In order to perform such task, six points at the strand's interfaced, as depicted in Fig. 7, were tracked as the solidification occurs during the entirely casting process.

Figure 40 – Stress components at corners. a) Ramberg-Osgood model with $K_p = 0$; b) Ramberg-Osgood model with isotropic hardening; and c) Odqvist's viscoplastic law.

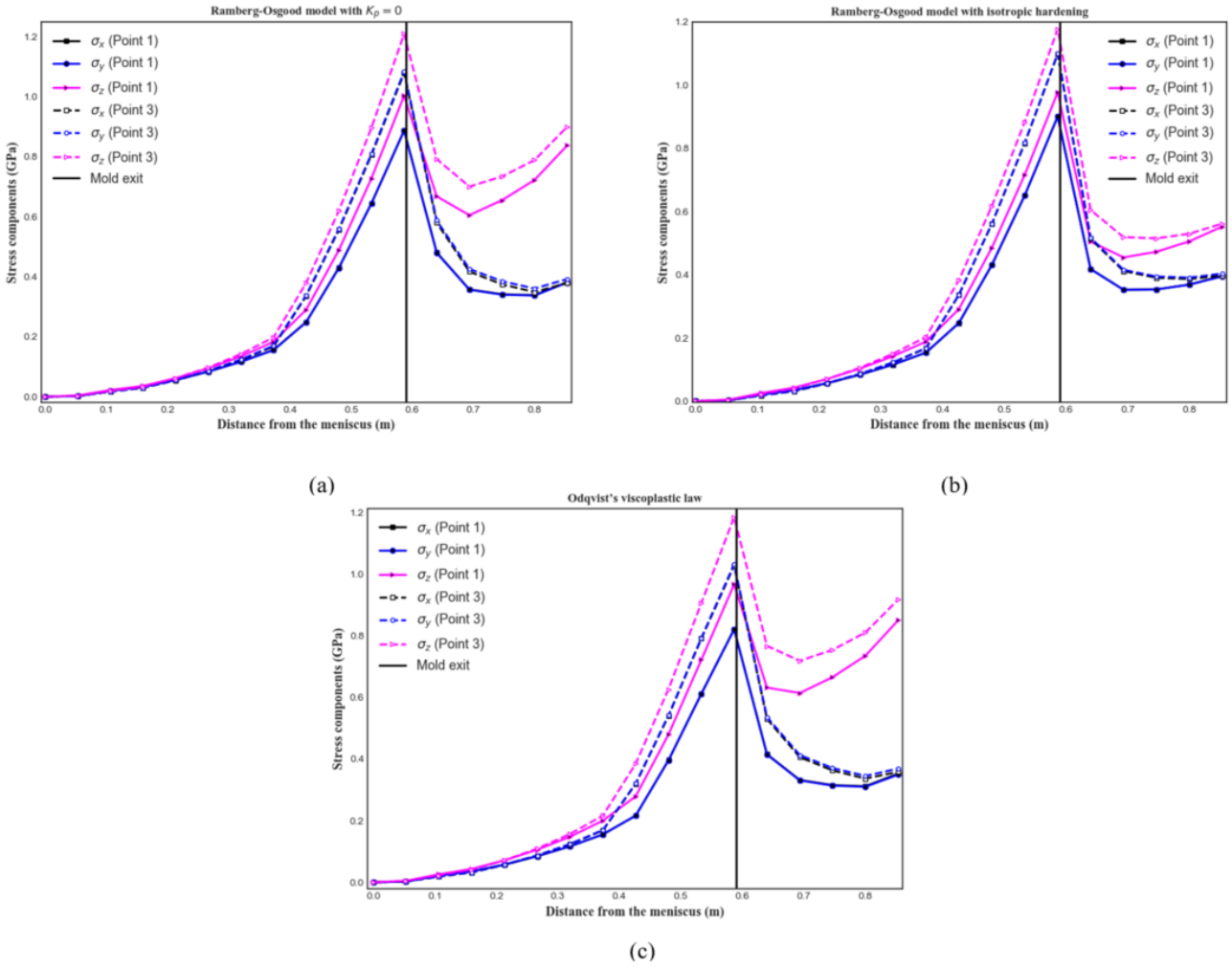

6.2.1 Existing cooling process

From the aforementioned points, the thermal behavior is presented in Figs. 42 and 43, for the casting velocities of 2.8 and 3.2 m/min, respectively.

In Figs. 42 and 43, the shell growth is delineated along the casting length. Special attention is given to the outlet of the mold, where the shell thickness, for the casting velocities of 2.8 and 3.2 m/min, present approximated values of 14 mm and 12 mm, respectively. These numerical predictions were more than enough to satisfy successfully the minimum shell thickness as it was described in the metallurgical criterion (see Section 2.6). Additionally, a small unsymmetrical temperature distribution throughout the first cooling zone was observed by the tracked points. Such behavior was expected since different heat transfer coefficients were imposed at each interface, unlike the secondary and tertiary cooling stages.

Also, from Figs. 42 and 43, the most pronounced reheating is at strand's corners

Figure 41 – Equivalent displacement at midpoint of the lateral face along the primary and secondary cooling. This numerical solution assumes the casting velocity of 3.2 m/min

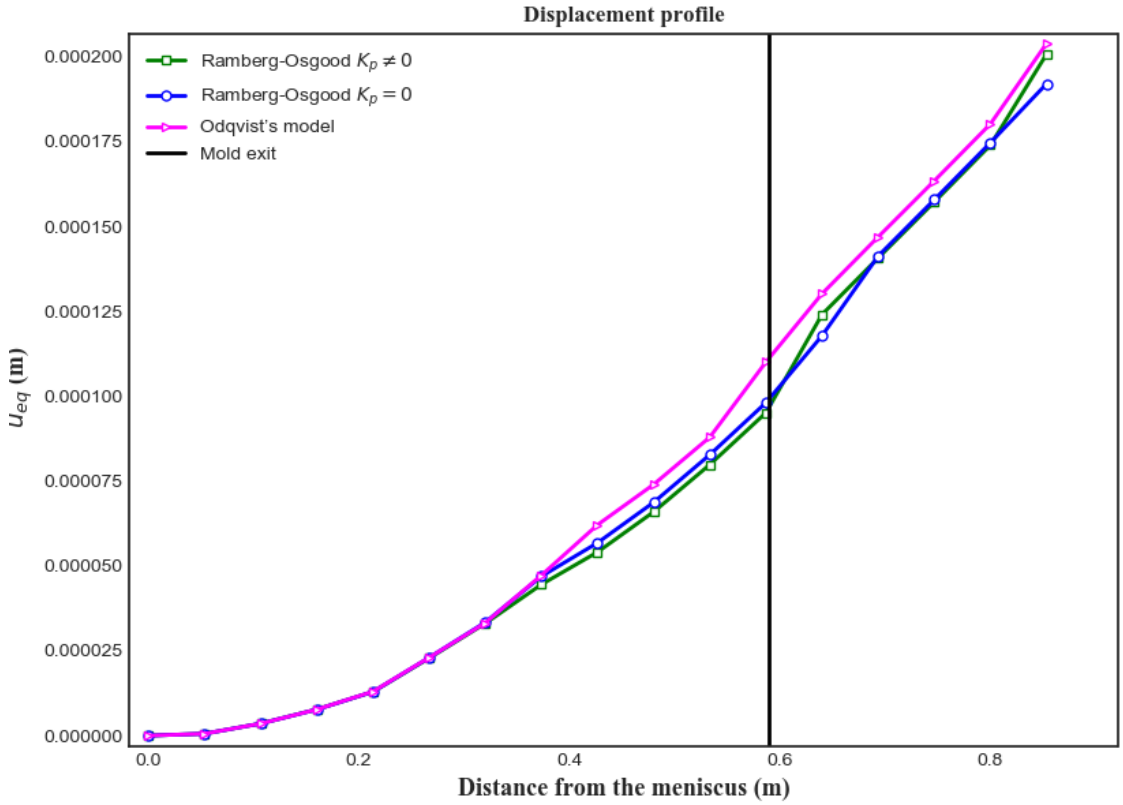

and it was observed when the cross section was in between the secondary and tertiary zones; more precisely, was verified reheating of 166 °C and 185 °C for the casting velocities of 2.8 and 3.2 m/min, respectively. On the other hand, at the interfaces, only the casting velocity of 2.8 m/min presented heating of 167 °C, which could lead to midway cracks formation, since the temperature of the face is within the high temperature zone. As discussed in Section 2.6, the maximum thermal variation length, according to the numerical simulations, has been violated for both casting velocities.

At the straightener, in Figs. 42 and 43, the numerical results predicted temperature greater than 1200 °C for the inner, outer, and lateral sides for both casting velocities. This surface temperature indicates that the strand's surface is into the low ductility zone and high level of compressive tensile stress during the contact of the ingot with the roles may lead to crack formation. Also, the casting velocity of 3.2 m/min presented solidification after the unbending point, which may lead to core cracks formation. Moreover, the stand is complete solidified before the cutoff point according to the simulations for both continuous casting velocities.

Figure 42 – Thermal profile for the casting velocity of 2.8 m/min along the casting machine.

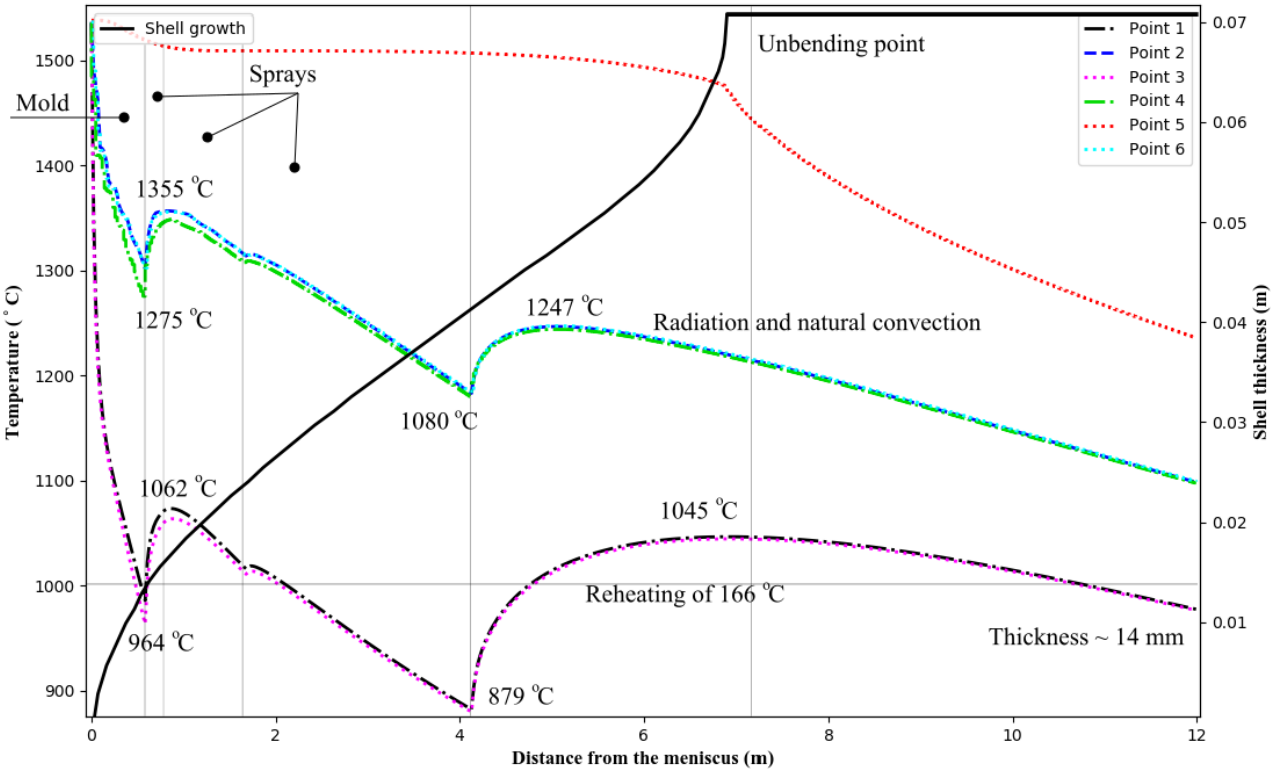

Figure 43 – Thermal profile for the casting velocity of 3.2 m/min along the casting machine.

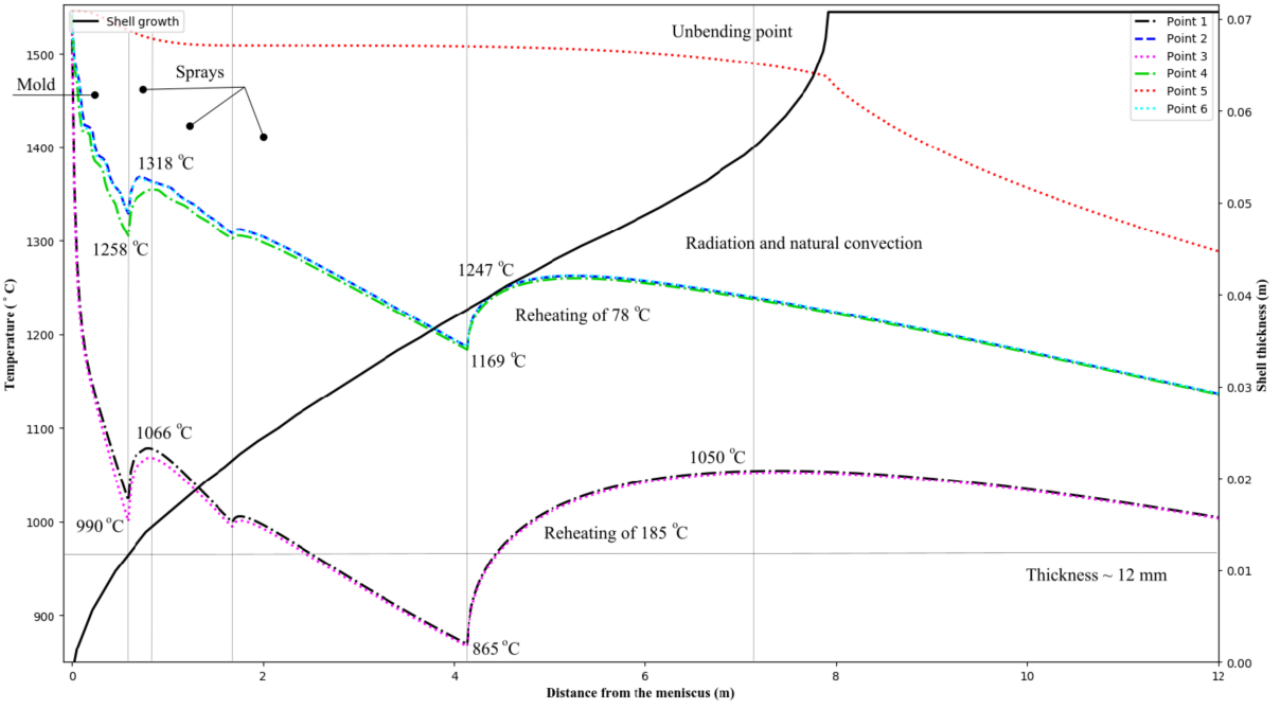

In order to verify the stress state due to the thermal variation, the two-dimensional representation is pictured in Figs. 44 and 45, assuming the first and the second casting operations, respectively. These illustrations present the temperature, in the deformed domain, and the out-of-plane stress component, in three casting positions ($z(t) = 2.0$ m, 4.11 m, and 12 m), for

each inelastic model employed.

Figure 44 – Temperature and out-of-plane stress distribution for the casting velocity of 2.8 m/min in three cooling sections.

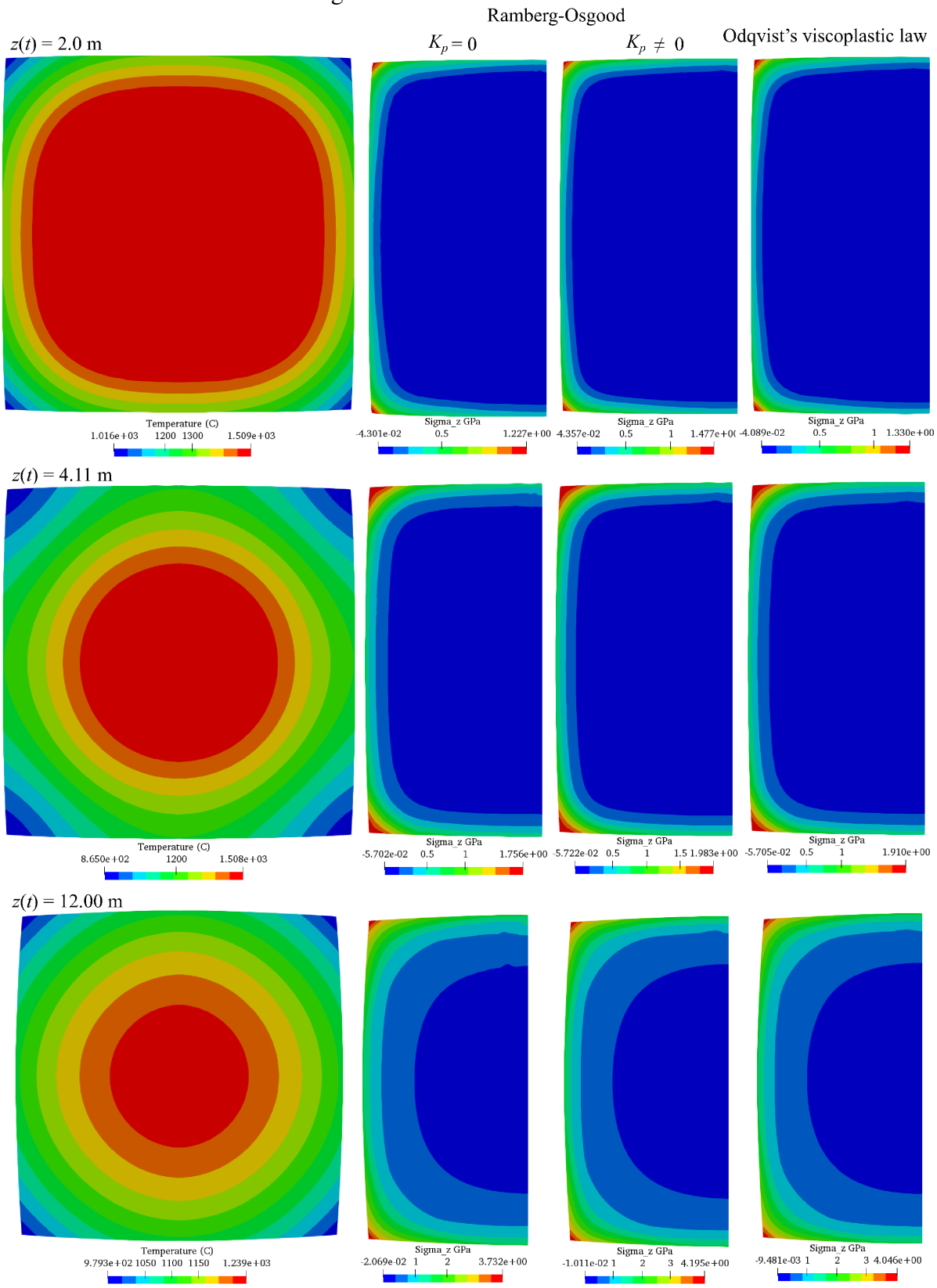

Figure 45 – Temperature and out-of-plane stress distribution for the casting velocity of 3.2 m/min in three cooling sections.

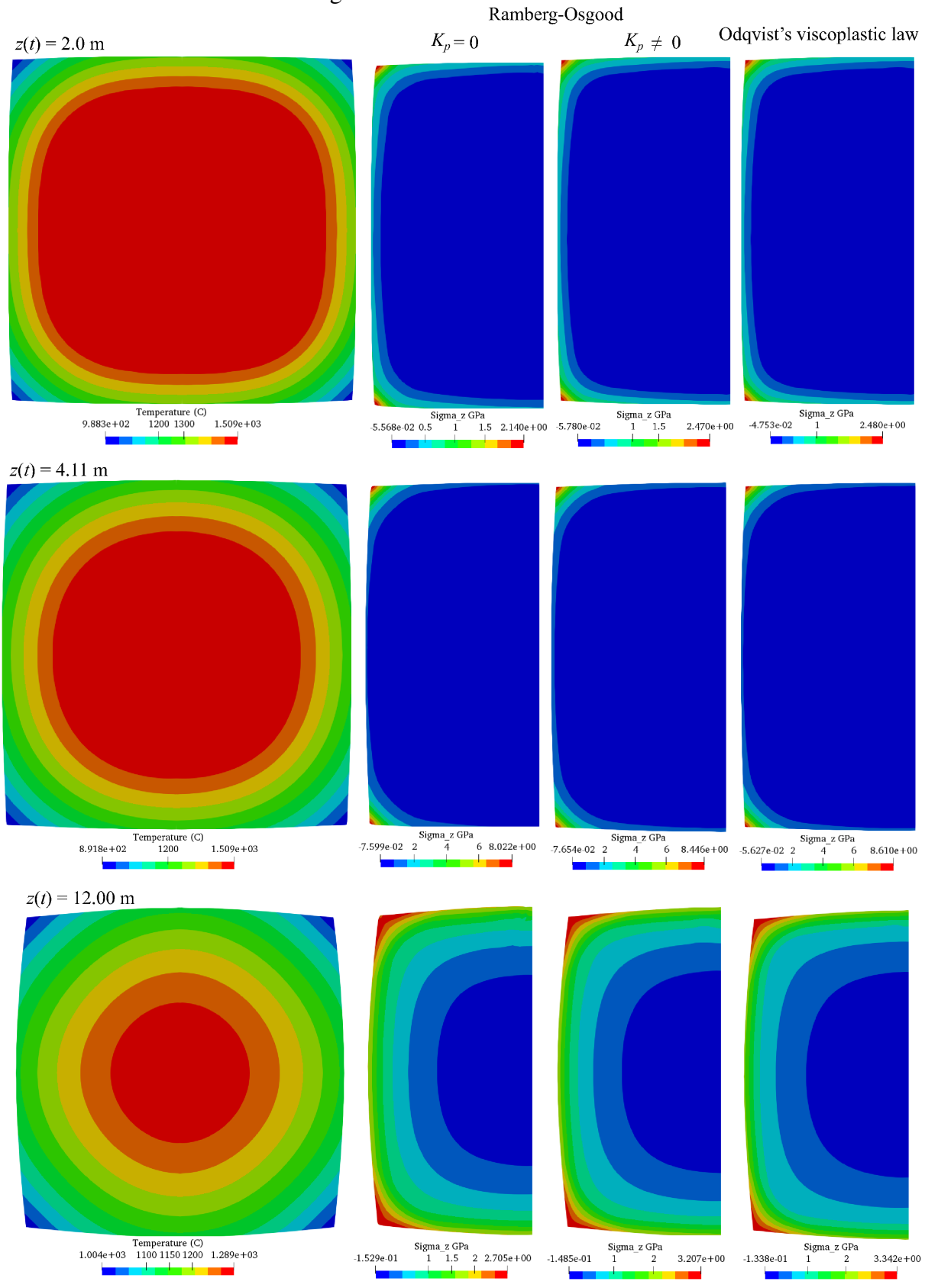

From Figs. 44 and 45, one can observe an evident increase of compressive tensile stress at the strand's corners. It is important to mention that the stress concentration at the casting position of $z(t) = 2.0$ m (sprays region) provided magnitudes approximately two times higher than at the mold outlet for both casting velocities (see Figs. 36 and 40). At the entrance of the tertiary stage, section position at $z(t) = 4.11$ m, the out-of-plane stress continued increasing until the cutoff point (casting position $z(t) = 12.00$ m). Moreover, the three models were able to present similar results. Another aspect that need to be pointed out is the considerable shrinkage of the ingot at the end of the casting machine, which indicates large deformation characteristics.

6.2.2 Modified cooling set in the sprays region

In order to enhance the cooling process, in the secondary zone, an additional spray section was added, as it was suggested in the work of Anjos (2013). The flow rate of water proposed for each section is presented in Table 7.

Table 7 – New suggested flow rates

	secondary cooling			
Velocity (m/min)	1st zone (l/s)	2nd zone (l/s)	3rd (l/s) zone	4th (l/s) zone
2.8	3.0	3.1	1.65	0.99
3.2	3.85	2.50	1.50	0.89

Moreover, since the thermal profile at mold region showed in Figs. 44 and 45 provide a very small unsymmetrical profile, the numerical results are given assuming just three points at the strand's interfaces instead of the six previous ones (for the sake of clarity). These numerical predictions are also compared with the previous cooling configuration, Figs. 46 and 47, discussed in the section above.

From the numerical predictions presented in Figs. 46 and 47, it is observed that the reheating at the strand's corners were 150 °C and 164 °C for the casting velocities of 2.8 and 3.2 m/min, respectively. Nevertheless, for the casting velocity of 3.2 m/min, this process happens in the low ductility zone. On the other hand, the reheating effect at each strand's face, for either casting velocities, were considerable low and equal to 50 °C and 58 °C for the casting velocities of 2.8 and 3.2 m/min, respectively. At unbending point, both casting velocities gave rise to temperature profiles in the ductility temperature range. Furthermore, the metallurgical length for both casting velocities were found before the unbending point. Although, the casting velocity

Figure 46 – Comparison of the modified thermal profiles with the previous results - casting velocity of 2.8 m/min.

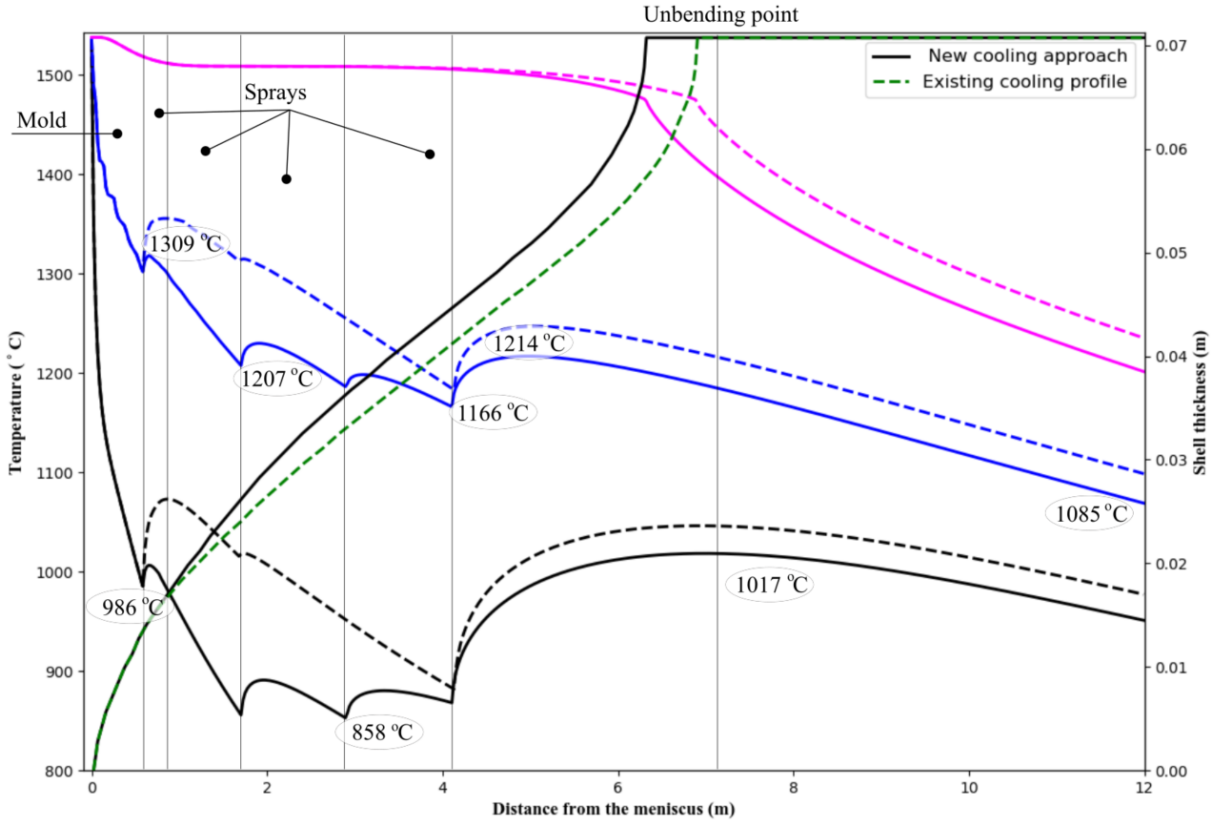

of 3.2 m/min presented strong tendency to crack formation at the corner due to the reheating amount, the overall results showed significant improvements in comparison with the first sprays configuration presented in the previous section.

At straightener or unbending point (Figs. 46 and 47), the numerical results predicted temperature into the ductility zone ($850\,^{\circ}C < T < 1200\,^{\circ}$C) for the inner, outer, and lateral sides for both casting velocities. This surface temperature indicates that the strand's surface is able to handle high level of stress during the contact of the ingot with the roles at straightener. Also, the casting velocity of 3.2 m/min presented solidification before the unbending point, which can avoid central crack formation.

The stress state that arises due to the thermal variation is showed in Figs. 48 and 49 from the point of view of the first and second casting operations, respectively. These two-dimensional view present the out-of-plane stress component and the thermal field in three casting position ($z(t)$ = 2.0 m, 4.11 m, and 12 m), for each inelastic model employed.

From Figs. 48 and 49, one can notice an evident increasing of the compressive tensile stress to the casting velocity of 2.8 m/min at the strand's corners compared to the previous cooling condition presented, in Figs. 44 and 45. Around the casting position of $z(t)$ = 2.0 m,

Figure 47 – Comparison of the modified thermal profiles with the previous results - casting velocity of 3.2 m/min.

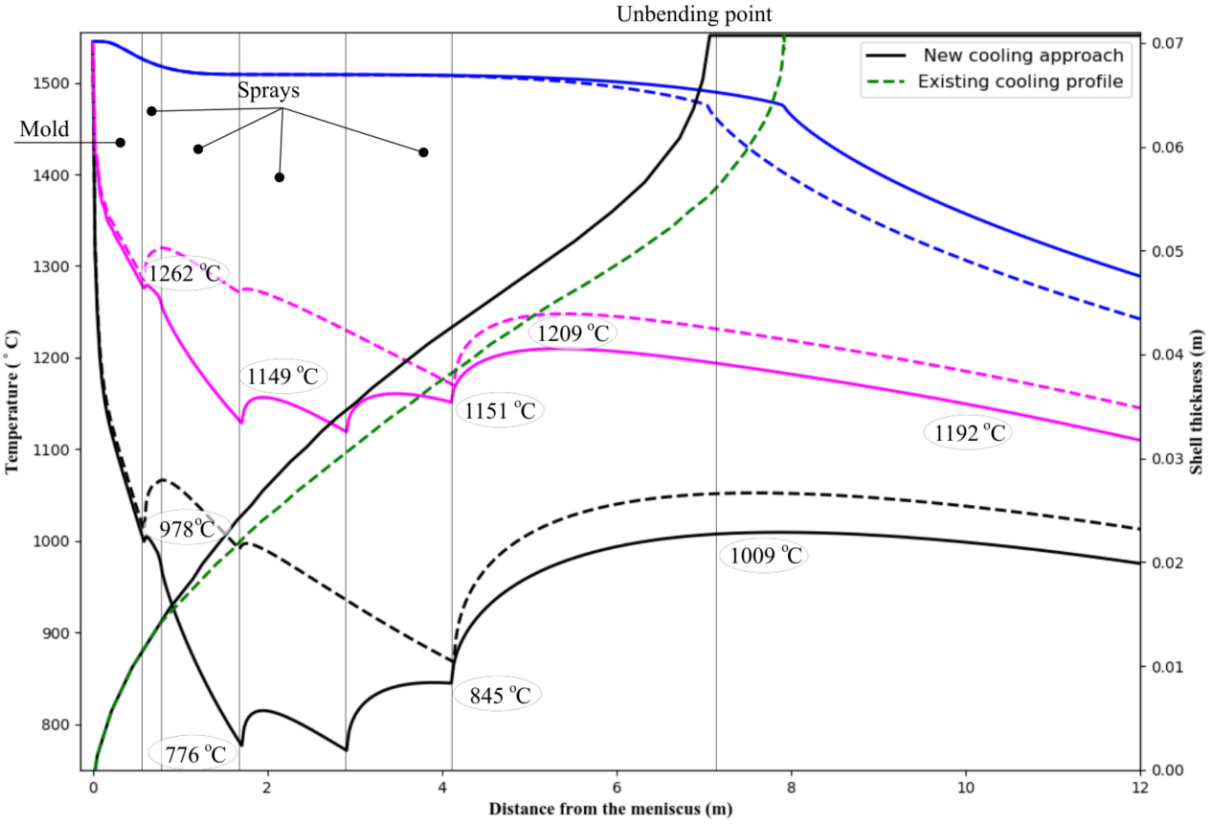

the stress concentration provided magnitudes approximately two times greater than the results given in the simulations of the previous cooling condition, for both casting velocities. However, at the position of $z(t)$ = 4.11 m, a considerable stress reduction is observed for the new cooling set associated to the casting velocity of 3.2 m/min.

It is important notice that the stress is concentrated mainly at the strand corners, in the new cooling set, in which, due to the geometry shape adopted, a severe cooling process is expected. A more realistic geometry presents a more rounder shape at the strand corners. In the cutoff section, casting position z(t) = 12.00 m, the aforementioned velocity presented a less concentrated stress, which can indicate that the new cooling process was able to provide a significant improvement. Finally, the three models employed were able to present similar results.

Figure 48 – Temperature and out-of-plane stress distribution, of the modified thermal profile, for the casting velocity of 2.8 m/min in three cooling casting sections.

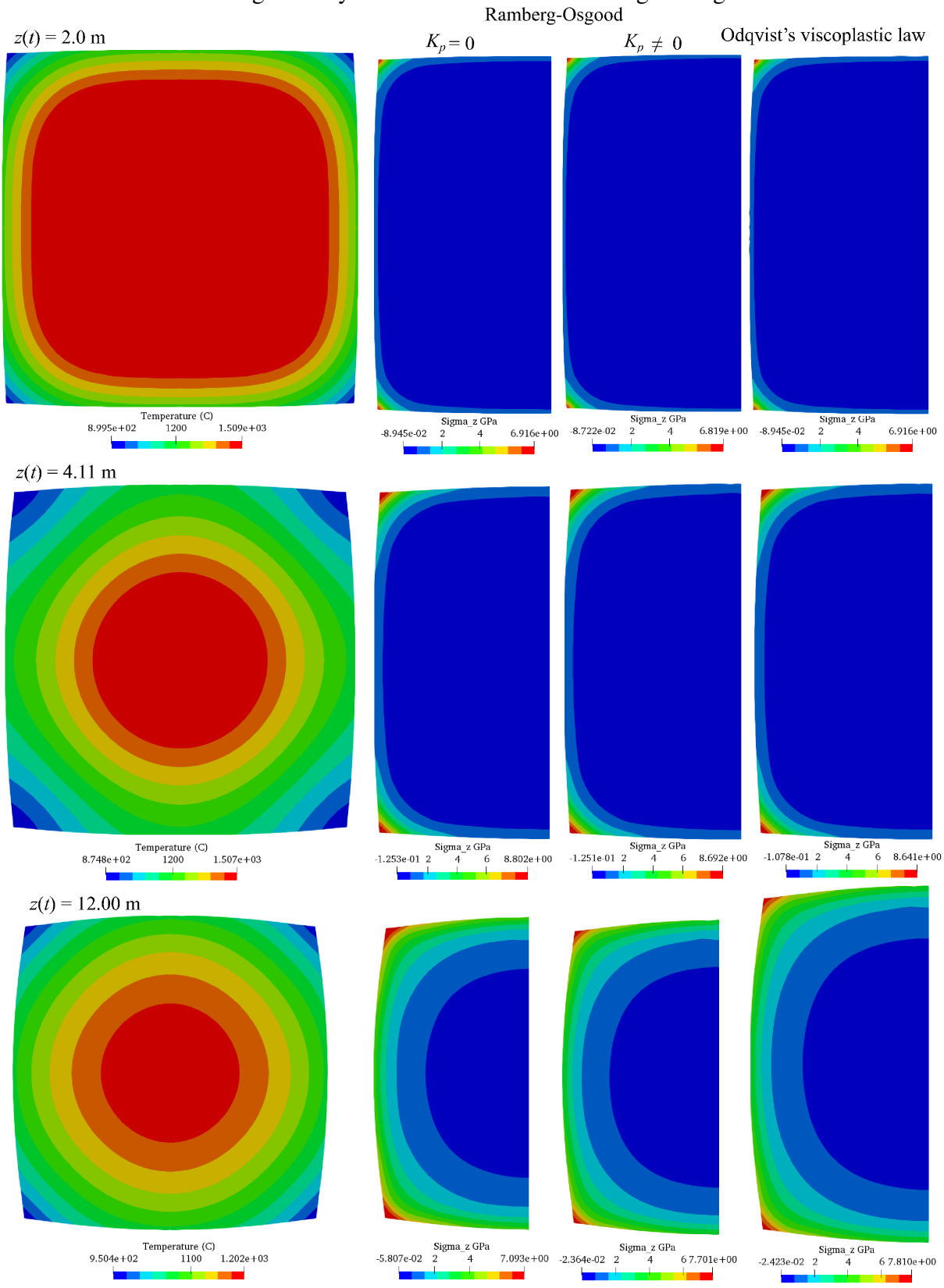

Figure 49 – Temperature and out-of-plane stress distribution, of the modified thermal profile, for the casting velocity of 3.2 m/min in three cooling casting sections.

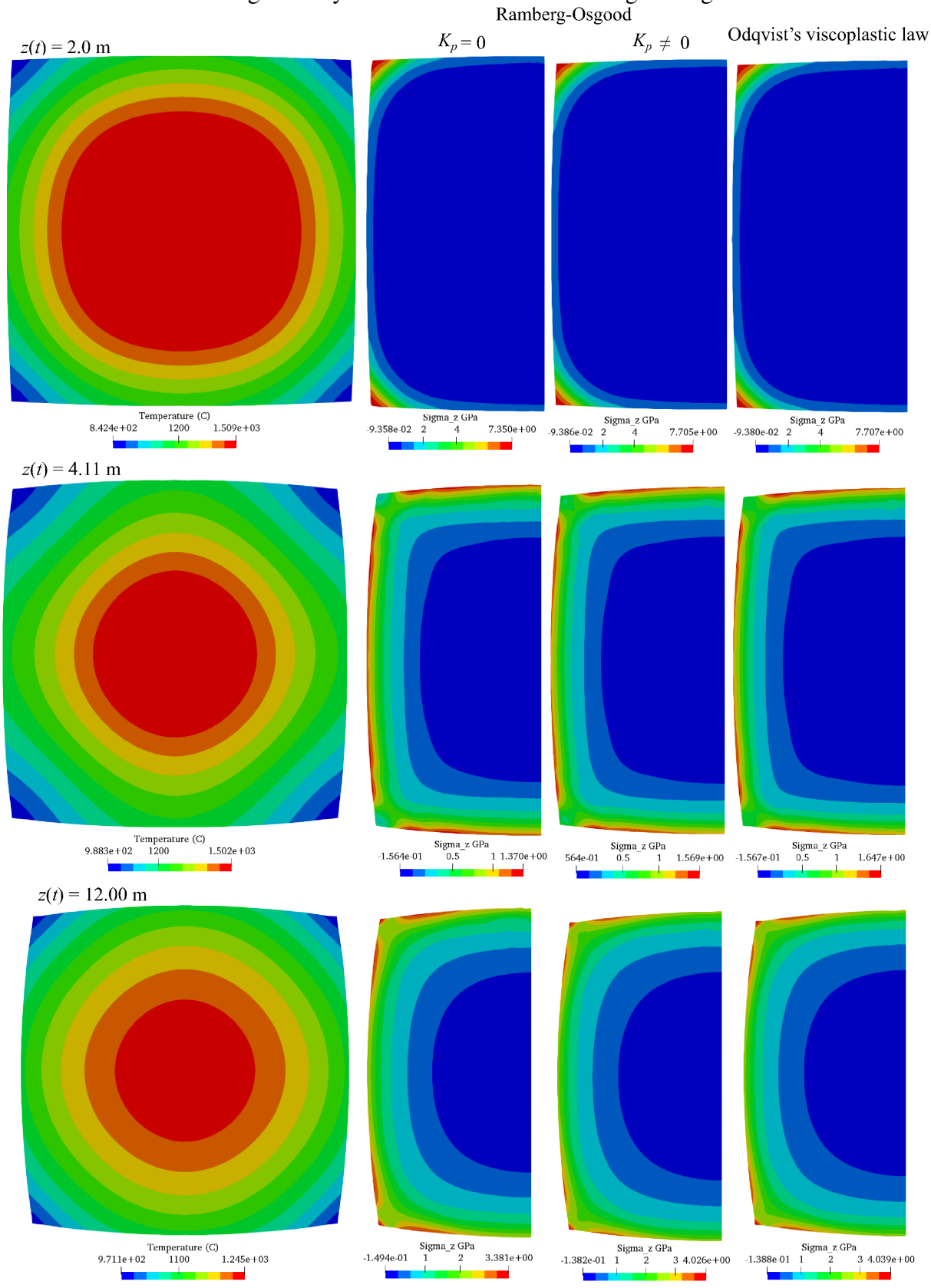

7 CONCLUSIONS

7.1 General conclusions

A two-dimensional thermal and mechanical analyzes using EbFVM has been presented and the models applied have been put in a suitable thermodynamic framework. Furthermore, based on this application, the following conclusions can be summarized:

1. The application of the EbFVM to linear and nonlinear materials (CSM) has demonstrated that EbFVM approach could handle problems in an efficient and accurate manner as it could be seen in Chapter 5.
2. The EbFVM numerical procedure was applied for the first time to analyze the dynamics of solidification process in the context of continuous casting. Numerical-experimental heat transfer coefficients were employed to study the cooling process as the strand's section passes through the casting machine. In addition, three inelastic models have been presented to simulate the thermomechanical behavior of a plain carbon steel. To improve the cooling process in the spray's zone, a new cooling spray configuration was proposed. The numerical results provided realistic behavior of the thermal profile. These results also pointed out that improvements in secondary zone could lead to significant improvement in order to avoid crack formation.
3. As it was noticed, the solidification of steel experience a great amount of strain rate, which is associated with the behavior of steel at elevates temperature. Such condition requires the inclusion of viscoplastic models. However, plastic models with linear isotropic hardening are widely used to model the continuous casting process, since they do not demand a complex computational implementation. When the viscoplastic and plastic models used in this work were compared, the results showed no significant difference between the models. Nonetheless, there are a large number of viscoplastic models and their results do not seem to agree. There is still a need for additional experimental data in order to allow accurate predictions of defects, such as crack formation (FALLAH *et al.*, 2000).
4. The proposed in-house simulator was implemented in Fortran in conjunction with Portable, Extensible Toolkit for Scientific Computation (PETSc) solver library. To linearize the equations, the Newton–Raphson procedure was applied.

7.2 Model limitations

In order to fully understand the physical aspects within the continuous casting technique, important features still have to be included in the simulator, as they are described bellow:

1. Function to estimate the size of the gap formation in the primary cooling stage;
2. The advection effect of the liquid pool, as well as the ferrostatic pressure of the liquid at solidified shell;
3. As it could be noticed, as the strand exits the casting machine, it sizes decreases significantly. Such behavior indicates that large deformations take place in such scenario, and therefore large instead of small deformations, as was considered in this work, should be considered;
4. A three-dimensional implementation can provide a more realistic thermal-mechanical behavior;
5. The inclusion of experimental measurements is essential to calibrate the simulator;
6. The inclusion of the mold in the simulator and insertion of the contact of the rolls with the strand's surface can provide a complete thermal-mechanical distribution view of the continuous casting process.

7.3 Future work

From the presented numerical model, several improvements still need to be made. As it was discussed in Section 7.2, to provide a complete understanding of the phenomenological aspects within the thermal-mechanical scenario during solidification, the inclusion of the listed points must be accomplished.

The inclusion of the Eulerian-Almansi finite strain tensor in the actual model could been seen as the most important insertion, since this approach allows a complete analyzes of the thermal-mechanical process. In the micro-structure level, during phase change, this approach is also able to provide the stress state of solid materials as the mechanical loads take place. Under this viewpoint, the simulator, aided by the flexibility of the EbFVM methodology, could be able to provide a more realistic behavior for different industrial applications. In addition, the incorporation of back-stress and generalized plane strain models could be made in conjunction with the aforementioned computational implementations.

Another important contribution is the introduction of level set method, which is sophisticated approach capable of track interfaces in different environments. This technique can be used to differentiate each emerged phase and track their evolution during the solidification as it happens. As for the investigation of crack formation, the introduction of damage and fracture models could be a differential.

It is important to mention that there is no fully developed simulator turned to the study of the solidification process in the continuous casting perspective. Furthermore, besides the simplification assumed in this simulator, it is still could be seen as important contribution not only to the study of the solidification during the continuous casting process, but also in the welding context.

BIBLIOGRAPHY

ANJOS, T. P. D. **Numerical-experimental methodology to determine the quality of steels obtained by continuous casting (In Portuguese)**. Dissertação (Mestrado) — Department of Engineering and Material Science. Federal University of Ceará, Fortaleza-CE, 2013.

ANJOS, T. P. D.; PIMENTA, P. V. C. L.; MARCONDES, F. Analysis of the heat transfer coefficients of the whole process of continuous casting of carbon steel. **Journal of the Brazilian Society of Mechanical Sciences and Engineering**, Springer, v. 40, n. 2, p. 107, 2018.

ASARO, R.; LUBARDA, V. **Mechanics of solids and materials**. [S.l.]: Cambridge University Press, 2006.

AVEDESIAN, M. M.; BAKER, H. *et al.* **ASM specialty handbook: magnesium and magnesium alloys**. [S.l.]: ASM international, 1999.

BAILEY, C.; CROSS, M. F. A finite volume procedure to solve elastic solid mechanics problems in three dimensions on an unstructured mesh. **International journal for numerical methods in engineering**, Wiley Online Library, v. 38, n. 10, p. 1757–1776, 1995.

BALIGA, B. R.; PATANKAR, S. V. A new finite-element formulation for convection-diffusion problems. **Numerical Heat Transfer**, Taylor & Francis, v. 3, n. 4, p. 393–409, 1980.

BARCELLOS, V. K. **Desenvolvimento de software de simulação da solidificação de aços no processo de lingotamento contínuo de tarugos. (Portuguese)**. Tese (Doutorado) — Universidade Federal do Rio Grande do Sul, Porto Alegre-RS, 2011.

BAUSE, M.; KNABNER, P. Computation of variably saturated subsurface flow by adaptive mixed hybrid finite element methods. **Advances in Water Resources**, Elsevier, v. 27, n. 6, p. 565–581, 2004.

BELLET, M.; HEINRICH, A. A two-dimensional finite element thermomechanical approach to a global stress-strain analysis of steel continuous casting. **ISIJ international**, The Iron and Steel Institute of Japan, v. 44, n. 10, p. 1686–1695, 2004.

BEZERRA, D. d. J. *et al.* **Two-dimensional numerical modeling of solidification process of Cartesian and cylindrical continuous casting geometries (In Portuguese)**. Tese (Doutorado) — Estate University of Campinas, Campinas-SP, 2016.

BEZERRA, D. de J. **Two dimensional modeling of solidification in the continuous casting process of Cartesian and cylindrical geometries (In Portuguese)**. Tese (Mechanical Engineering) — University of Campinas, Campinas - SP, 2016.

BILBAO, S.; HAMILTON, B. Wave-based room acoustics simulation: Explicit/implicit finite volume modeling of viscothermal losses and frequency-dependent boundaries. **Journal of the Audio Engineering Society**, Audio Engineering Society, v. 65, n. 1/2, p. 78–89, 2017.

BOLLE, E.; MOUREAU, J. C. Sprays cooling of hot surfaces: a description of the dispersed phase and a parametric study of heat transfer results. **Proceedings of Two Phase Flows and Heat Transfer**, NATO Advanced Study Institute, v. 101, p. 1327–1346, 1946.

BRIMACOMBE, J.; HAWBOLT, E.; WEINBERG, F. Metallurgical investigation of continuous casting billet moulds. **Progress Rep. for AISI, prepared at the University of BC**, 1980.

BRIMACOMBE, J.; SAMARASEKERA, I.; BOMMARAJU, R. Optimum design and operation of moulds for the continuous casting of steel billets. In: **Steelmaking Proceedings.** [S.l.: s.n.], 1986. v. 69, p. 409–423.

BRIMACOMBE, J.; SORIMACHI, K. Crack formation in the continuous casting of steel. **Metallurgical transactions B**, Springer, v. 8, n. 2, p. 489–505, 1977.

BRIMACOMBE, J. K. Design of continuous casting machines based on a heat-flow analysis: state-of-the-art review. **Canadian Metallurgical Quarterly**, Taylor & Francis, v. 15, n. 2, p. 163–175, 1976.

BRIMACOMBE, J. K.; SAMARASEKERA, I. V.; LAIT, J. E. **Continuous casting: heat flow, solidification and crack formation**. [S.l.]: Iron & Steel Society, 1984. v. 2.

BUSCHOW, K. J.; CAHN, R. W.; FLEMINGS, M. C.; ILSCHNER, B.; KRAMER, E. J.; MAHAJAN, S. Encyclopedia of materials. **Science and technology**, v. 1, p. 11, 2001.

CALLISTER, W. D.; RETHWISCH, D. G. **Materials science and engineering**. [S.l.]: John Wiley & Sons NY, 2011. v. 5.

CARSLAW, H. S.; JAEGER, J. C. **Conduction of heat in solids: Oxford Science Publications**. [S.l.]: Oxford, England, 1959.

CHAUDHURI, S.; SINGH, R. K.; PATWARI, K.; MAJUMDAR, S.; RAY, A. K.; SINGH, A. K. P.; NEOGI, N. Design and implementation of an automated secondary cooling system for the continuous casting of billets. **ISA transactions**, Elsevier, v. 49, n. 1, p. 121–129, 2010.

CHEN, W.; ZHANG, Y. Z.; ZHANG, C. J.; ZHU, L. G.; LU, W. G.; WANG, B. X.; MA, J. H. Thermo-mechanical simulation and parameters optimization for beam blank continuous casting. **Materials Science and Engineering: A**, Elsevier, v. 499, n. 1-2, p. 58–63, 2009.

CHEUNG, N. **Interaction between a knowledge-base and a mathematical model of solidification to the quality analysis of continuous casting of steels (In Portuguese)**. Dissertação (Mestrado) — University of Campinas, Campinas - SP, 1999.

CRISFIELD, M. A.; REMMERS, J. J. C.; VERHOOSEL, C. V. *et al.* **Nonlinear finite element analysis of solids and structures**. [S.l.]: John Wiley & Sons, 2012.

DEMIRDŽIĆ, I.; MARTINOVIĆ, D. Finite volume method for thermo-elasto-plastic stress analysis. **Computer methods in applied mechanics and engineering**, Elsevier, v. 109, n. 3-4, p. 331–349, 1993.

DEMIRDŽIĆ, I.; MUZAFERIJA, S. Finite volume method for stress analysis in complex domains. **International Journal for Numerical Methods in Engineering**, Wiley Online Library, v. 37, n. 21, p. 3751–3766, 1994.

DU, F.; WANG, X.; FU, J.; HAN, X.; XU, J.; YAO, M. Inverse problem-based analysis on non-uniform thermo-mechanical behaviors of slab during continuous casting. **The International Journal of Advanced Manufacturing Technology**, Springer, v. 94, n. 1-4, p. 1189–1196, 2018.

DU, F.; WANG, X.; HAN, X.; XU, J.; YAO, M. Analysis of non-uniform thermal behaviour of special steel during slab continuous casting. **Ironmaking & Steelmaking**, Taylor & Francis, v. 45, n. 4, p. 350–355, 2018.

DUNNE, F.; PETRINIC, N. **Introduction to computational plasticity**. [S.l.]: Oxford University Press on Demand, 2005.

DVORKIN, E.; CANGA, M. Thermomechanical behavior of the mold in siderca continuous casting machine cc3. case of φ 295 mm and carbon steel 042. **Reporte Técnico I 1.20/190-90, CINI**, 1990.

ERICSON, L. Cracking in low-alloy al-grain refined steels. **Scandinavian Journal of Metallurgy**, v. 6, n. 3, p. 116–124, 1977.

FACHINOTTI, V. D.; CARDONA, A. Constitutive models of steel under continuous casting conditions. **Journal of Materials Processing Technology**, Elsevier, v. 135, n. 1, p. 30–43, 2003.

FALLAH, N. A.; BAILEY, C.; CROSS, M.; TAYLOR, G. A. Comparison of finite element and finite volume methods application in geometrically nonlinear stress analysis. **Applied Mathematical Modelling**, Elsevier, v. 24, n. 7, p. 439–455, 2000.

FERNANDES, B. R. B. **Implicit and Semi-Implicit Techniques for the Compositional Petroleum Reservoir Simulation based on Volume Balance**. Dissertação (Mestrado) — Federal University of Ceará, Fortaleza-CE, 2014.

FERNANDES, B. R. B.; LIMA, I. d.; FILHO, E. P. D.; OLIVEIRA, J. C. B. de; MARCONDES, F.; SEPEHRNOORI, K. A tvd scheme for 3d unstructured grids applied to compositional reservoir simulation. **Brazilian Journal of Chemical Engineering**, SciELO Brasil, v. 34, n. 4, p. 1161–1174, 2017.

FERNANDES, B. R. B.; MARCONDES, F.; SEPEHRNOORI, K. Investigation of several interpolation functions for unstructured meshes in conjunction with compositional reservoir simulation. **Numerical Heat Transfer, Part A: Applications**, Taylor & Francis, v. 64, n. 12, p. 974–993, 2013.

FILIPPINI, G.; MALISKA, C. R.; VAZ, M. A physical perspective of the element-based finite volume method and fem-galerkin methods within the framework of the space of finite elements. **International Journal for Numerical Methods in Engineering**, Wiley Online Library, v. 98, n. 1, p. 24–43, 2014.

FORSYTH, P. A.; KROPINSKI, M. C. Monotonicity considerations for saturated–unsaturated subsurface flow. **SIAM Journal on Scientific Computing**, SIAM, v. 18, n. 5, p. 1328–1354, 1997.

FRYER, Y. D.; BAILEY, C.; CROSS, M.; LAI, C.-H. A control volume procedure for solving the elastic stress-strain equations on an unstructured mesh. **Applied mathematical modelling**, Elsevier, v. 15, n. 11-12, p. 639–645, 1991.

GARCIA, A.; SPIM, J. A.; SANTOS, C. A.; CHEUNG, N. Continuous casting of steel (in portuguese). **Associação Brasileira de Metalurgia, São Paulo - SP: ISBN 85-7737-005-4**, 2006.

GE, S.; ISAC, M.; GUTHRIE, R. I. L. Progress in strip casting technologies for steel; technical developments. **ISIJ international**, The Iron and Steel Institute of Japan, v. 53, n. 5, p. 729–742, 2013.

GRILL, A.; BRIMACOMBE, J.; WEINBERG, F. Mathematical analysis of stresses in continuous casting of steel. **Ironmaking Steelmaking**, v. 3, n. 1, p. 38–47, 1976.

GURTIN, M. E.; FRIED, E.; ANAND, L. **The mechanics and thermodynamics of continua**. [S.l.]: Cambridge University Press, 2010.

HARDIN, R. A.; LIU, K.; BECKERMANN, C.; KAPOOR, A. A transient simulation and dynamic spray cooling control model for continuous steel casting. **Metallurgical and materials transactions B**, Springer, v. 34, n. 3, p. 297–306, 2003.

HARSTE, K.; JABLONKA, A.; SCHWERDTFEGER, K. 4th int. conf. continuous casting, brussels, belgium. Verlag Stahleisen Dusseldorf, 1988.

HUESPE, A. E.; CARDONA, A.; FACHINOTTI, V. Thermomechanical model of a continuous casting process. **Computer methods in applied mechanics and engineering**, Elsevier, v. 182, n. 3-4, p. 439–455, 2000.

HULL, D.; BACON, D. J. **Introduction to dislocations**. [S.l.]: Butterworth-Heinemann, 2001.

INOUE, T. Metallo-thermo-mechanical coupling. application to the analysis of quenching, welding and continuous casting processes. **Berg Huttenmann. Monatsh.**, v. 132, n. 3, p. 63–71, 1987.

JABLONKA, A.; HARSTE, K.; SCHWERDTFEGER, K. Thermomechanical properties of iron and iron-carbon alloys: density and thermal contraction. **Steel research**, Wiley Online Library, v. 62, n. 1, p. 24–33, 1991.

JASAK, H.; WELLER, H. G. Application of the finite volume method and unstructured meshes to linear elasticity. **International journal for numerical methods in engineering**, v. 48, n. 2, p. 267–287, 2000.

JIMBO, I.; CRAMB, A. The density of liquid iron-carbon alloys. **Metallurgical Transactions B**, Springer, v. 24, n. 1, p. 5–10, 1993.

KELLY, J. E.; MICHALEK, K. P.; O'CONNOR, T. G.; THOMAS, B. G.; DANTZIG, J. A. Initial development of thermal and stress fields in continuously cast steel billets. **Metallurgical Transactions A**, Springer, v. 19, n. 10, p. 2589–2602, 1988.

KHAN, A. Q. **The effect of morphology on the strength of copper-based martensites**. Tese (Doutorado) — University of Leuven, Belgium, 1972.

KIM, N.-H. **Introduction to nonlinear finite element analysis**. [S.l.]: Springer Science & Business Media, 2014.

KORIC, S. **Efficient thermo-mechanical model for solidification processes and its applications in steel continuous casting**. Tese (Doutorado) — University of Illinois at Urbana-Champaign, 2006.

KORIC, S.; THOMAS, B. G. Thermo-mechanical model of solidification processes with abaqus. In: **ABAQUS Users Conference**. [S.l.: s.n.], 2007. p. 320–336.

KORIC, S.; THOMAS, B. G. Thermo-mechanical models of steel solidification based on two elastic visco-plastic constitutive laws. **journal of materials processing technology**, Elsevier, v. 197, n. 1-3, p. 408–418, 2008.

KULKARNI, M. S.; BABU, A. S. Managing quality in continuous casting process using product quality model and simulated annealing. **Journal of Materials Processing Technology**, Elsevier, v. 166, n. 2, p. 294–306, 2005.

KUMAR, S. **An expert system to diagnose quality problems in the continuous casting of steel billets**. Tese (Doutorado) — University of British Columbia, 1991.

LEE, S. State of the art technology in slab continuous casting. **BHM Berg-und Hüttenmännische Monatshefte**, Springer, v. 163, n. 1, p. 3–10, 2018.

LEMAITRE, J.; CHABOCHE, J.-L. **Mechanics of solid materials**. [S.l.]: Cambridge university press, 1994.

LEWIS, R.; MORGAN, K.; ROBERTS, P. Determination of thermal stresses in solidification problems. **Numerical analysis of forming processes**, Wiley New York, p. 405–431, 1984.

LI, C.; THOMAS, B. G. Thermomechanical finite-element model of shell behavior in continuous casting of steel. **Metallurgical and MAterials transactions B**, Springer, v. 35, n. 6, p. 1151–1172, 2004.

LI, C. S.; THOMAS, B. G. Thermo-mechanical finite element model of shell behavior in the continuous casting of steel. **Key Engineering Materials**, Trans Tech Publ, 2003.

LOGAN, D. First course in finite element analysis. **Brooks/Cole**, 2002.

LUBLINER, J. **Plasticity theory**. [S.l.]: Courier Corporation, 2008.

LUO, X.; CHEN, Y.; SHEN, H. Thermomechanical behavior in continuous bloom casting with different mold tapers. **Tsinghua Science and Technology**, TUP, v. 13, n. 5, p. 598–604, 2008.

MALISKA, C. R. **Heat Transfer and Computational Fluid Mechanics (In Portuguese)**. [S.l.]: LTC Editora, Rio de Janeiro, 2004.

MARCONDES, F.; SEPEHRNOORI, K. An element-based finite-volume method approach for heterogeneous and anisotropic compositional reservoir simulation. **Journal of Petroleum Science and Engineering**, Elsevier, v. 73, n. 1, p. 99–106, 2010.

MAZUMDAR, S.; RAY, S. K. Solidification control in continuous casting of steel. **Sadhana**, Springer, v. 26, n. 1-2, p. 179–198, 2001.

MOCZO, P.; ROBERTSSON, J. O. A.; EISNER, L. The finite-difference time-domain method for modeling of seismic wave propagation. **Advances in Geophysics**, Elsevier, v. 48, p. 421–516, 2007.

MORO, L.; NOVAK, J. S.; BENASCIUTTI, D.; BONA, F. D. Thermal distortion in copper moulds for continuous casting of steel: numerical study on creep and plasticity effect. **Ironmaking & Steelmaking**, Taylor & Francis, p. 1–7, 2017.

NETO, E. A. S.; PERIC, D.; OWEN, D. R. J. **Computational methods for plasticity: theory and applications**. [S.l.]: John Wiley & Sons, 2011.

OKUNO, K.; NARUWA, H.; KURIBAYASHI, T.; TAKAMOTO, T. Dynamic spray cooling control system for continuous casting. **Iron Steel Eng.**, v. 64, n. 4, p. 34–38, 1987.

PATANKAR, S. V. Numerical heat transfer and fluid flow: Computational methods in mechanics and thermal science. Hemisphere Publishing Corp., v. 1, 1980.

PETRUS, B.; ZHENG, K.; ZHOU, X.; THOMAS, B. G.; BENTSMAN, J. Real-time, model-based spray-cooling control system for steel continuous casting. **Metallurgical and materials transactions B**, Springer, v. 42, n. 1, p. 87–103, 2011.

PIMENTA, P. V. C. L. **Thermomechanical simulation of the continuous casting process using the Element based Finite Volume Method (In Portuguese)**. Dissertação (Mestrado) — Department of Engineering and Material Science. Federal University of Ceará, Fortaleza-CE, 2014.

PIMENTA, P. V. C. L.; MARCONDES, F. Two-dimensional rate-independent plasticity using the element-based finite volume method. **Journal of the Brazilian Society of Mechanical Sciences and Engineering**, Springer, v. 41, n. 3, p. 142, 2019.

RAY, A. K.; RAY, S. K.; BASU, D. S.; MAZUMDAR, S. Continuous casting: A review. **Steel India**, v. 26, n. 3, p. 138–154, 2004.

ROCHA, J. R. S. **Modeling and numerical simulation of fluid flow and heat transfer of a steel continuous casting tundish**. Dissertação (Mestrado) — Department of Engineering and Material Science. Federal University of Ceará, Fortaleza-CE, 2017.

RODRIGUEZ, N.; DAVEY, K.; FEIJOO, J. V.; JUAREZ-HERNANDEZ, A. Numerical modelling of unsteady convective–diffusive heat transfer with a control volume hybrid method. **Applied Mathematical Modelling**, Elsevier, v. 33, n. 2, p. 897–923, 2009.

RYSKIN, G.; LEAL, L. G. Numerical solution of free-boundary problems in fluid mechanics. part 1. the finite-difference technique. **Journal of Fluid Mechanics**, Cambridge University Press, v. 148, p. 1–17, 1984.

SANTAOJA, K. Gradient theory from the thermomechanics point of view. **Engineering fracture mechanics**, Elsevier, v. 71, n. 4-6, p. 557–566, 2004.

SANTOS, C.; SPIM, J.; GARCIA, A. Mathematical modeling and optimization strategies (genetic algorithm and knowledge base) applied to the continuous casting of steel. **Engineering applications of artificial intelligence**, Elsevier, v. 16, n. 5-6, p. 511–527, 2003.

SCHNEIDER, G. E.; ZEDAN, M. Control-volume-based finite element formulation of the heat conduction equation. **Spacecraft Thermal Control, Design, and Operation, Progress in Astronautics and Aeronautics**, v. 86, p. 305–327, 1983.

SILVA, F. D. A. **Quality optimization in continuous casting of Billets through use of mathematical models (In Portuguese)**. Dissertação (Mestrado) — Federal University of Pernambuco, Recife-PE, 2016.

SIVARAMAKRISHNAN, S.; BAI, H.; THOMAS, B.; VANKA, P.; DAUBY, P.; ASSAR, M. Transient flow structures in continuous casting of steels. In: **59th Ironmaking Conference, Pittsburgh, P A, Iron and Steel Society, Warrendale, P A**. [S.l.: s.n.], 2000. v. 59, p. 541–557.

SLADEK, J.; SLADEK, V.; MARKECHOVA, I. Boundary element method analysis of stationary thermoelasticity problems in non-homogeneous media. **International Journal for Numerical Methods in Engineering**, Wiley Online Library, v. 30, n. 3, p. 505–516, 1990.

SLONE, A. K.; BAILEY, C.; CROSS, M. Dynamic solid mechanics using finite volume methods. **Applied mathematical modelling**, Elsevier, v. 27, n. 2, p. 69–87, 2003.

SOEYANTO, K. **Improvement of surface quality of continuously cast steel control of cast structure and straightening temperature**. Tese (Doutorado) — University of Wollongong, 1995.

SOPHER, R. Effects of chemical composition on cracking resistance of high-strength-steel weld metals. **Welding lournal**, v. 37, n. 11, 1958.

SPUY, D. D. Van der; CRAIG, I. K.; PISTORIUS, P. C. An optimization procedure for the secondary cooling zone of a continuous billet caster. **Journal of the South African Institute of Mining and Metallurgy**, SOUTH AFRICAN INST MIN METALL PO BOX 61127 11-13 MACLAREN ST 13TH FLOOR-CAPE TOWERS, MARSHALLTOWN TRANSVAAL 2107, SOUTH AFRICA, v. 99, n. 1, p. 49–54, 1999.

SRIVASTAVA, R.; YEH, T.-C. J. A three-dimensional numerical model for water flow and transport of chemically reactive solute through porous media under variably saturated conditions. **Advances in water resources**, Elsevier, v. 15, n. 5, p. 275–287, 1992.

SULIMAN, R.; OXTOBY, O. F.; MALAN, A. G.; KOK, S. An enhanced finite volume method to model 2d linear elastic structures. **Applied Mathematical Modelling**, Elsevier, v. 38, n. 7, p. 2265–2279, 2014.

TAYLOR, G. A.; BAILEY, C.; CROSS, M. Solution of the elastic/visco-plastic constitutive equations: a finite volume approach. **Applied mathematical modelling**, Elsevier, v. 19, n. 12, p. 746–760, 1995.

TAYLOR, G. A.; BAILEY, C.; CROSS, M. A vertex-based finite volume method applied to non-linear material problems in computational solid mechanics. **International Journal of Numerical Methods in Engineering**, v. 56, n. 4, p. 507–529, 2003.

THOMAS, B.; SAMARASEKERA, I.; BRIMACOMBE, J. Mathematical model of the thermal processing of steel ingots: Part ii. stress model. **Metallurgical transactions B**, Springer, v. 18, n. 1, p. 131, 1987.

THOMAS, B. G. Modeling of the continuous casting of steel—past, present, and future. **Metallurgical and materials transactions B**, Springer, v. 33, n. 6, p. 795–812, 2002.

THOMAS, B. G. Review on modeling and simulation of continuous casting. **steel research international**, Wiley Online Library, v. 89, n. 1, p. 1700312, 2018.

THOMAS, B. G.; BRIMACOMBE, J. K.; SAMARASEKERA, I. V. The formation of panel cracks in steel ingots: a state-of-the-art review. **ISS transactions**, v. 7, n. 10, p. 7–20, 1986.

TIADEN, J. Phase field simulations of the peritectic solidification of fe–c. **Journal of crystal Growth**, Elsevier, v. 198, p. 1275–1280, 1999.

TSZENG, T.; KOBAYASHI, S. Stress analysis in solidification processes: application to continuous casting. **International Journal of Machine Tools and Manufacture**, Elsevier, v. 29, n. 1, p. 121–140, 1989.

VERZICCO, R.; ORLANDI, P. A finite-difference scheme for three-dimensional incompressible flows in cylindrical coordinates. **Journal of Computational Physics**, Elsevier, v. 123, n. 2, p. 402–414, 1996.

VOLLER, V.; CROSS, M. Accurate solutions of moving boundary problems using the enthalpy method. **International journal of heat and mass transfer**, Elsevier, v. 24, n. 3, p. 545–556, 1981.

VOLLER, V. R. **Basic control volume finite element methods for fluids and solids**. [S.l.]: World Scientific, 2009. v. 1.

WANG, X.; KONG, L.; DU, F.; YAO, M.; ZHANG, X.; MA, H.; WANG, Z. Mathematical modeling of thermal resistances of mold flux and air gap in continuous casting mold based on an inverse problem. **ISIJ International**, The Iron and Steel Institute of Japan, v. 56, n. 5, p. 803–811, 2016.

WHEEL, M. A. A geometrically versatile finite volume formulation for plane elastostatic stress analysis. **The Journal of Strain Analysis for Engineering Design**, SAGE Publications, v. 31, n. 2, p. 111–116, 1996.

WILLIAMS, J.; LEWIS, R.; MORGAN, K. An elasto-viscoplastic thermal stress model with applications to the continuous casting of metals. **International Journal for Numerical Methods in Engineering**, Wiley Online Library, v. 14, n. 1, p. 1–9, 1979.

WINSLOW, A. M. Numerical solution of the quasilinear poisson equation in a nonuniform triangle mesh. **Journal of computational physics**, Elsevier, v. 1, n. 2, p. 149–172, 1966.

WONG, H.; LEO, C. J.; DUFOUR, N. Thermodynamics in mono and biphasic continuum mechanics. In: **Thermodynamics-Systems in Equilibrium and Non-Equilibrium**. [S.l.]: InTech, 2011.

WOODWARD, C. S.; DAWSON, C. N. Analysis of expanded mixed finite element methods for a nonlinear parabolic equation modeling flow into variably saturated porous media. **SIAM Journal on Numerical Analysis**, SIAM, v. 37, n. 3, p. 701–724, 2000.

ZHANG, B.; XU, C.-L.; WANG, S.-M. Generalized source finite volume method for radiative transfer equation in participating media. **Journal of Quantitative Spectroscopy and Radiative Transfer**, Elsevier, v. 189, p. 189–197, 2017.

ZHU, H. **Coupled Thermo-Mechanical Finite-Element Model With Application to Initial Soldification**. Tese (Doutorado) — PhD thesis, The University of Illinois at Urbana-Champaign, 1996.

ZIENKIEWICK, O. C.; TAYLOR, R. L. **The Finite Element Method: Basic Formulation and Linear Problems**. [S.l.]: Mc Graw-Hill Book Company, 1989. v. 1.

ZIENKIEWICZ, O. C.; TAYLOR, R. L. **The Finite Element Method, 4th edn McGraw-Hill**. [S.l.]: London, 1991. v. 2.

ZOU, J.; TSENG, A. Microscopic modeling of fundamental phase transformations in continuous castings of steel. **Metallurgical Transactions A**, Springer, v. 23, n. 2, p. 457–467, 1992.

APPENDIX A – STRESS AND STRAIN IN AN ELASTIC SOLID

Admitting the two-dimensional approach, the constitutive elastic stress-strain matrix for plane strain and plane stress can be introduced using Voigt's notation as follows (LOGAN, 2002)

$$\begin{bmatrix} \sigma_{xx} \\ \sigma_{yy} \\ \sigma_{xy} \end{bmatrix} = \frac{E\bar{\nu}}{(1-\nu^2)} \begin{bmatrix} 1 & \zeta\nu & 0 \\ \zeta\nu & 1 & 0 \\ 0 & 0 & \frac{\bar{\nu}(1-\nu)}{2} \end{bmatrix} \left(\begin{bmatrix} \varepsilon_{xx} \\ \varepsilon_{yy} \\ 2\varepsilon_{xy} \end{bmatrix} - \begin{bmatrix} \varepsilon_{xx}^{th} \\ \varepsilon_{yy}^{th} \\ 0 \end{bmatrix} \right). \tag{A.1}$$

For convenience, the parameters ζ and $\bar{\nu}$ are introduced in order to define the plane stress ($\sigma_{zz} = \sigma_{zy} = \sigma_{zx}$=0) and the plane strain ($\varepsilon_{zz} = \varepsilon_{zy} = \varepsilon_{zx}$=0). Additionally, for plane stress is assumed $\zeta = \bar{\nu} = 1$, and one additional term to evaluate the normal or out-of-plane strain component (z-direction)

$$\varepsilon_{zz} = -\frac{\nu}{E}(\sigma_{xx} + \sigma_{yy}) + \alpha\Delta T. \tag{A.2}$$

On the other hand, plane strain takes place when $\zeta = \dfrac{1}{1-\nu}$ and $\bar{\nu} = \dfrac{(1-\nu)^2}{1-2\nu}$, with an additional expression to evaluate the normal stress in z-direction

$$\sigma_{zz} = -\frac{E\nu(\varepsilon_{xx} + \varepsilon_{yy})}{(1-2\nu)(1+\nu)} + \frac{E\alpha}{1-2\nu}\Delta T. \tag{A.3}$$

APPENDIX B – EBFVM APPLIED TO ELASTIC-PLASTIC PROBLEMS

In section is described succinctly the formalism used in the Fortran implementation code applied to analyze the stress state of solids.

B.1 EbFVM discretization

Considering the momentum equation from the point of view of quasi-static equilibrium, we are able to express:

$$\oint_{\partial V} d\sigma_{ij} n_j \, ds = F_{i,\text{ext}} - F_{i,\text{int}} - F_{i,\text{th}}, \tag{B.1}$$

where

$$n_j = \begin{bmatrix} n_x & 0 & n_y \\ 0 & n_y & n_x \end{bmatrix}, \tag{B.2}$$

and

$$d\sigma_{ij} = D^{ep}_{ijkl} d\varepsilon_{kl}, \tag{B.3}$$

where $D^{ep}_{ijkl} = \dfrac{\partial \sigma_{ij}}{\partial \varepsilon_{kl}}$. In addition, the stress increment can be written in terms of the total deformation increment

$$d\sigma_{ij} = \begin{bmatrix} d\sigma_{xx} \\ d\sigma_{yy} \\ d\sigma_{xy} \end{bmatrix} = \begin{bmatrix} a_{11} & a_{12} & a_{13} \\ a_{21} & a_{22} & a_{23} \\ a_{31} & a_{32} & a_{33} \end{bmatrix} \begin{bmatrix} d\varepsilon_{xx} \\ d\varepsilon_{yy} \\ d\varepsilon_{xy} \end{bmatrix}, \tag{B.4}$$

and the total deformation is expressed as a function of the displacement

$$\begin{bmatrix} d\varepsilon^e_{xx} \\ d\varepsilon^e_{yy} \\ d\varepsilon^e_{xy} \end{bmatrix} = \begin{bmatrix} \frac{\partial}{\partial x} & 0 \\ 0 & \frac{\partial}{\partial y} \\ \frac{\partial}{\partial y} & \frac{\partial}{\partial x} \end{bmatrix} \begin{bmatrix} \delta u_x \\ \delta u_y \end{bmatrix}. \tag{B.5}$$

Therefore, the numerical integration using EbFVM is performed at each sub-control volume, as illustrate in Fig. 50.

The expression in Eq. (B.1) evaluates the physical properties at each integration point accounting to the following manner

$$\oint_{\partial V} d\sigma_{ij} n_j \, ds = \sum_{k=1}^{2} \int_{\partial V_k} d\sigma_{ij} n_j \, ds, \tag{B.6}$$

Figure 50 – EbFVM integration at the sub-control volume.

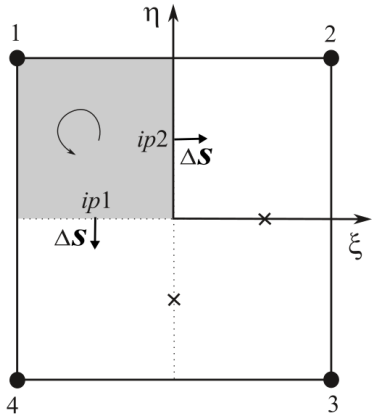

which can be approximated via midpoint rule, as

$$\sum_{k=1}^{2}\int_{\partial V_k} d\sigma_{ij}n_j\,ds \approx \sum_{k=1}^{2}(\Delta s)_k \begin{bmatrix} \sigma_{xx}n_x & \sigma_{xy}n_x \\ \sigma_{yx}n_x & \sigma_{yy}n_y \end{bmatrix}_k . \tag{B.7}$$

In order to numerically approximate any arbitrary variable anywhere inside the element, we introduce the following interpolation approach

$$\mathbf{v} \approx \sum_{i=1}^{4} N_i \mathbf{v}_i \tag{B.8}$$

where N_i is the shape function, which is given by

$$\begin{aligned} N_1(\xi,\eta) &= \frac{1}{4}(1-\xi-\eta+\xi\eta), \\ N_2(\xi,\eta) &= \frac{1}{4}(1-\xi+\eta-\xi\eta), \\ N_3(\xi,\eta) &= \frac{1}{4}(1+\xi+\eta+\xi\eta), \\ N_4(\xi,\eta) &= \frac{1}{4}(1+\xi-\eta-\xi\eta). \end{aligned} \tag{B.9}$$

The matrix in Eq. (B.7) can be further expressed considering Eqs. (B.2), (B.4), and (B.9), as

$$\begin{bmatrix} \sigma_{xx}n_x & \sigma_{xy}n_x \\ \sigma_{yx}n_x & \sigma_{yy}n_y \end{bmatrix} =$$
$$\sum_{l=1}^{4} \begin{bmatrix} n_x\left(a_{11}\frac{\partial N_l}{\partial x}+a_{13}\frac{\partial N_l}{\partial y}\right)+n_y\left(a_{31}\frac{\partial N_l}{\partial x}+a_{33}\frac{\partial N_l}{\partial y}\right) & n_x\left(a_{12}\frac{\partial N_l}{\partial y}+a_{13}\frac{\partial N_l}{\partial x}\right)+n_y\left(a_{32}\frac{\partial N_l}{\partial y}+a_{33}\frac{\partial N_l}{\partial x}\right) \\ n_y\left(a_{21}\frac{\partial N_l}{\partial x}+a_{23}\frac{\partial N_l}{\partial y}\right)+n_x\left(a_{31}\frac{\partial N_l}{\partial x}+a_{33}\frac{\partial N_l}{\partial y}\right) & n_y\left(a_{22}\frac{\partial N_l}{\partial y}+a_{23}\frac{\partial N_l}{\partial x}\right)+n_x\left(a_{32}\frac{\partial N_l}{\partial y}+a_{33}\frac{\partial N_i}{\partial x}\right) \end{bmatrix}$$
$$\times \begin{bmatrix} \delta u_{x,l} \\ \delta u_{y,l} \end{bmatrix}. \tag{B.10}$$

The material and geometrical properties can be gathered in a compact form with the introduction of the matrix G, as

$$\sum_{k=1}^{2}\begin{bmatrix}\sigma_{xx}n_x & \sigma_{xy}n_y\\ \sigma_{yx}n_x & \sigma_{yy}n_y\end{bmatrix}_k = \sum_{k=1}^{2}\sum_{l=1}^{4}\begin{bmatrix}G_{xx,l} & G_{xy,l}\\ G_{yx,l} & G_{yy,l}\end{bmatrix}_k\begin{bmatrix}\delta u_{x,l}\\ \delta u_{y,l}\end{bmatrix} \tag{B.11}$$

the G matrix can also be seen as

$$A_{ij}^{sc} = \sum_{k=1}^{2}\sum_{l=1}^{4}\begin{bmatrix}G_{xx,l} & G_{xy,l}\\ G_{yx,l} & G_{yy,l}\end{bmatrix}_k, \tag{B.12}$$

where A_{ij}^{sc} is the stiffness matrix for the control volume.

By visiting each sub-control volume and assembling the ones that share the same vertex, we are able to rewrite Eq. (B.1) in terms of the following approximation

$$A_{ij}\delta u_i = F_{i,\text{ext}} - F_{i,\text{int}} - F_{i,\text{th}} = R_i, \tag{B.13}$$

where A_{ij} is the global stiffness matrix.

The iterative displacement field is given by

$$\delta u_i = -A_{ij}^{-1}R_i. \tag{B.14}$$

The displacement increment is updated by

$$u_i^{n+1} = u_i^n + \delta u_i. \tag{B.15}$$

and using the last converged u_i^* and the previous displacement vectors calculated, we are able to evaluate the increment displacement field as

$$\Delta u_i^{n+1} = u_i^{n+1} - u_i^*. \tag{B.16}$$

The vector force is expressed as

$$F_{i,\text{th}}^{n+1} = \sum_{k=1}^{ip}\int_{\partial V_k} D_{ijlm}^{ep,n+1}\varepsilon_{lm}^{n+1,th}n_j\,dS_k, \tag{B.17}$$

and internal force vector is

$$F_{i,\text{int}}^{n+1}\left(u_i^{n+1}\right) = \sum_{k=1}^{ip}\int_{\partial V_k}\sigma_{ij}^{n+1}n_j\,dS_k. \tag{B.18}$$

B.2 3D Return Mapping

For isotropic materials, the von Mises criteria σ_v can be written as

$$\sigma_v = \sqrt{3J_2} = \sqrt{\frac{3}{2} S_{ij} S_{ij}}, \tag{B.19}$$

where

$$S_{ij} = \sigma_{ij} - \frac{1}{3}\delta_{ij}\sigma_{kk}, \tag{B.20}$$

or

$$\sigma_v^2 = \frac{1}{2}\left[(\sigma_{11}-\sigma_{22})^2 + (\sigma_{22}-\sigma_{33})^2 + (\sigma_{33}-\sigma_{11})^2 + 6(\sigma_{23}^2 + \sigma_{31}^2 + \sigma_{12}^2)\right]. \tag{B.21}$$

The yield function which is responsible for verify whether the current stress state is within the elastic or inelastic domain is given by

$$f\left(\sigma_{ij}, \bar{\varepsilon}\right) = \sigma_v - \sigma_y\left(\bar{\varepsilon}\right). \tag{B.22}$$

To define the inelastic deformation from the viewpoint of the associative flow rule, we use

$$\begin{aligned}
\frac{\partial \sigma_v}{\partial \sigma_{ij}} &= \frac{\partial}{\partial \sigma_{ij}}\left(\sqrt{\frac{3}{2} S_{ij} S_{ij}}\right) \\
&= \frac{3}{2}\left(\frac{3}{2} S_{ij} S_{ij}\right)^{-\frac{1}{2}} S_{ij} \\
&= \sqrt{\frac{3}{2}} \frac{S_{ij}}{||S_{ij}||},
\end{aligned} \tag{B.23}$$

and finally,

$$\varepsilon_{ij}^{i} = \bar{\varepsilon}\frac{\partial f}{\partial \sigma_{ij}} = \bar{\varepsilon}\sqrt{\frac{3}{2}}\frac{S_{ij}}{||S_{ij}||} \tag{B.24}$$

The total deformation increment is calculated using the displacement evaluated at the structural level by Eq. (B.16), the differential operator defined in Eq. (B.5), and the shape function in Eq. (B.8)

$$\Delta\varepsilon_{ij} = \left[L_{ij}\sum_{l=1}^{nve} N_l\right]\left[\Delta u_{j(l)}\right], \tag{B.25}$$

and the stress increment is given by

$$\Delta\sigma_{ij}^{n+1} = D_{ijkl}^{e}\Delta\varepsilon_{ij}^{n+1}, \tag{B.26}$$

which update the current stress state

$$\sigma_{ij}^{n+1} = \sigma_{ij}^{*} + \Delta\sigma_{ij}^{n+1}, \tag{B.27}$$

where σ_{ij}^{*} is the previous converged tensor.

From the function f defined in (B.22), in case of $f > 0$, the stress state is within the inelastic domain and correction in the stress has to be performed.

Then, by adding the inelastic deformation increment, Eq. (B.24), in Eq. (B.27), we have

$$\sigma_{ij}^{n+1} = \sigma_{ij}^{c} - D_{ijkl}^{e}\Delta\bar{\varepsilon}^{n}\sqrt{\frac{3}{2}}\frac{S_{kl}^{n}}{||S_{kl}^{n}||}, \tag{B.28}$$

where $\sigma_{ij}^{c} = \sigma_{ij}^{*} + \Delta\sigma_{ij}^{n+1}$ is defined as the candidate stress.

To impose the aforementioned corrections, we introduce the definition of the following residue functions

$$R_{\bar{\varepsilon}}^{n} = \left[D_{ijkl}^{e}\right]^{-1}(\sigma_{kl}^{n} - \sigma_{kl}^{c}) + \Delta\bar{\varepsilon}^{n}\sqrt{\frac{3}{2}}\frac{S_{ij}\left(\sigma_{ij}^{n}\right)}{||S_{ij}\left(\sigma_{ij}^{n}\right)||} \tag{B.29}$$

$$R_{\bar{\varepsilon}}^{n} = \sqrt{3J_2\left(\sigma_{ij}^{n}\right)} - \sigma_y\left(\Delta\bar{\varepsilon}^{n}\right) \tag{B.30}$$

where the internal variable $\bar{\varepsilon}^{n+1}$ and the stress state σ_{ij}^{n+1} is calculated via Newton-Raphson iterative process, as

$$\begin{bmatrix}\delta\sigma_{ij}^{n+1}\\ \delta\bar{\varepsilon}^{n+1}\end{bmatrix} = -[J]^{-1}\begin{bmatrix}R_{\sigma}^{n}\\ R_{\bar{\varepsilon}}^{n}\end{bmatrix}, \tag{B.31}$$

with

$$\sigma_{ij}^{n+1} = \sigma_{ij}^{n} + \delta\sigma_{ij}^{n+1}$$
$$\bar{\varepsilon}^{n+1} = \bar{\varepsilon}^{n} + \delta\bar{\varepsilon}^{n+1},$$

where J is the Jacobian matrix and it is given by

$$J = \begin{bmatrix}\dfrac{\partial R_{\sigma}}{\partial\sigma} & \dfrac{\partial R_{\sigma}}{\partial\bar{\varepsilon}}\\ \dfrac{\partial R_{\bar{\varepsilon}}}{\partial\sigma} & \dfrac{\partial R_{\bar{\varepsilon}}}{\partial\bar{\varepsilon}}\end{bmatrix}. \tag{B.32}$$

The Jacobian matrix is explicitly expressed, as

$$J = \begin{bmatrix} \frac{\partial R_{\sigma_{xx}}}{\partial \sigma_{xx}} & \frac{\partial R_{\sigma_{xx}}}{\partial \sigma_{yy}} & \frac{\partial R_{\sigma_{xx}}}{\partial \sigma_{zz}} & \frac{\partial R_{\sigma_{xx}}}{\partial \sigma_{xy}} & \frac{\partial R_{\sigma_{xx}}}{\partial \sigma_{yz}} & \frac{\partial R_{\sigma_{xx}}}{\partial \sigma_{xz}} & \frac{\partial R_{\sigma_{xx}}}{\partial \bar{\varepsilon}} \\ \frac{\partial R_{\sigma_{yy}}}{\partial \sigma_{xx}} & \frac{\partial R_{\sigma_{yy}}}{\partial \sigma_{yy}} & \frac{\partial R_{\sigma_{yy}}}{\partial \sigma_{zz}} & \frac{\partial R_{\sigma_{yy}}}{\partial \sigma_{xy}} & \frac{\partial R_{\sigma_{yy}}}{\partial \sigma_{yz}} & \frac{\partial R_{\sigma_{yy}}}{\partial \sigma_{xz}} & \frac{\partial R_{\sigma_{yy}}}{\partial \bar{\varepsilon}} \\ \frac{\partial R_{\sigma_{zz}}}{\partial \sigma_{xx}} & \frac{\partial R_{\sigma_{zz}}}{\partial \sigma_{yy}} & \frac{\partial R_{\sigma_{zz}}}{\partial \sigma_{zz}} & \frac{\partial R_{\sigma_{zz}}}{\partial \sigma_{xy}} & \frac{\partial R_{\sigma_{zz}}}{\partial \sigma_{yz}} & \frac{\partial R_{\sigma_{zz}}}{\partial \sigma_{xz}} & \frac{\partial R_{\sigma_{zz}}}{\partial \bar{\varepsilon}} \\ \frac{\partial R_{\sigma_{xy}}}{\partial \sigma_{xx}} & \frac{\partial R_{\sigma_{xy}}}{\partial \sigma_{yy}} & \frac{\partial R_{\sigma_{xy}}}{\partial \sigma_{zz}} & \frac{\partial R_{\sigma_{xy}}}{\partial \sigma_{xy}} & \frac{\partial R_{\sigma_{xy}}}{\partial \sigma_{yz}} & \frac{\partial R_{\sigma_{xy}}}{\partial \sigma_{xz}} & \frac{\partial R_{\sigma_{xy}}}{\partial \bar{\varepsilon}} \\ \frac{\partial R_{\sigma_{yz}}}{\partial \sigma_{xx}} & \frac{\partial R_{\sigma_{yz}}}{\partial \sigma_{yy}} & \frac{\partial R_{\sigma_{yz}}}{\partial \sigma_{zz}} & \frac{\partial R_{\sigma_{yz}}}{\partial \sigma_{xy}} & \frac{\partial R_{\sigma_{yz}}}{\partial \sigma_{yz}} & \frac{\partial R_{\sigma_{yz}}}{\partial \sigma_{xz}} & \frac{\partial R_{\sigma_{xy}}}{\partial \bar{\varepsilon}} \\ \frac{\partial R_{\sigma_{xz}}}{\partial \sigma_{xx}} & \frac{\partial R_{\sigma_{xz}}}{\partial \sigma_{yy}} & \frac{\partial R_{\sigma_{xz}}}{\partial \sigma_{zz}} & \frac{\partial R_{\sigma_{xz}}}{\partial \sigma_{xy}} & \frac{\partial R_{\sigma_{xz}}}{\partial \sigma_{yz}} & \frac{\partial R_{\sigma_{xz}}}{\partial \sigma_{xz}} & \frac{\partial R_{\sigma_{xz}}}{\partial \bar{\varepsilon}} \\ \frac{\partial R_{\bar{\varepsilon}}}{\partial \sigma_{xx}} & \frac{\partial R_{\bar{\varepsilon}}}{\partial \sigma_{yy}} & \frac{\partial R_{\bar{\varepsilon}}}{\partial \sigma_{zz}} & \frac{\partial R_{\bar{\varepsilon}}}{\partial \sigma_{xy}} & \frac{\partial R_{\bar{\varepsilon}}}{\partial \sigma_{yz}} & \frac{\partial R_{\bar{\varepsilon}}}{\partial \sigma_{xz}} & \frac{\partial R_{\bar{\varepsilon}}}{\partial \bar{\varepsilon}} \end{bmatrix} \tag{B.33}$$

Additionally, the components of the vectors R_σ and $R_{\bar{\varepsilon}}$ are given by

$$\frac{\partial R_{\sigma_{xx}}}{\partial \sigma_{xx}} = a_{11} + \Delta\bar{\varepsilon}\sqrt{\frac{3}{2}}\frac{\partial^2 f}{\partial \sigma_{xx}^2}$$
$$\frac{\partial R_{\sigma_{xx}}}{\partial \sigma_{yy}} = a_{12} + \Delta\bar{\varepsilon}\sqrt{\frac{3}{2}}\frac{\partial^2 f}{\partial \sigma_{xx}\partial \sigma_{yy}}$$
$$\frac{\partial R_{\sigma_{xx}}}{\partial \sigma_{zz}} = a_{13} + \Delta\bar{\varepsilon}\sqrt{\frac{3}{2}}\frac{\partial^2 f}{\partial \sigma_{xx}\partial \sigma_{zz}}$$
$$\frac{\partial R_{\sigma_{xx}}}{\partial \sigma_{xy}} = a_{14} + \Delta\bar{\varepsilon}\sqrt{\frac{3}{2}}\frac{\partial^2 f}{\partial \sigma_{xx}\partial \sigma_{xy}}$$
$$\frac{\partial R_{\sigma_{xx}}}{\partial \sigma_{yz}} = a_{15} + \Delta\bar{\varepsilon}\sqrt{\frac{3}{2}}\frac{\partial^2 f}{\partial \sigma_{xx}\partial \sigma_{yz}}$$
$$\frac{\partial R_{\sigma_{xx}}}{\partial \sigma_{xz}} = a_{16} + \Delta\bar{\varepsilon}\sqrt{\frac{3}{2}}\frac{\partial^2 f}{\partial \sigma_{xx}\partial \sigma_{xz}}$$
$$\frac{\partial R_{\sigma_{xx}}}{\partial \bar{\varepsilon}} = \sqrt{\frac{3}{2}}\frac{S_{xx}}{||S_{ij}||}$$
$$\frac{\partial R_{\sigma_{yy}}}{\partial \sigma_{xx}} = a_{21} + \Delta\bar{\varepsilon}\sqrt{\frac{3}{2}}\frac{\partial^2 f}{\partial \sigma_{yy}\partial \sigma_{xx}}$$
$$\frac{\partial R_{\sigma_{yy}}}{\partial \sigma_{yy}} = a_{22} + \Delta\bar{\varepsilon}\sqrt{\frac{3}{2}}\frac{\partial^2 f}{\partial \sigma_{yy}^2}$$
$$\frac{\partial R_{\sigma_{yy}}}{\partial \sigma_{zz}} = a_{23} + \Delta\bar{\varepsilon}\sqrt{\frac{3}{2}}\frac{\partial^2 f}{\partial \sigma_{yy}\partial \sigma_{zz}}$$
$$\frac{\partial R_{\sigma_{yy}}}{\partial \sigma_{xy}} = a_{24} + \Delta\bar{\varepsilon}\sqrt{\frac{3}{2}}\frac{\partial^2 f}{\partial \sigma_{yy}\partial \sigma_{xy}}$$
$$\frac{\partial R_{\sigma_{yy}}}{\partial \sigma_{yz}} = a_{25} + \Delta\bar{\varepsilon}\sqrt{\frac{3}{2}}\frac{\partial^2 f}{\partial \sigma_{yy}\partial \sigma_{yz}}$$

$$\frac{\partial R_{\sigma_{yy}}}{\partial \sigma_{xz}} = a_{26} + \Delta\bar{\varepsilon}\sqrt{\frac{3}{2}}\frac{\partial^2 f}{\partial \sigma_{yy}\partial \sigma_{xz}}$$
$$\frac{\partial R_{\sigma_{yy}}}{\partial \bar{\varepsilon}} = \sqrt{\frac{3}{2}}\frac{S_{yy}}{||S_{ij}||}$$
$$\frac{\partial R_{\sigma_{zz}}}{\partial \sigma_{xx}} = a_{31} + \Delta\bar{\varepsilon}\sqrt{\frac{3}{2}}\frac{\partial^2 f}{\partial \sigma_{zz}\partial \sigma_{xx}}$$
$$\frac{\partial R_{\sigma_{zz}}}{\partial \sigma_{yy}} = a_{32} + \Delta\bar{\varepsilon}\sqrt{\frac{3}{2}}\frac{\partial^2 f}{\partial \sigma_{zz}\partial \sigma_{yy}}$$
$$\frac{\partial R_{\sigma_{zz}}}{\partial \sigma_{zz}} = a_{33} + \Delta\bar{\varepsilon}\sqrt{\frac{3}{2}}\frac{\partial^2 f}{\partial \sigma_{zz}^2}$$
$$\frac{\partial R_{\sigma_{zz}}}{\partial \sigma_{xy}} = a_{34} + \Delta\bar{\varepsilon}\sqrt{\frac{3}{2}}\frac{\partial^2 f}{\partial \sigma_{zz}\partial \sigma_{xy}}$$
$$\frac{\partial R_{\sigma_{zz}}}{\partial \sigma_{yz}} = a_{35} + \Delta\bar{\varepsilon}\sqrt{\frac{3}{2}}\frac{\partial^2 f}{\partial \sigma_{zz}\partial \sigma_{yz}}$$
$$\frac{\partial R_{\sigma_{zz}}}{\partial \sigma_{xz}} = a_{36} + \Delta\bar{\varepsilon}\sqrt{\frac{3}{2}}\frac{\partial^2 f}{\partial \sigma_{zz}\partial \sigma_{xz}}$$
$$\frac{\partial R_{\sigma_{zz}}}{\partial \bar{\varepsilon}} = \sqrt{\frac{3}{2}}\frac{S_{zz}}{||S_{ij}||}$$
$$\frac{\partial R_{\sigma_{xy}}}{\partial \sigma_{xx}} = a_{41} + \Delta\bar{\varepsilon}\sqrt{\frac{3}{2}}\frac{\partial^2 f}{\partial \sigma_{xy}\partial \sigma_{xx}}$$
$$\frac{\partial R_{\sigma_{xy}}}{\partial \sigma_{yy}} = a_{42} + \Delta\bar{\varepsilon}\sqrt{\frac{3}{2}}\frac{\partial^2 f}{\partial \sigma_{xy}\partial \sigma_{yy}}$$
$$\frac{\partial R_{\sigma_{xy}}}{\partial \sigma_{zz}} = \alpha_{43} + \Delta\bar{\varepsilon}\sqrt{\frac{3}{2}}\frac{\partial^2 f}{\partial \sigma_{xy}\partial \sigma_{zz}}$$
$$\frac{\partial R_{\sigma_{xy}}}{\partial \sigma_{xy}} = a_{44} + \Delta\bar{\varepsilon}\sqrt{\frac{3}{2}}\frac{\partial^2 f}{\partial \sigma_{xy}^2}$$
$$\frac{\partial R_{\sigma_{xy}}}{\partial \sigma_{yz}} = a_{45} + \Delta\bar{\varepsilon}\sqrt{\frac{3}{2}}\frac{\partial^2 f}{\partial \sigma_{xy}\partial \sigma_{yz}}$$
$$\frac{\partial R_{\sigma_{xy}}}{\partial \sigma_{xz}} = a_{46} + \Delta\bar{\varepsilon}\sqrt{\frac{3}{2}}\frac{\partial^2 f}{\partial \sigma_{xy}\partial \sigma_{xz}}$$
$$\frac{\partial R_{\sigma_{xy}}}{\partial \bar{\varepsilon}} = \sqrt{\frac{3}{2}}\frac{S_{xy}}{||S_{ij}||}$$
$$\frac{\partial R_{\sigma_{yz}}}{\partial \sigma_{xx}} = a_{51} + \Delta\bar{\varepsilon}\sqrt{\frac{3}{2}}\frac{\partial^2 f}{\partial \sigma_{yz}\partial \sigma_{xx}}$$
$$\frac{\partial R_{\sigma_{yz}}}{\partial \sigma_{yy}} = a_{52} + \Delta\bar{\varepsilon}\sqrt{\frac{3}{2}}\frac{\partial^2 f}{\partial \sigma_{yz}\partial \sigma_{yy}}$$
$$\frac{\partial R_{\sigma_{yz}}}{\partial \sigma_{zz}} = a_{53} + \Delta\bar{\varepsilon}\sqrt{\frac{3}{2}}\frac{\partial^2 f}{\partial \sigma_{yz}\partial \sigma_{zz}}$$

$$\frac{\partial R_{\sigma_{yz}}}{\partial \sigma_{xy}} = a_{54} + \Delta\bar{\varepsilon}\sqrt{\frac{3}{2}}\frac{\partial^2 f}{\partial \sigma_{yz}\partial \sigma_{xy}}$$
$$\frac{\partial R_{\sigma_{yz}}}{\partial \sigma_{yz}} = a_{55} + \Delta\bar{\varepsilon}\sqrt{\frac{3}{2}}\frac{\partial^2 f}{\partial \sigma_{yz}^2}$$
$$\frac{\partial R_{\sigma_{yz}}}{\partial \sigma_{xz}} = a_{56} + \Delta\bar{\varepsilon}\sqrt{\frac{3}{2}}\frac{\partial^2 f}{\partial \sigma_{yz}\partial \sigma_{xz}}$$
$$\frac{\partial R_{\sigma_{yz}}}{\partial \bar{\varepsilon}} = \sqrt{\frac{3}{2}}\frac{S_{yz}}{||S_{ij}||}$$
$$\frac{\partial R_{\sigma_{xz}}}{\partial \sigma_{xx}} = a_{61} + \Delta\bar{\varepsilon}\sqrt{\frac{3}{2}}\frac{\partial^2 f}{\partial \sigma_{xy}\partial \sigma_{xx}}$$
$$\frac{\partial R_{\sigma_{xz}}}{\partial \sigma_{yy}} = a_{62} + \Delta\bar{\varepsilon}\sqrt{\frac{3}{2}}\frac{\partial^2 f}{\partial \sigma_{xz}\partial \sigma_{yy}}$$
$$\frac{\partial R_{\sigma_{xz}}}{\partial \sigma_{yy}} = a_{63} + \Delta\bar{\varepsilon}\sqrt{\frac{3}{2}}\frac{\partial^2 f}{\partial \sigma_{xz}\partial \sigma_{zz}}$$
$$\frac{\partial R_{\sigma_{xz}}}{\partial \sigma_{xy}} = a_{64} + \Delta\bar{\varepsilon}\sqrt{\frac{3}{2}}\frac{\partial^2 f}{\partial \sigma_{xz}\partial \sigma_{xy}}$$
$$\frac{\partial R_{\sigma_{xz}}}{\partial \sigma_{yz}} = a_{65} + \Delta\bar{\varepsilon}\sqrt{\frac{3}{2}}\frac{\partial^2 f}{\partial \sigma_{xz}\partial \sigma_{yz}}$$
$$\frac{\partial R_{\sigma_{xz}}}{\partial \sigma_{xz}} = a_{66} + \Delta\bar{\varepsilon}\sqrt{\frac{3}{2}}\frac{\partial^2 f}{\partial \sigma_{xz}^2}$$
$$\frac{\partial R_{\sigma_{xz}}}{\partial \bar{\varepsilon}} = \sqrt{\frac{3}{2}}\frac{S_{xz}}{||S_{ij}||}$$
$$\frac{\partial R_{\bar{\varepsilon}}}{\partial \sigma_{xx}} = \sqrt{\frac{3}{2}}\frac{S_{xx}}{||S_{ij}||}$$
$$\frac{\partial R_{\bar{\varepsilon}}}{\partial \sigma_{yy}} = \sqrt{\frac{3}{2}}\frac{S_{yy}}{||S_{ij}||}$$
$$\frac{\partial R_{\bar{\varepsilon}}}{\partial \sigma_{yy}} = \sqrt{\frac{3}{2}}\frac{S_{yy}}{||S_{ij}||}$$
$$\frac{\partial R_{\bar{\varepsilon}}}{\partial \sigma_{xy}} = \sqrt{\frac{3}{2}}\frac{S_{xy}}{||S_{ij}||}$$
$$\frac{\partial R_{\bar{\varepsilon}}}{\partial \sigma_{xz}} = \sqrt{\frac{3}{2}}\frac{S_{yz}}{||S_{ij}||}$$
$$\frac{\partial R_{\bar{\varepsilon}}}{\partial \sigma_{xz}} = \sqrt{\frac{3}{2}}\frac{S_{xz}}{||S_{ij}||}$$
$$\frac{\partial R_{\bar{\varepsilon}}}{\partial \bar{\varepsilon}} = \frac{\partial f}{\partial \bar{\varepsilon}}$$

The derivatives are calculated as

$$\frac{\partial^2 f}{\partial \sigma_{xx}^2} = \frac{3}{2\sqrt{3J_2}}\left[\frac{\partial^2 J_2}{\partial \sigma_{xx}^2} - \frac{3}{2}\left(\frac{\partial J_2}{\partial \sigma_{xx}}\right)^2 \frac{1}{3J_2}\right]$$

$$\frac{\partial^2 f}{\partial \sigma_{xx}\partial \sigma_{yy}} = \frac{3}{2\sqrt{3J_2}}\left[\frac{\partial^2 J_2}{\partial \sigma_{xx}\partial \sigma_{yy}} - \frac{3}{2}\left(\frac{\partial J_2}{\partial \sigma_{xx}}\frac{\partial J_2}{\partial \sigma_{yy}}\right)\frac{1}{3J_2}\right]$$

$$\frac{\partial^2 f}{\partial \sigma_{xx}\partial \sigma_{zz}} = \frac{3}{2\sqrt{3J_2}}\left[\frac{\partial^2 J_2}{\partial \sigma_{xx}\partial \sigma_{zz}} - \frac{3}{2}\left(\frac{\partial J_2}{\partial \sigma_{xx}}\frac{\partial J_2}{\partial \sigma_{zz}}\right)\frac{1}{3J_2}\right]$$

$$\frac{\partial^2 f}{\partial \sigma_{xx}\partial \sigma_{xy}} = \frac{3}{2\sqrt{3J_2}}\left[\frac{\partial^2 J_2}{\partial \sigma_{xx}\partial \sigma_{xy}} - \frac{3}{2}\left(\frac{\partial J_2}{\partial \sigma_{xx}}\frac{\partial J_2}{\partial \sigma_{xy}}\right)\frac{1}{3J_2}\right]$$

$$\frac{\partial^2 f}{\partial \sigma_{xx}\partial \sigma_{xz}} = \frac{3}{2\sqrt{3J_2}}\left[\frac{\partial^2 J_2}{\partial \sigma_{xx}\partial \sigma_{yz}} - \frac{3}{2}\left(\frac{\partial J_2}{\partial \sigma_{xx}}\frac{\partial J_2}{\partial \sigma_{yz}}\right)\frac{1}{3J_2}\right]$$

$$\frac{\partial^2 f}{\partial \sigma_{xx}\partial \sigma_{xz}} = \frac{3}{2\sqrt{3J_2}}\left[\frac{\partial^2 J_2}{\partial \sigma_{xx}\partial \sigma_{xz}} - \frac{3}{2}\left(\frac{\partial J_2}{\partial \sigma_{xx}}\frac{\partial J_2}{\partial \sigma_{xz}}\right)\frac{1}{3J_2}\right]$$

$$\frac{\partial^2 f}{\partial \sigma_{yy}\partial \sigma_{xx}} = \frac{3}{2\sqrt{3J_2}}\left[\frac{\partial^2 J_2}{\partial \sigma_{yy}\partial \sigma_{xx}} - \frac{3}{2}\left(\frac{\partial J_2}{\partial \sigma_{yy}}\frac{\partial J_2}{\partial \sigma_{xx}}\right)\frac{1}{3J_2}\right]$$

$$\frac{\partial^2 f}{\partial \sigma_{yy}^2} = \frac{3}{2\sqrt{3J_2}}\left[\frac{\partial^2 J_2}{\partial \sigma_{yy}^2} - \frac{3}{2}\left(\frac{\partial J_2}{\partial \sigma_{yy}}\right)^2 \frac{1}{3J_2}\right]$$

$$\frac{\partial^2 f}{\partial \sigma_{yy}\partial \sigma_{yy}} = \frac{3}{2\sqrt{3J_2}}\left[\frac{\partial^2 J_2}{\partial \sigma_{yy}\partial \sigma_{zz}} - \frac{3}{2}\left(\frac{\partial J_2}{\partial \sigma_{yy}}\frac{\partial J_2}{\partial \sigma_{zz}}\right)\frac{1}{3J_2}\right]$$

$$\frac{\partial^2 f}{\partial \sigma_{yy}\partial \sigma_{xy}} = \frac{3}{2\sqrt{3J_2}}\left[\frac{\partial^2 J_2}{\partial \sigma_{yy}\partial \sigma_{xy}} - \frac{3}{2}\left(\frac{\partial J_2}{\partial \sigma_{yy}}\frac{\partial J_2}{\partial \sigma_{xy}}\right)\frac{1}{3J_2}\right]$$

$$\frac{\partial^2 f}{\partial \sigma_{yy}\partial \sigma_{yz}} = \frac{3}{2\sqrt{3J_2}}\left[\frac{\partial^2 J_2}{\partial \sigma_{yy}\partial \sigma_{yz}} - \frac{3}{2}\left(\frac{\partial J_2}{\partial \sigma_{yy}}\frac{\partial J_2}{\partial \sigma_{yz}}\right)\frac{1}{3J_2}\right]$$

$$\frac{\partial^2 f}{\partial \sigma_{yy}\partial \sigma_{xz}} = \frac{3}{2\sqrt{3J_2}}\left[\frac{\partial^2 J_2}{\partial \sigma_{yy}\partial \sigma_{xz}} - \frac{3}{2}\left(\frac{\partial J_2}{\partial \sigma_{yy}}\frac{\partial J_2}{\partial \sigma_{xz}}\right)\frac{1}{3J_2}\right]$$

$$\frac{\partial^2 f}{\partial \sigma_{zz}\partial \sigma_{xx}} = \frac{3}{2\sqrt{3J_2}}\left[\frac{\partial^2 J_2}{\partial \sigma_{zz}\partial \sigma_{xx}} - \frac{3}{2}\left(\frac{\partial J_2}{\partial \sigma_{zz}}\frac{\partial J_2}{\partial \sigma_{xx}}\right)\frac{1}{3J_2}\right]$$

$$\frac{\partial^2 f}{\partial \sigma_{zz}\partial \sigma_{yy}} = \frac{3}{2\sqrt{3J_2}}\left[\frac{\partial^2 J_2}{\partial \sigma_{zz}\partial \sigma_{yy}} - \frac{3}{2}\left(\frac{\partial J_2}{\partial \sigma_{zz}}\frac{\partial J_2}{\partial \sigma_{zz}}\right)\frac{1}{3J_2}\right]$$

$$\frac{\partial^2 f}{\partial \sigma_{zz}^2} = \frac{3}{2\sqrt{3J_2}}\left[\frac{\partial^2 J_2}{\partial \sigma_{zz}^2} - \frac{3}{2}\left(\frac{\partial J_2}{\partial \sigma_{zz}}\right)^2 \frac{1}{3J_2}\right]$$

$$\frac{\partial^2 f}{\partial \sigma_{zz}\partial \sigma_{xy}} = \frac{3}{2\sqrt{3J_2}}\left[\frac{\partial^2 J_2}{\partial \sigma_{zz}\partial \sigma_{xy}} - \frac{3}{2}\left(\frac{\partial J_2}{\partial \sigma_{zz}}\frac{\partial J_2}{\partial \sigma_{xy}}\right)\frac{1}{3J_2}\right]$$

$$\frac{\partial^2 f}{\partial \sigma_{zz}\partial \sigma_{yz}} = \frac{3}{2\sqrt{3J_2}}\left[\frac{\partial^2 J_2}{\partial \sigma_{zz}\partial \sigma_{yz}} - \frac{3}{2}\left(\frac{\partial J_2}{\partial \sigma_{zz}}\frac{\partial J_2}{\partial \sigma_{yz}}\right)\frac{1}{3J_2}\right]$$

$$\frac{\partial^2 f}{\partial \sigma_{zz}\partial \sigma_{xz}} = \frac{3}{2\sqrt{3J_2}}\left[\frac{\partial^2 J_2}{\partial \sigma_{zz}\partial \sigma_{xz}} - \frac{3}{2}\left(\frac{\partial J_2}{\partial \sigma_{zz}}\frac{\partial J_2}{\partial \sigma_{xz}}\right)\frac{1}{3J_2}\right]$$

$$\frac{\partial^2 f}{\partial \sigma_{xy}\partial \sigma_{xx}} = \frac{3}{2\sqrt{3J_2}}\left[\frac{\partial^2 J_2}{\partial \sigma_{xy}\partial \sigma_{11}} - \frac{3}{2}\left(\frac{\partial J_2}{\partial \sigma_{xy}}\frac{\partial J_2}{\partial \sigma_{xx}}\right)\frac{1}{3J_2}\right]$$

$$\frac{\partial^2 f}{\partial \sigma_{xy}\partial \sigma_{yy}} = \frac{3}{2\sqrt{3J_2}}\left[\frac{\partial^2 J_2}{\partial \sigma_{xy}\partial \sigma_{yy}} - \frac{3}{2}\left(\frac{\partial J_2}{\partial \sigma_{xy}}\frac{\partial J_2}{\partial \sigma_{yy}}\right)\frac{1}{3J_2}\right]$$

$$\frac{\partial^2 f}{\partial \sigma_{xy}\partial \sigma_{yy}} = \frac{3}{2\sqrt{3J_2}}\left[\frac{\partial^2 J_2}{\partial \sigma_{xy}\partial \sigma_{yy}} - \frac{3}{2}\left(\frac{\partial J_2}{\partial \sigma_{xy}}\frac{\partial J_2}{\partial \sigma_{yy}}\right)\frac{1}{3J_2}\right]$$

$$\frac{\partial^2 f}{\partial \sigma_{xy}^2} = \frac{3}{2\sqrt{3J_2}}\left[\frac{\partial^2 J_2}{\partial \sigma_{xy}^2} - \frac{3}{2}\left(\frac{\partial J_2}{\partial \sigma_{xy}}\right)^2\frac{1}{3J_2}\right]$$

$$\frac{\partial^2 f}{\partial \sigma_{xy}\partial \sigma_{xz}} = \frac{3}{2\sqrt{3J_2}}\left[\frac{\partial^2 J_2}{\partial \sigma_{xy}\partial \sigma_{yz}} - \frac{3}{2}\left(\frac{\partial J_2}{\partial \sigma_{xy}}\frac{\partial J_2}{\partial \sigma_{yz}}\right)\frac{1}{3J_2}\right]$$

$$\frac{\partial^2 f}{\partial \sigma_{xy}\partial \sigma_{xz}} = \frac{3}{2\sqrt{3J_2}}\left[\frac{\partial^2 J_2}{\partial \sigma_{xy}\partial \sigma_{xz}} - \frac{3}{2}\left(\frac{\partial J_2}{\partial \sigma_{xy}}\frac{\partial J_2}{\partial \sigma_{xz}}\right)\frac{1}{3J_2}\right]$$

$$\frac{\partial^2 f}{\partial \sigma_{yz}\partial \sigma_{xx}} = \frac{3}{2\sqrt{3J_2}}\left[\frac{\partial^2 J_2}{\partial \sigma_{yz}\partial \sigma_{xx}} - \frac{3}{2}\left(\frac{\partial J_2}{\partial \sigma_{yz}}\frac{\partial J_2}{\partial \sigma_{xx}}\right)\frac{1}{3J_2}\right]$$

$$\frac{\partial^2 f}{\partial \sigma_{yz}\partial \sigma_{yy}} = \frac{3}{2\sqrt{3J_2}}\left[\frac{\partial^2 J_2}{\partial \sigma_{yz}\partial \sigma_{yy}} - \frac{3}{2}\left(\frac{\partial J_2}{\partial \sigma_{yz}}\frac{\partial J_2}{\partial \sigma_{yy}}\right)\frac{1}{3J_2}\right]$$

$$\frac{\partial^2 f}{\partial \sigma_{yz}\partial \sigma_{zz}} = \frac{3}{2\sqrt{3J_2}}\left[\frac{\partial^2 J_2}{\partial \sigma_{yz}\partial \sigma_{zz}} - \frac{3}{2}\left(\frac{\partial J_2}{\partial \sigma_{yz}}\frac{\partial J_2}{\partial \sigma_{zz}}\right)\frac{1}{3J_2}\right]$$

$$\frac{\partial^2 f}{\partial \sigma_{yz}\partial \sigma_{xy}} = \frac{3}{2\sqrt{3J_2}}\left[\frac{\partial^2 J_2}{\partial \sigma_{yz}\partial \sigma_{xy}} - \frac{3}{2}\left(\frac{\partial J_2}{\partial \sigma_{yz}}\frac{\partial J_2}{\partial \sigma_{xy}}\right)\frac{1}{3J_2}\right]$$

$$\frac{\partial^2 f}{\partial \sigma_{yz}^2} = \frac{3}{2\sqrt{3J_2}}\left[\frac{\partial^2 J_2}{\partial \sigma_{yz}^2} - \frac{3}{2}\left(\frac{\partial J_2}{\partial \sigma_{yz}}\right)^2\frac{1}{3J_2}\right]$$

$$\frac{\partial^2 f}{\partial \sigma_{yz}\partial \sigma_{xz}} = \frac{3}{2\sqrt{3J_2}}\left[\frac{\partial^2 J_2}{\partial \sigma_{yz}\partial \sigma_{xz}} - \frac{3}{2}\left(\frac{\partial J_2}{\partial \sigma_{yz}}\frac{\partial J_2}{\partial \sigma_{xz}}\right)\frac{1}{3J_2}\right]$$

$$\frac{\partial^2 f}{\partial \sigma_{xz}\partial \sigma_{xx}} = \frac{3}{2\sqrt{3J_2}}\left[\frac{\partial^2 J_2}{\partial \sigma_{xz}\partial \sigma_{xx}} - \frac{3}{2}\left(\frac{\partial J_2}{\partial \sigma_{xz}}\frac{\partial J_2}{\partial \sigma_{xx}}\right)\frac{1}{3J_2}\right]$$

$$\frac{\partial^2 f}{\partial \sigma_{xz}\partial \sigma_{yy}} = \frac{3}{2\sqrt{3J_2}}\left[\frac{\partial^2 J_2}{\partial \sigma_{xz}\partial \sigma_{yy}} - \frac{3}{2}\left(\frac{\partial J_2}{\partial \sigma_{xz}}\frac{\partial J_2}{\partial \sigma_{yy}}\right)\frac{1}{3J_2}\right]$$

$$\frac{\partial^2 f}{\partial \sigma_{xz}\partial \sigma_{zz}} = \frac{3}{2\sqrt{3J_2}}\left[\frac{\partial^2 J_2}{\partial \sigma_{xz}\partial \sigma_{zz}} - \frac{3}{2}\left(\frac{\partial J_2}{\partial \sigma_{xz}}\frac{\partial J_2}{\partial \sigma_{zz}}\right)\frac{1}{3J_2}\right]$$

$$\frac{\partial^2 f}{\partial \sigma_{xz}\partial \sigma_{xy}} = \frac{3}{2\sqrt{3J_2}}\left[\frac{\partial^2 J_2}{\partial \sigma_{xz}\partial \sigma_{xy}} - \frac{3}{2}\left(\frac{\partial J_2}{\partial \sigma_{xz}}\frac{\partial J_2}{\partial \sigma_{xy}}\right)\frac{1}{3J_2}\right]$$

$$\frac{\partial^2 f}{\partial \sigma_{xz}\partial \sigma_{yz}} = \frac{3}{2\sqrt{3J_2}}\left[\frac{\partial^2 J_2}{\partial \sigma_{xz}\partial \sigma_{yz}} - \frac{3}{2}\left(\frac{\partial J_2}{\partial \sigma_{xz}}\frac{\partial J_2}{\partial \sigma_{yz}}\right)\frac{1}{3J_2}\right]$$

$$\frac{\partial^2 f}{\partial \sigma_{xz}^2} = \frac{3}{2\sqrt{3J_2}}\left[\frac{\partial^2 J_2}{\partial \sigma_{xz}^2} - \frac{3}{2}\left(\frac{\partial J_2}{\partial \sigma_{xz}}\right)^2\frac{1}{3J_2}\right]$$

The first order complementary derivatives are expressed as

$$\frac{\partial J_2}{\partial \sigma_{xx}} = \frac{1}{3}\left[2\sigma_{xx} - (\sigma_{yy} + \sigma_{zz})\right] = S_{xx}$$
$$\frac{\partial J_2}{\partial \sigma_{yy}} = \frac{1}{3}\left[2\sigma_{yy} - (\sigma_{xx} + \sigma_{zz})\right] = S_{yy}$$
$$\frac{\partial J_2}{\partial \sigma_{zz}} = \frac{1}{3}\left[2\sigma_{zz} - (\sigma_{yy} + \sigma_{xx})\right] = S_{zz}$$
$$\frac{\partial J_2}{\partial \sigma_{xy}} = 2\sigma_{xy} = S_{xy}$$
$$\frac{\partial J_2}{\partial \sigma_{yz}} = 2\sigma_{yz} = S_{yz}$$
$$\frac{\partial J_2}{\partial \sigma_{xz}} = 2\sigma_{xz} = S_{xz}$$

The second order complementary derivatives are presented as follows

$$\frac{\partial^2 J_2}{\partial \sigma_{xx}^2} = \frac{2}{3}$$
$$\frac{\partial^2 J_2}{\partial \sigma_{yy}^2} = \frac{2}{3}$$
$$\frac{\partial^2 J_2}{\partial \sigma_{zz}^2} = \frac{2}{3}$$
$$\frac{\partial^2 J_2}{\partial \sigma_{xy}^2} = 2$$
$$\frac{\partial^2 J_2}{\partial \sigma_{yz}^2} = 2$$
$$\frac{\partial^2 J_2}{\partial \sigma_{xz}^2} = 2$$
$$\frac{\partial^2 J_2}{\partial \sigma_{xx} \partial \sigma_{yy}} = -\frac{1}{3}$$
$$\frac{\partial^2 J_2}{\partial \sigma_{xx} \partial \sigma_{zz}} = -\frac{1}{3}$$
$$\frac{\partial^2 J_2}{\partial \sigma_{xx} \partial \sigma_{yy}} = -\frac{1}{3}$$
$$\frac{\partial^2 J_2}{\partial \sigma_{xx} \partial \sigma_{xy}} = 0$$
$$\frac{\partial^2 J_2}{\partial \sigma_{xx} \partial \sigma_{yz}} = 0$$
$$\frac{\partial^2 J_2}{\partial \sigma_{xx} \partial \sigma_{xz}} = 0$$
$$\frac{\partial^2 J_2}{\partial \sigma_{yy} \partial \sigma_{xx}} = -\frac{1}{3}$$
$$\frac{\partial^2 J_2}{\partial \sigma_{yy} \partial \sigma_{zz}} = -\frac{1}{3}$$
$$\frac{\partial^2 J_2}{\partial \sigma_{yy} \partial \sigma_{xy}} = 0$$
$$\frac{\partial^2 J_2}{\partial \sigma_{yy} \partial \sigma_{yz}} = 0$$
$$\frac{\partial^2 J_2}{\partial \sigma_{yy} \partial \sigma_{xz}} = 0$$
$$\frac{\partial^2 J_2}{\partial \sigma_{zz} \partial \sigma_{xx}} = -\frac{1}{3}$$
$$\frac{\partial^2 J_2}{\partial \sigma_{zz} \partial \sigma_{yy}} = -\frac{1}{3}$$

$$\frac{\partial^2 J_2}{\partial \sigma_{zz} \partial \sigma_{xy}} = 0$$
$$\frac{\partial^2 J_2}{\partial \sigma_{zz} \partial \sigma_{yz}} = 0$$
$$\frac{\partial^2 J_2}{\partial \sigma_{zz} \partial \sigma_{xz}} = 0$$
$$\frac{\partial^2 J_2}{\partial \sigma_{xy} \partial \sigma_{xx}} = 0$$
$$\frac{\partial^2 J_2}{\partial \sigma_{xy} \partial \sigma_{yy}} = 0$$
$$\frac{\partial^2 J_2}{\partial \sigma_{xy} \partial \sigma_{zz}} = 0$$
$$\frac{\partial^2 J_2}{\partial \sigma_{xy} \partial \sigma_{yz}} = 0$$
$$\frac{\partial^2 J_2}{\partial \sigma_{xy} \partial \sigma_{xz}} = 0$$
$$\frac{\partial^2 J_2}{\partial \sigma_{yz} \partial \sigma_{xx}} = 0$$
$$\frac{\partial^2 J_2}{\partial \sigma_{yz} \partial \sigma_{yy}} = 0$$
$$\frac{\partial^2 J_2}{\partial \sigma_{yz} \partial \sigma_{zz}} = 0$$
$$\frac{\partial^2 J_2}{\partial \sigma_{yz} \partial \sigma_{yz}} = 0$$
$$\frac{\partial^2 J_2}{\partial \sigma_{yz} \partial \sigma_{xz}} = 0$$
$$\frac{\partial^2 J_2}{\partial \sigma_{xz} \partial \sigma_{xx}} = 0$$
$$\frac{\partial^2 J_2}{\partial \sigma_{xz} \partial \sigma_{yy}} = 0$$
$$\frac{\partial^2 J_2}{\partial \sigma_{xz} \partial \sigma_{zz}} = 0$$
$$\frac{\partial^2 J_2}{\partial \sigma_{xz} \partial \sigma_{xy}} = 0$$
$$\frac{\partial^2 J_2}{\partial \sigma_{xz} \partial \sigma_{yz}} = 0$$

It is important to point out that the derivatives can be permuted due to the isotropic properties of the material.

B.3 Viscoplasticity

The Perzyna model used in Subsection 5.2.3 is presented here in more details. In this scenario, the viscoplastic deformation is defined as

$$\Delta\varepsilon_{ij}^{i} = \frac{\Delta t}{\mu_{\varepsilon}}\left[\left(\frac{\sqrt{3J_2}}{\sigma_y}\right)^{N_{\varepsilon}} - 1\right]\frac{\partial f}{\partial \sigma_{ij}} = \Delta\bar{\varepsilon}\frac{\partial f}{\partial \sigma_{ij}} \tag{B.34}$$

And the internal variable increment $\Delta\bar{\varepsilon}$ is explicitly written as follows

$$\Delta\bar{\varepsilon} = \begin{cases} \dfrac{\Delta t}{\mu}\left[\left(\frac{\sqrt{3J_2}}{\sigma_y}\right)^{N_{\varepsilon}} - 1\right], & f \geq 0 \\ 0, & f < 0 \end{cases} \tag{B.35}$$

In case of inelastic load, the material yields and elastic-plastic surface function is expressed by

$$\Delta\bar{\varepsilon} - \frac{\Delta t}{\mu_{\varepsilon}}\left[\left(\frac{\sqrt{3J_2}}{\sigma_y}\right)^{N_{\varepsilon}} - 1\right] = 0 \tag{B.36}$$

which can be rearranged as

$$f = \sqrt{3J_3} - \sigma_y\left(\frac{\mu_{\varepsilon}\Delta\bar{\varepsilon}}{\Delta t} + 1\right)^{N_{\varepsilon}}. \tag{B.37}$$